UNIVERSIDADE D
COIMBRA

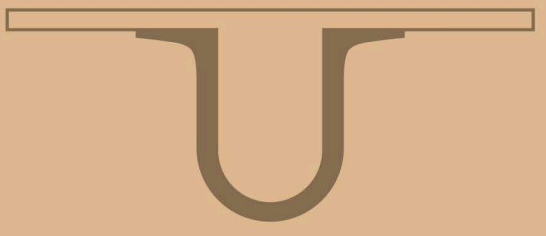

Miguel Alexandre Gonçalves Santos

DEVELOPMENT OF A DUAL-POLARITY ION DRIFT CHAMBER & STUDY OF ION TRANSPORT PROPERTIES IN GASEOUS MIXTURES OF INTEREST

Dissertation presented to obtain the Integrated Master's degree in Engineering Physics, branch of Instrumentation, supervised by Prof. Dr. Filipa Melo Borges Belo Soares (FCTUC) and by André Filipe Ventura Cortez (LIP) and submitted to the Faculty of Sciences and Technology of the University of Coimbra.

September 2018

Miguel Alexandre Gonçalves Santos

Development of a Dual-Polarity Ion Drift Chamber & Study of ion transport properties in gaseous mixtures of interest

Dissertation presented to the University of Coimbra
in order to complete the necessary requirements to
obtain the Master's degree in Engineering Physics.

LABORATÓRIO DE INSTRUMENTAÇÃO
E FÍSICA EXPERIMENTAL DE PARTÍCULAS
partículas e tecnologia

Supervisor:

Prof. Dr. Filipa Melo Borges Belo Soares (FCTUC)

Co-supervisor:

MSc. André Filipe Ventura Cortez (LIP)

Coimbra, September 2018

To my family...

Acknowledgments

To Prof. Dr. Filipa Borges and André Cortez, who supervised this thesis, for their patient guidance and help, enthusiastic encouragement and useful critiques in this work, as well as for accepting and trusting me with this project.

To the researchers at LIP: Prof. Filomena Santos, Alexandre Trindade, Dr. José Escada, Miguel Moita and Dr. Carlos Conde for their availability and help, sharing their expertises and knowledge without any constraints. Thank you as well for the delightful conversations which made me feel like I was a part of the group.

To the team of the LIP workshop and lab facilities: Eng. Rui Alves, Nuno Dias, Douglas Dias, Américo Cunha, Luís Lopes, Nuno Carolino and Carlos Silva, for your precious suggestions and help in the design and construction of the necessary components for the DP-IDC.

To the GIAN group for supplying me with Kapton foils and helping me with the CsI deposition, in particular to Dr. Fernando Amaro and Pedro Silva.

Institutionally, to the Laboratory of Instrumentation and Experimental Particle Physics (LIP-Coimbra) and to the Physics Department of the University of Coimbra for providing me with the necessary tools and infrastructure with which I developed this work.

To all my friends and colleagues for being present in the good and bad times, especially to Rafael Ferreira, Carolina Sousa and Marco Alberto. Thank you for all the help, companionship, emotional support and enlightening discussions, not only during this work but across these last 6 years.

Last but not least, to Inês Costa* and to my family, in particular to my parents Paula Gonçalves and José Santos, for all the love, kindness, patience and unconditional support.

To all of you, my deepest gratitude.

Resumo

O estudo das propriedades de transporte de iões em gases e misturas gasosas é de grande relevância em várias áreas desde a química à física, especialmente para o desenvolvimento de detetores de radiação de grande volume, como ”Time Projection Chambers” (TPCs), onde a deriva dos iões representa um papel importante na formação de sinal.

Por exemplo, no futuro Linear Collider TPC (LCTPC), que será o detetor central da experiência ”Internatinal Linear Collider” (ILC), a deriva dos iões positivos poderá ter efeitos nocivos no desempenho do detetor. De modo a perceber a sua influência na formação sinal e a desenvolver sistemas para a mitigar, vários estudos sobre a mobilidade de iões em gases e misturas gasosas de interesse serão apresentados nesta dissertação. Nomeadamente, em isobutano puro (iso-C_4H_{10}), em misturas binárias de árgon (Ar) com tetrafluorometano (CF_4) e isobutano, e em misturas binárias de tetrafluorometano com metano (CH_4), etano (C_2H_6) e isobutano. Finalmente, foram feitas medidas em misturas ternárias de Ar–CF_4–CH_4 (92-3-5), Ar–CF_4–C_2H_6 (94-3-3) e Ar–CF_4–iso-C_4H_{10} (95-3-2). Além disso, será apresentada uma interpretação dos resultados obtidos em misturas de árgon com azoto (N_2), utilizando resultados obtidos anteriormente. Os resultados são apresentados para pressões totais entre 6 e 10 Torr, para campos elétricos reduzidos (E/N) entre 15 e 20 Td na maioria dos casos, tendo sido alargada a gama de E/N (10-45 Td) para o estudo em isobutano puro, à temperatura ambiente (293K).

Por outro lado, recentemente tem surgido o interesse no desenvolvimento de ”Negative Ion TPCs” (NITPCs) para física de eventos raros, como a procura de matéria escura e de decaimentos beta sem emissão de neutrinos, e também para astrofísica, pelo seu potencial em experiências de polarimetria de raio-X.

Neste sentido, e em paralelo com os trabalhos de medição da mobilidade de iões positivos, uma nova câmara de deriva de iões, apelidada ”Dual-Polarity Ion Drift Chamber” (DP-IDC), foi desenvolvida no âmbito deste trabalho. Esta nova câmara, para além do estudo da mobilidade de iões positivos, permitirá realizar estudos de mobilidade de iões negativos com interesse para o desenvolvimento de NITPCs, bem como variar a distância de deriva, funcionalidade que possibilitará retirar diferentes conclusões sobre a deriva de iões com especial interesse para o desenvolvimento de detetores de alta pressão.

No âmbito deste trabalho, este novo sistema experimental foi projetado, construído, montado e testado. Os resultados dos primeiros testes com este protótipo serão apresentados, bem como uma discussão sobre as suas limitações atuais e formas de as resolver.

Palavras-chave: Transporte de cargas e multiplicação em gases; Fontes de iões (iões positivos, iões negativos, electron cyclotron resonance (ECR), electron beam (EBIS)); Detetores gasosos; Processos de ionização e excitacão; Mobilidade de ioes.

Abstract

The study of ion transport properties in gases and gas mixtures is highly relevant in several areas ranging from chemistry to physics, especially in the development of large volume radiation detectors, such as Time Projection Chambers (TPCs), where the drift of ions plays an important role in the pulse shape.

For example, in the upcoming Linear Collider TPC (LCTPC), which will be the central detector of the International Linear Collider (ILC) experiment, the drift of the positive ions may have undesirable effects on the detector performance. In order to both understand their influence on signal formation and to develop systems to reduce it, several studies on the mobility of positive ions in gases and gaseous mixtures of interest will be presented in this dissertation, namely, for pure isobutane (iso-C_4H_{10}), for binary mixtures of argon (Ar) with carbon-tetrafluoride (CF_4) and isobutane, for binary mixtures of carbon-tetrafluoride with methane (CH_4), ethane (C_2H_6) and isobutane. Finally, for ternary mixtures of Ar–CF_4–CH_4 (92-3-5), Ar–CF_4–C_2H_6 (94-3-3) and Ar–CF_4–iso-C_4H_{10} (95-3-2). Also, an interpretation of the results previously obtained in mixtures of argon with nitrogen (N_2) is presented. These results are presented for total pressures ranging from 6 to 10 Torr, for reduced electric fields (E/N) of 15 and 20 Td for most of the cases, with a larger range (10-45 Td) studied in the pure isobutane case, at room temperature (293K).

On the other hand, interest has recently appeared in the development of Negative Ion TPCs (NITPCs) for rare event physics, such as dark matter and neutrinoless beta decay searches, and for astrophysics, because of their potential application in X-ray polarimetry.

With this in mind, and in parallel with the positive ion mobility measurement work, a new ion drift chamber, named Dual-Polarity Ion Drift Chamber (DP-IDC), was developed within the scope of this work. This new chamber will not only allow the study of the mobility of positive ions, but will also enable us to perform studies on the mobility of negative ions with interest for the development of NITPCs, as well as allow the variation of the drift distance which will enable us to draw different conclusions about the ions drifting in the gases with special interest for the development of high pressure detectors.

In the scope of this work, this new experimental system was designed, constructed, assembled and tested. The results of the first tests with this prototype will be presented here, as well as a discussion of its current limitations, and suggestions of improvements on its performance.

Keywords: Charge transport and multiplication in gases; Ion sources (positive ions, negative ions, electron cyclotron resonance (ECR), electron beam (EBIS)); Gaseous detectors; Ionization and excitation processes; Ion mobility.

Publications

Scientific publications:

1. A.F.V. Cortez, M.A.G. Santos *et al.*, *"Experimental ion mobility measurements in Xe-CO_2"*. Journal of Instrumentation, 12(06):P06012, 2017.

2. M.A.G. Santos *et al.*, *"Experimental ion mobility measurements for the LCTPC Collaboration - Ar-CF_4 mixtures"*. Journal of Instrumentation, 13(04):P04012, 2018

3. A.F.V. Cortez, M.A. Kaja, J. Escada, M.A.G. Santos *et al.*, *"Experimental ion mobility measurements in Xe-CF_4 mixtures"*. Journal of Instrumentation, 13(04):P04006, 2018

4. A.F.V. Cortez, M.A.G. Santos *et al.*, *"Experimental ion mobility measurements for the LCTPC Collaboration"*. Conference paper. 14th Pisa Meeting on Advanced Detectors: Frontier Detectors for Frontier Physics, La Biodola-Isola d'Elba, Livorno, Italy, May 2018. Submitted.

5. M.A.G. Santos *et al.*, *"Experimental ion mobility measurements in Ar-N_2"*. Journal of Instrumentation, 2018. Accepted.

Oral communications:

6. A.F.V. Cortez, M.A.G. Santos *et al.*, *"Ion Mobility in Ar-CF_4"*. LCTPC Collaboration Meeting @DESY (Germany), November 2017.

7. M.A.G. Santos *et al.*, *"Ion mobility studies for the ILC experiment"*. RD51 Collaboration Mini-week @CERN (Switzerland), December 2017.

8. M.A.G. Santos *et al.*, *"Alternative gas mixtures for LCTPC: Ar-CF_4-C_2H_6"*. RD51 Collaboration Mini-week @CERN (Switzerland), February 2018.

9. M.A.G. Santos *et al.*, *"Ion Mobility studies in Ar-CF_4-iC_4H_{10} mixtures for the LCTPC Collaboration"*. RD51 Collaboration Meeting @TUM (Munich), June 2018.

Poster communications:

10. A.F.V. Cortez, M.A.G. Santos *et al.*, *"Experimental ion mobility measurements for the LCTPC Collaboration"*. 14th Pisa Meeting on Advanced Detectors: Frontier Detectors for Frontier Physics, La Biodola-Isola d'Elba, Livorno, Italy, May 2018.

11. M.A.G. Santos *et al.*, *"Ion mobility in gas mixtures for large volume detectors"*. @UBI (Portugal), FISICA 2018, August/September 2018.

12. M.A.G. Santos *et al.*, *"Experimental ion mobility studies of alternative gas mixtures for the LCTPC"*. Sydney, Australia, IEEE Nuclear Science Symposium and Medical Imaging Conference, November 2018. Accepted.

Contents

List of Tables

List of Figures

Nomenclature

CsI Caesium Iodide

DC Direct Current

DP-IDC Dual-Polarity Ion Drif Chamber

E/N Reduced electric field expressed in Td

GEM Gas Electron Multiplier

HV High Voltage

ILC International Linear Collider

LCTPC Linear Collider Time Projection Chamber

Micromegas MICRO-MEsh GASeous structures

MWPC Multi-Wire Proportional Chamber

MPGD Micro-Pattern Gaseous Detectors

NITPC Negative Ion Time Projection Chamber

TPC Time Projection Chamber

$\boldsymbol{V}_{GEM}$ Voltage across the GEM electrodes expressed in V

VUV Vacuum Ultraviolet

Chapter 1

Introduction and Motivation

The knowledge of ion mobility is of considerable importance in various fields ranging from physics to chemistry, within the areas of radiation physics, astrophysics and chemical analyses of compounds. For example, Ion Mobility Spectroscopy (IMS) is a technique that aims to identify substances based on the drift of the ions of a volatile or semi-volatile organic compound under the influence of an electric field [1]. Applications of this technique can be found in many fields ranging from military, security, pharmaceutical, clinical, environmental and food analysis, process monitoring and space exploration [2]. Examples of its application are the detection of explosives, due to the presence of electronegative nitrated derivatives, and drug detection, due to their amido groups composition, that exhibit high affinity to form positive ions.

However the main concern of the present work is to understand ion transport properties in gaseous mixtures of interest in gaseous radiation detectors with spacial resolutions, specifically in Time Projection Chambers (TPCs), where ions have various roles depending on the type, configuration and properties of the detector.

Positive ions' drift may have an important role on the signal pulse shape obtained, since clouds of positive ions can produce changes on the electric field present and induce a signal on the anode while drifting to the cathode. On the other hand, in most gaseous radiation detectors, negative ions are usually a hindrance since they reduce the signal by capturing the electrons responsible for it, so their presence must be minimized. However, in the Negative Ion Time Projection Chamber (NITPC), their transport properties are of great importance to use Time-Of-Flight (TOF) methods for spatial projection of ionization tracks.

The first part of this work focuses on measurements of positive ion mobility for mixtures of interest for the Linear Collider Time Projection Chamber (LCTPC) project, with the main objective of understanding the influence of gases with carbon content as additives to the main argon (Ar) gas on the mobility of the ions.

The second part of this work, will focus on topics of the development of the first prototype of a Dual-Polarity Ion Drift Chamber (DP-IDC) which will allow to perform experimental measurements of ion mobility, and eventually diffusion, for both negative and positive ions, in mixtures of interest for NITPCs.

1.1 Time Projection Chamber

Time Projection Chambers (TPCs) were invented in 1976 by D. Nygren [3] for the electron-positron (PEP4) collider experiment at SLAC, which started taking data in 1983 [4]. Thenceforth, TPC use increased massively, as their dimensions and number of read-out channels grew significantly. Today, they are a very important tool in the fields of experimental high energy, nuclear and astroparticle physics as in the TOPAZ TPC, ALEPH TPC, DELPHI TPC, STAR, NA49, Ceres and in the LHC at CERN in the ALICE TPC experiment because of their powerful tracking capabilities allied with efficient particle identification over a wide range of momentum from a multiplicity of specific energy loss (dE/dx) measurements [4].

In their most conventional geometry (original design) they consist of a sensitive, gas filled, volume, usually cylindrical, with an high voltage applied between the two ends, the anode at a positive high voltage, coupled at a readout system, and the cathode at negative voltage or grounded, as can be seen in Figure 1.1.

When a charged particle transverses their gaseous volume, it will ionize the gas along its trajectory originating electrons and positive ions that drift in opposite directions. When under an uniform electric field, the free electrons will drift towards the anode, where the signal will be induced and the radial and azimuthal trajectories can be reconstructed. As the electrons drift under a uniform electric field and reach a velocity that can be considered constant, the knowledge of their mobility and their drift time, allows to obtain the longitudinal position of the interaction.

In most high energy physics application, TPCs work very well because of the very high drift speeds of the electrons, which can be improved by the gaseous mixture chosen.

Due to the electric field applied, the longitudinal diffusion of electrons along E is different from its transverse diffusion. As the detector size increases, the effects of transverse and longitudinal diffusion of the electrons can limit the maximum spatial resolution obtained, since they tend increase the signal width. In order to suppress this effect a magnetic field can be applied, parallel to the drift field, to minimize transverse electron diffusion and/or a gas mixture with smaller electron diffusion coefficients can be chosen [4].

The inherent three-dimensional track reconstruction can provide us valuable information on the stopping power measurements and in the identification of the particles involved. Also, the versatility of the gaseous mixture choice helps to optimize the most important properties of the detector such as electron and ion drift velocity, stopping power in terms of the type of ionizing radiation (by choosing gas mixtures with the appropriate Z number), electron diffusion, signal amplification, cost, *etc*.

The TPCs concept is still evolving: new position-sensitive electron amplification systems are being studied as parallel plate chambers and Micro-Pattern Gaseous Detectors (MPGDs) as Gaseous Electron Multipliers (GEMs) and MICRO-MEsh GASeous structures (Micromegas) and with the use of new geometries, cylinder but with radial electric field or even flat geometries.

Ions, due to their higher mass, rapidly lose their energy in the collisions with the gas molecules, therefore their kinetic energy stays close to thermal. So their diffusion is much smaller and isotropic than that of the electrons, their mobility stays fairly constant with the fields. With the purpose of making use

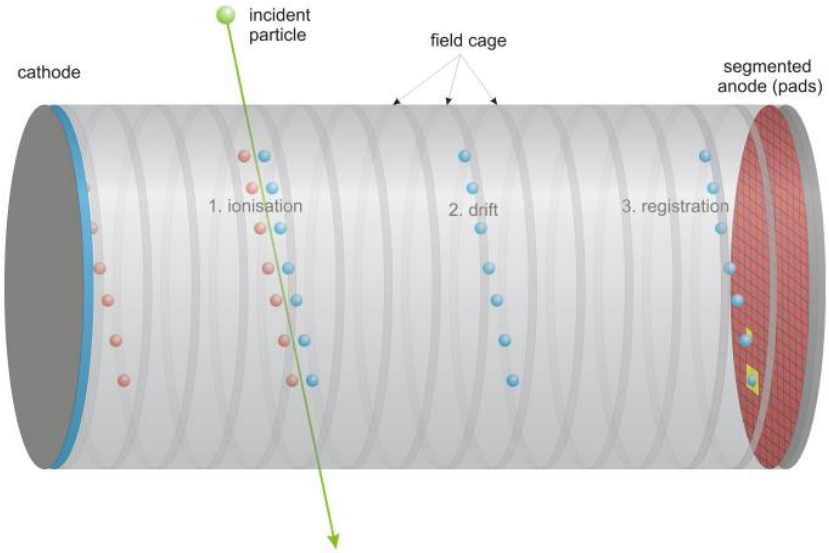

Figure 1.1: Schematics of a conventional TPC (extracted from [6]). An incident particle ionizes molecules of the filling gas, creating ion-electron pairs. The positive ions (in red) and electrons/negative ion (in blue) drift towards the cathode and anode, respectively, guided by an uniform electric field created by the HV rings of the field cage.

of these advantageous properties of ions in the TPCs for low rate signal applications, new techniques using negative ions instead of electrons as the information carriers have been developed, the Negative Ion Time Projection Chambers (NITPCs), which will be addressed in a later section. Also, the theoretical possibility of using positive ion detection as a way to suppress the negative effects of the diffusion of electrons is being addressed [5] .

1.2 Space charge effects and ion backflow

In Multi-Wire Proportional Chambers (MWPCs) the output signal is produced by induction of moving charges such as electrons and positive ions. As electrons pass through the drift portion of the volume and enter the amplification stage, they start avalanches that produce a great quantity of ion-electron pairs, which induces electrical signals on the wires. While electrons drift quickly away from the wires, ions move slowly producing long tailed signals thus representing up to 80% of the induced signal, even for lower shaping times around where only 30% of the charge is collected [4]. Because of this phenomenon, the shaping times are usually lower than that of the full collection times and the signals are required to be shaped electronically to avoid pulse pile-up effects.

These ions produced during the avalanche build space charge effects in both the amplification and the drift stages of the detector.

In the multiplication stage, the massive quantity of ions produced drift very slowly away from the multiplication area distorting the electric field, usually by reducing it, thus reducing the amplification gain and the output signal amplitude below the expected value. Thus, these variations tend to reduce the energy resolution of the detector.

These space charge effects can be categorized as self-induced or cumulative [7]. Depending on the multiplication gain of the filling gas, ions formed during one avalanche can affect the output of the following avalanches, producing self-induced space charge effects that do not depend on the pulse rate. On the other hand, depending on the pulse rate, cumulative space charge effects can take place, especially at higher pulse rates where positive ions formed due to a set of avalanches from a given event affect the output of subsequent events. Both of these effects can be minimized by choosing an gas mixture with high ion mobility in order to quickly remove them from the multiplication zone.

In a drift chamber, ions producing space charge effects can be due to the gas ionization, which is an intrinsic process and has a low impact on the detector performance, or from the multiplication stage, since ions drift back to the drift volume. In this case, their effect is several orders of magnitude larger and can lead to significant distortions in the electric field [8].

In the near future, MPGD structures, such as GEMs, are expected to substitute the previous MWPC readout systems. GEMs intrinsically suppress the ion backflow by trapping the ions at their electrodes when lower electric fields in the drift region are applied. However, even multi-GEM structures have leakages higher than the ones that it is possible to achieve with the use of closed gating grids [8]. Still, this is not enough when the goal is to have leakages lower than 10^{-4} for not to increase the charge density above the one due to the primary ionization. In fact, for example in ALICE TPC [9], studies with triple GEM structure found that the ion backflows exceed the maximum tolerable drift field distortion specifications [10].

For diminishing these effects, gating grids need to be added, even since the PEP4 experiment, because of the high rate of events. The most simple way is to do it using a static mode gating grid blocking all ions and letting a great fraction of the electrons pass but which still represents a significant signal loss of about 25$\%$. This number was acceptable for the DELPHI experiment. But most of the TPCs use a mode in which the gate opens on a trigger for the full drift time of the event, closing after that it [4].

1.3 LCTPC and our objective

The main goal of the International Linear Colider (ILC) is to enrich our understanding of the Higgs boson through electron-positron collisions, instead of through ion collision as in the ALICE experiment. However, in order to achieve this objective, a new LCTPC is under research and development with the purpose of improving the energy and spacial resolutions to near intrinsic levels, over the capabilities of the ALICE TPC.

Since the density of ionization in the chamber depends on the momentum and type of particle [11], measurements of the positions and specific energy loss are required as means to accurately and efficiently reconstruct their tracks and identify the particles transversing the volume.

One of the ways they intend to improve over the ALICE TPC is by substituting the gas amplification systems from multi-wires multiplication to MPGDs such as Micromegas and GEMs which are more robust, easily supportable, do not suffer from $\mathbf{E} \times \mathbf{B}$ effects, and also, reduce the influence of the space

charge effects [11].

As the operation conditions of the TPC are of high rate of interactions, effects from the ion backdrift to the main chamber are expected to have an impact on the sensitive volume. In order to suppress this ion backdrift into the volume, a gating plane will be designed that will open and close between trains in order to guarantee robust and stable operations, as well as to remove the need for corrections due to space charges effects.

The development of this gating device is one of the biggest and urgent challenges on the R&D for the LCTPC and in this document, results on experimental ion mobility in several alternative mixtures for the LCTPC are presented that will help the positioning of the gates [11, 12].

1.4 Gas choice for the LCTPC

Gaseous radiation detectors based on charge multiplication, such as MWPCs and TPCs, are usually filled with a mixture of gases: a noble gas with one or more molecular additives for quenching (minimizing the possibility of multiple pulsing detection), and other stability of operation reasons.

Avalanche multiplication occurs in atomic gases at lower electric fields than in molecular complex ones as a consequence of the extra non-ionizing energy dissipation modes of the later, thus usually a noble gas is used as the main filling gaseous radiation detectors. The choice of species of the noble gas is usually determined by the requirements on specific ionization and cost. Xenon or krypton, for example, have high specific ionization, but the rareness and cost of these gases is prohibitive for a lot of applications and so argon (Ar) has been chosen as the main filling for several detectors [13], as it did for the LCTPC.

As for the choice of addictive, carbon-tetrafluoride (CF_4) has been considered for the LCTPC mixture [14] because of its intrinsic desirable characteristics for high rate radiation detectors, such as, the highest known electron drift velocity and very low electron transverse diffusion, even in the absence of a magnetic field [13]. A third component is expected to be added and should be of methane (CH_4), ethane (C_2H_6) or isobutane (iso-C_4H_{10}). As we increase the molecule size of the third component, the gain for lower amplification electric fields increases [11] and the quencher efficiency also increases, at the cost of lower ions' drift velocity and lower lifetime due to processes of ageing of the detector [13].

In order to understand the ion transport properties in terms of three alternative gaseous mixtures for the LCTPC: Ar–CF_4–CH_4 (92-3-5), Ar–CF_4–C_2H_6 (94-3-3) and Ar–CF_4–iso-C_4H_{10} (95-3-2), several studies were conducted in our group, and the results will presented here.

1.5 Negative Ion Time Projection Chamber

The conventional TPC concept works very well in most of the high energy physics experiments but for low pressure or larger detectors, the electron diffusion effects on the widening of the signal obtained are much greater, limiting both the maximum spatial resolution achieved and the precision on the reconstruction of the tracks. As mentioned before there are two ways to suppress this problem, by applying

a magnetic field parallel to the drift direction, which is a expensive and, usually not practical solution, or by choosing a mixture with low electron diffusion coefficients at the cost of energy resolution.

A solution to this problem was found by Martoff et al. in 2000 [15] by introducing a modification to the conventional concept of the TPC, transforming it into a Negative Ion Time Projection Chamber (NITPC). The idea was to introduce an electronegative dopant which will quickly capture the electrons formed from ionization processes, generating anions which drift towards the anode. Near the anode, electrons are stripped from the anions originating an avalanche in the multiplication structure.

This technique can provide very high spacial resolution and near intrinsic energy resolution, since the ion diffusion coefficients are low and the ions' drift velocity is low enough, that at lower pressures, it is almost possible to count each ion individually, at the cost of lower response times. Also, since there is no need for a magnetic field to be applied for suppressing the ion diffusion, these detectors are more easily scalable [16].

The characteristics mentioned above make of NITPCs serious contenders for rare events physics such as dark matter and neutrinoless beta decay ($0\nu\beta\beta$) searches.

The first low pressure NITPC was developed for the DRIFT collaboration [16] for directional detection of dark matter by measuring the scattering of WIMPs (Weakly Interacting Massive Particles). This experiment seeks not only to reconstruct the energy of the WIMPs but also the direction of the nuclear recoils, in order to confirm their galactic origin. For that, the collaboration's last detector, the DRIFT-IId, makes us of a gaseous mixture 30:10:1 of CS_2:CF_4:O_2 where the fluorine atoms of the CF_4 molecules act as the target for the WIMP scattering and where CS_2 and O_2 act as the electronegative gases, producing several species of anions with slightly different ion velocities in order to reconstruct the nuclear recoils with sub-milliliter accuracy in the first non-background limited dark matter searches [17].

There is also a possibility of introducing NITPC in the searches for the neutrinoless double beta decay ($0\nu\beta\beta$) in the high pressure Xe enriched with ^{136}Xe by adding a dopant of electronegative gas with the main objective of counting the negative ions formed by electron attachment individually and so getting near intrinsic energy and spacial resolution. This alternative is referred as Ultra-High Resolution NITPC (UHR NITPC) [18].

Finally, other NITPCs detectors are under development for X-ray polarimetry and astronomical sources using nitromethane (CH_3NO_2) as the electronegative gas [19]. Gaseous detectors such as TPCs have been shown to have high detection efficiencies and to achieve high modulation factors but due the (great) detector dimensions required, the electron diffusion effects limit the highest possible spatial resolution that can be achieved, property which is critical in order to perform polarization measurements.

In order to attain accurate experimental measurements on ion mobility, and hopefully on diffusion, in mixtures of interest with electronegative dopant, a DP-IDC is under development, and details on its first prototype development efforts and first results will be presented here on a later chapter.

Chapter 2

Theoretical Background

2.1 Ion mobility

The first steps to measure ion mobility were taken at the end of the 19^{th} century and beginning of the 20^{th} century, when it was discovered that gases could pass from an insulating to a conducting phase through various processes. This change to conductive phase was attributed to the formation of electrons and ions, and led to the first studies about the mobility of ions.

When no electric field is applied, the ions' movement occurs in the opposite direction of their concentration gradient, which is referred to as diffusion.

Considering a group of ions originated in a weakly ionized gas moving under the influence of a low and uniform electric field, in these conditions, this group of ions will gain energy from the electric field, and lose energy by colliding with the neutral atoms and molecules, a process that is repeated continuously. Eventually a steady state is reached and the speed of this group of ions, also known as drift velocity, becomes proportional to the electric field, by a proportionality constant named mobility [1] [7].

$$v_d = KE \tag{2.1}$$

where v_d is the drift velocity, K is the mobility of the ion, usually expressed in units of $cm^2V^{-1}s^{-1}$, and E is the electric field.

To facilitate the comparison between mobility values obtained under different conditions and by different experiments, a commonly adopted way to represent it is by the so-called reduced mobility, K_0, presented as a function of reduced electric field in units of Townsend (1 Td = 10^{-17} Vcm^2).

$$K_0 = K\frac{N}{N_0} \tag{2.2}$$

where N is the gas number density in units of atoms or molecules cm^{-3} and N_0 is the Loschmidt number (N_0 = 2.6867 x 10^{25} m^3).

In the same way, the reduced electric field is defined by E/N and its dependence with the mobility

is derived from more advanced transport theories, such as Boltzmann-Enskog and Maxwell-Chapman methods, both leading to equation 2.1 in the low-field region where the energy is close to thermal.

2.2 Ion formation and transport properties

Ions and electrons on a gas mixture interact with the gas atoms or molecules by several processes. At room temperature, if no electric field is applied, electrons and ions tend to move randomly across the volume with thermal energy, drifting away from high density regions. Since the thermal velocity of electrons is much larger than that of ions, this effect will be more pronounced for electrons.

This thermal motion and diffusion causes ions and/or electrons to collide giving rise to charge transfer, electron attachment and recombination processes.

When a collision between a positive ion and a neutral molecule occurs, there is a possibility for the neutral to give and electron to the positive ion, reversing their charge polarities. In binary mixtures, the net positive charge will be due to the ions of the molecule with the lowest ionization energy.

The primary mechanism for negative ion production is electron attachment. As free electrons collide with neutral molecules of the gas, depending on their species, some have a tendency to attach them and form negative ions.

These already formed charged particles and molecules can be lost, again, by recombination processes, and therefore not contributing to the signal amplitude.

2.2.1 Diffusion

As explained above, when no electric field is applied, the ion movement occurs in the direction opposite to its concentration gradient.

Considering a point-like distribution at the initial instant, electrons and ions will spread from their initial point, as a function of time, following a normal spatial distribution with a standard deviation (σ) of the distribution [7] given by:

$$\sigma = \sqrt{2Dt} \tag{2.3}$$

where D is the diffusion coefficient.

When a low electric field is applied, this effect will still persist although with less impact. In this case diffusion can be characterized as either transversal (normal to E) or longitudinal (parallel to E).

2.2.2 Charge Transfer

In a charge transfer reaction an ion collides with a neutral atom/molecule, transferring some or all of its charge, depending on its ionization energy. In mixtures, usually, the charge is transfered to the lowest ionization energy atom/molecule [7].

$$A^+ + B \rightarrow A + B^+ \tag{2.4}$$

If the collision partners are identical, resonant charge transfer may occur [20].

$$A^+ + A \rightarrow A + A^+ \tag{2.5}$$

This resonant charge transfer does not change the concentration of the original ion but tends to reduce its mobility and so it frequently used to justifies the discrepancy between the experimental mobility value obtained and the one predicted by the relation given from the Langevin limit (Equation 2.13).

2.2.3 Electron attachment

Electron attachment is a process which occurs when an electronegative atom/molecule collides with an electron and originates a negative ion.

This process can be either non-dissociative or dissociative, depending if it maintains or destroys some of the chemical bonds in the molecule [21], as shown below.

If a thermal electron is captured by the atom/molecule, it produces the corresponding atomic/molecular anion by:

$$A + e^- + M \rightarrow A^- + M \tag{2.6}$$

This non-dissociative reaction is called resonant electron capture and M is a third body required to conserve momentum and energy.

However, when molecules and high energy electrons are involved, dissociative processes can occur in which the molecule loses its bonds and produces one atomic ion and one neutral atom.

$$AB + e^- \rightarrow A^- + B \tag{2.7}$$

This process is called dissociative electron capture.

At even higher electron energies, the collision between the electron and the molecule can originate one positive ion and one negative ion, releasing an electron with lower energy than before.

$$AB + e^- \rightarrow A^- + B^+ + e^- \tag{2.8}$$

This process is called ion pair formation.

Typical studies on ion mobility with our experimental system are for electron energies between 10-30 eV and so dissociative processes are more likely to occur.

2.2.4 Cluster formation

In this process, a central ion binds with one or more molecules forming cluster ions of different orders (depending on the number of molecules that bind with the ion), due to the attractive force between the ion charge and a polarized molecule. The typical bonding energy of these molecules is in between that of the chemical and the van der Wall bonds (0.1 - 1.5 eV).

The reaction process for positive [22] and negative [23] ion cluster seems to be similar and in the first order case can be described as:

$$A^+ + B + M \rightarrow B.A^+ + M \tag{2.9}$$

$$A^- + B + M \rightarrow B.A^- + M \tag{2.10}$$

These cluster ions are heavier than the original and so tend to reduce the measured mobility.

2.2.5 Recombination

Recombination is the process in which an ion neutralizes by colliding either with an ion of opposite polarity or with an electron.

In the first case, the extra electron present in the negative ion is transfered for the positive ion, neutralizing both molecules.

$$A^- + B^+ \rightarrow A + B \tag{2.11}$$

In the second case, an electron is captured by the positive ion, originating a neutral molecule.

$$e^- + A^+ \rightarrow A \tag{2.12}$$

In high concentrations of negative ions, the neutralization between two ions is dominant, since its cross section is usually higher [7].

This recombination effect is responsible for diminishing the signal collected and is predominant when no electric field is applied. As the electric field increases, this effect becomes negligible.

2.3 Langevin theory

In 1905, French physicist Paul Langevin described the mobility of ions in the case that the ion-neutral interaction potential is mainly due to the polarization of the neutral by the electric field of the ion, which can be referred to as the Polarization effect [24]. Langevin considered ions as hard elastic spheres and the neutral gas atoms/molecules as polarizable in the electric field of the ions. In conditions of low E/N, low temperature and low pressure, the polarization attraction due to the charge-induced dipole force is dominant over the hard sphere elastic repulsion between ion and gas neutral, and the value of the mobility in Langevin's limit is defined by the following equation:

$$K_0 = 13,88(\frac{1}{\alpha\mu})^{1/2} \tag{2.13}$$

where α is the neutral polarizability in cubic angstroms $Å^{-3}$ of the neutral atom/ molecule (in Table 2.1 values on the neutral polarizability of the gases studied is this thesis are summarized) and μ is the ion-neutral reduced mass in atomic mass units, given by:

$$\mu = \frac{mM}{m+M} \tag{2.14}$$

where m is the mass of the ion and M the mass of the neutral molecule/ atom.

This approximation, is in fair agreement with the experimental values obtained in our experimental system: low pressure, low E/N and low temperature (room temperature).

However, even in the conditions mentioned above, the validity of the Langevin formula is weakened when the gas atoms or molecules are weakly polarizable, or when molecules are large. In these circumstances, the hard-sphere elastic scattering becomes dominant over the charge-induced dipole force, and the limit starts depending on the ion and gas radii, which usually is not known precisely [20].

Table 2.1: Neutral polirizabilities for different gases: Ar, CF_4, CH_4, C_2H_6, iC_4H_{10} and N_2 (references in the last column).

Neutral	Polarizability ($Å^{-3}$)	Ref
Ar	1.64±0.01	[25]
CF_4	3.86±0.01	[26]
CH_4	2.62±0.01	[27]
C_2H_6	4.47±0.01	[27]
iC_4H_{10}	8.14±0.01	[27]
N_2	1.95±0.10	[28]

2.4 Blanc's law

While working on the mobility of ions in binary gas mixtures, Blanc found an empirical law, that has proven to be applicable when determining ion mobility in gas mixtures. Blanc's law states that the mobility of a group of ions in mixtures of two gases 1 and 2, K_0, is given by:

$$\frac{1}{K_{0mix}} = \frac{f_1}{K_{0g_1}} + \frac{f_2}{K_{0g_2}} \tag{2.15}$$

where K_{0mix} is the reduced mobility of the ion in the binary mixture; K_{0g1} and K_{0g2} the reduced mobility of that same ion in an atmosphere of 100% of gas 1 and 2 respectively; f_1 and f_2 are the molar fraction of each gas in the binary mixture [29].

For ternary mixtures, it was assumed a form of the Blanc's law in order to obtain the theoretical mobility of the ions, in which the mobility of a group of ions in mixtures of three gases 1, 2 and 3, K_0, is given by:

$$\frac{1}{K_{0mix}} = \frac{f_1}{K_{0g_1}} + \frac{f_2}{K_{0g_2}} + \frac{f_3}{K_{0g_3}} \tag{2.16}$$

where K_{0mix} is the reduced mobility of the ion in the binary mixture; K_{0g1}, K_{0g2} and K_{0g3} the reduced mobility of that same ion on a atmosphere of 100% of gas 1, 2 and 3 respectively; f_1, f_2 and f_3 are the molar fraction of each gas in the ternary mixture.

In our work, K_{gi} in Blanc's law are usually obtained either by using experimental values from literature

or, when not possible, by extrapolating from existing experimental data or from the Langevin theory.

This relationship holds true while the effects of the charge transfer reaction are negligible compared to the polarization attraction and short-range repulsion between ions and atoms/molecules effects.

2.5 Collision Theory and Chemical Kinetics

As described earlier, reactions in the gas volume between ions and molecules/atoms are explained by the collision between the reagents. This is the main principle of the collision theory that is is used to explain the chemical kinetics [30].

However, these reactions correspond to statistical processes that depend both on the concentration of the reactants and in the reaction rates.

We can represent a two body chemical reaction between two different species, A and B, which produces two products C and D by:

$$aA + bB \rightarrow cC + dD \tag{2.17}$$

where a, b, c and d are the stoichiometric coefficient of their correspondent species.

The kinetics of these reactions can be described by a reaction rate R, which is directly proportional to the negative or positive of the rate of change for the concentration of the reactants or products with time, respectively, as defined in Equation 2.18.

$$R = -\frac{1}{a}\frac{d[A]}{dt} = -\frac{1}{b}\frac{d[B]}{dt} = \frac{1}{c}\frac{d[C]}{dt} = \frac{1}{d}\frac{d[D]}{dt} \tag{2.18}$$

Where $[A]$, $[B]$, $[C]$ and $[D]$ are the concentrations of the reactants A and B, and of the products C and D. The reaction rate units depend on the type of the reaction.

However, the tabulated values are frequently given in terms of reaction constant k, which relates with the reaction rate through:

$$R = k[A]^m[B]^n \tag{2.19}$$

Where m and n are the order of the reaction in the reactants A and B. Usually the stoichiometric a and b are used to determine the reaction rate order of the reactants, but true values can only be obtained experimentally.

In first order reactions, the reaction rate is described by:

$$R = k[A] = -\frac{d[A]}{dt} \tag{2.20}$$

And by integration of this equation, we can obtain the temporal evolution of the concentration of A, as long as we know its initial concentration:

$$[A]_t = [A]_0 e^{-kt} \tag{2.21}$$

where $[A]_t$ is the concentration of the reactant A at instant t and $[A]_0$ its the initial one.

This result can be easily used to compute the temporal evolution of the products. Which, in first order, is:

$$[C]_t = [C]_0 + [A]_0(1 - e^{-kt}) \tag{2.22}$$

where $[C]_0$ and $[C]_t$ are the initial concentration of the product C and its value at instant t, respectively

For higher order reactions, two-body and three-body ones, the respective reaction rates of second and third order are:

$$R = -k[A][B] = \frac{d[A]}{dt} \tag{2.23}$$

and

$$R = -k[A][B][C] = \frac{d[A]}{dt} \tag{2.24}$$

As with each order, there is an increase in complexity of the differential equations, we use a pseudo-first-order method to solve them as an approximation. In the case of the two-body reaction, if we assume $[A] >> [B]$, then $[A]$ stays fairly constant during the reaction and we can write equation 2.23 as:

$$R = -k_{2n}[A][B] = -k_n[B] = \frac{d[B]}{dt} \tag{2.25}$$

where $k_n = k_{2n}[A]$ and the lower index is the reaction order.

In a similar way, for a three-body reaction, if we assume $[A], [C] >> [B]$, then the concentration of A and C remain constant throughout the reaction and we can write equation 2.24 as:

$$R = -k_{3n}[A][B][C] = -k_n[B] = \frac{d[B]}{dt} \tag{2.26}$$

where $k_n = k_{3n}[A][C]$.

Since the collision of more than three bodies at once is highly improbable, chemical reactions of higher orders are not reported in the literature.

When reaction rates are known, we can use this knowledge to predict the evolution of the concentration of ions during their drift time. However these calculations are only as accurate and precise as the reaction constants used to compute them, thus some level of deviation is always expected.

Chapter 3

Positive ion mobility studies in gaseous mixtures of interest

In the first part of this chapter the experimental system developed by P. N. B. Neves [31], as well as the methods and techniques, used to conduct studies on the mobility of positive ions in gases are described.

In the second part, experimental results on ion mobility in several pure gases and binary mixtures will be briefly reviewed or presented and discussed in order to understand the behavior in terms of ion transport properties in the alternative mixtures expected for the LCTPC, whose results will be presented in the end of this chapter. A discussion of the results in Ar–N_2 mixtures is also presented.

3.1 Experimental system

Between 2005 and 2009, P. N. B. Neves [31] developed a new experimental technique for measuring positive ion mobility in their parent gases with the primary objective of distinguishing the atomic and dimer ions in rare gases [32].

Since 2013, this technique has been applied to study ion mobility in mixtures of rare gases with molecular additives for total pressures typically ranging from 2 to 30 Torr and for reduced electric fields (E/N) between 5 and 45 Td.

The range of the E/N values used to determine the ions' mobility is limited by two factors: one is the occurrence of electric discharges at higher E/N, and the other is the deterioration of the time of arrival spectra for values below 5 Td, which has been attributed to collisions between the ions and impurity molecules, since the ions' drift time becomes longer for these lower E/N.

This experimental system and associated analysis have proven to be a valid solution for the ion identification problem, having resulted several scientific papers already published [20, 22, 32, 33, 34, 35, 36, 37, 38, 39, 40, 41, 42, 43, 44, 45, 46, 47].

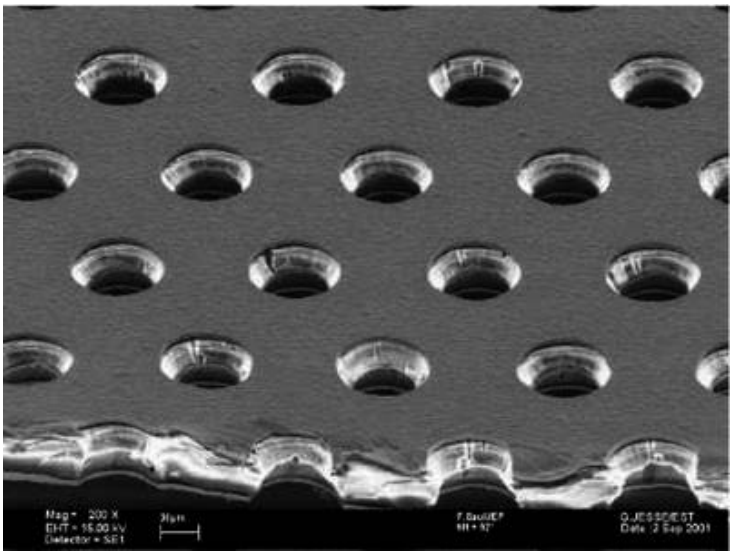

Figure 3.1: GEM surface (extracted from [48]).

3.1.1 Ion production method

In the present system, ions are produced in a structure composed by a Gas Electron Multiplier (GEM) with a Cesium Iodide (CsI) film deposited on top of it.

The Gas Electron Multiplier (GEM) consists on a thick Kapton foil, that acts as an insulator, clad in electrochemically deposited copper on both sides, with holes hatched in a regular pattern in this structure [49], as shown in Figure 3.1 where a GEM surface image taken with an electron microscope is presented. When a voltage difference is applied across the two copper layers and the in presence of certain gases, a single electron entering any hole will create an avalanche, thus producing electrons and positive ions which will drift in opposite directions.

At our working pressure (of few Torr), the great advantage of using the GEM as an ion source is that ions are produced in a well defined position inside the GEM holes, and with a well defined energy, since the maximum energy gained by the electrons throughout their path is roughly equivalent to the voltage difference between top and bottom electrodes of the GEM. Therefore allowing to predict which primary ions can be originated by electron impact ionization of the gas atoms/molecules, as well as their relative abundance.

In order to produce the electrons required for the impact ionization of the gas atoms/ molecules in the GEM holes, a 250 nm thick CsI film was vacuum evaporated on the top copper electrodes of the GEM. This film acts as a photocathode, converting the incident photon flux emitted from a VUV Xe lamp located above the GEM structure into photoelectrons, that will be accelerated through the GEM holes, resulting in ionization of some of the gas atoms/molecules.

One of the main drawbacks of using a deposited photocathode, such as CsI, is that several ageing effects that can cause the deterioration of its performance (*eg.* quantum efficiency) are known, one example is the exposure to the air humidity. For this reason, the system assembly time must be minimized to reduce the exposure of the CsI film to the air humidity.

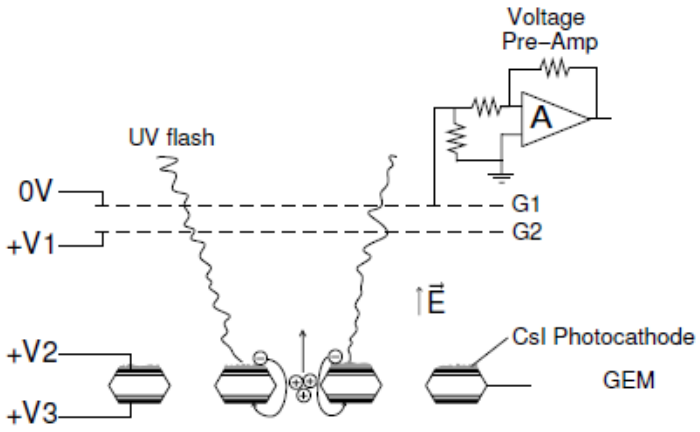

Figure 3.2: Schematic diagram of the system working principle (extracted from [31]).

3.1.2 Working principle

Every measurement starts with a flash of a Xe VUV Hamamtsu (model L2439) lamp, that emits photons with a 10 Hz frequency and a pulse duration shorter than 0.5 μs, which releases photoelectrons from the CsI photocathode deposited on the top electrode of the GEM. These photoelectrons will then gain energy from the electric field, drifting through the GEM holes, ionizing some of the gas atoms/molecules inside them when the energy of the electrons becomes higher than the gas ionization threshold.

While electrons are collected at the bottom electrode of the GEM, the ions produced during the avalanche start drifting towards grids G2 and G1, distanced of about 0.5 $\pm$ 0.1 mm, under the influence of a uniform electric field. The uniformity of this drift electric field is ensured by several equally-spaced field rings along the drift portion of the detector, biased through a voltage divider.

In this system, grid G2 plays an important role as it acts as a Frisch grid, preventing the signal induction due to the drifting ions in the collecting grid G1, while also guaranteeing a uniform reduced electric field in the drift region.

When the group of ions crosses grid G2, a signal is then induced in grid G1. This signal is converted from current to voltage by a high density charge AmpTEK® (model A250F/NF) pre-amplifier with the resistors chosen to maximize the gain while minimizing noise [31]. An average of 128 pulses, to filter signal instabilities, is then recorded in a digital oscilloscope (Tektronix TDS 1012) and finally fed to a PC for processing and storage. The background is also recorded without biasing the GEM, $i.e$ without the presence of drifting ions.

After the signal and the electronic background are recorded, the background is then subtracted from the signal and the peaks present in the time-of-arrival spectra that correspond to positive ions that arrived to G1, are identified. By fitting Gaussian curves to the spectrum obtained in a MATLAB® application developed in our group, the information on the peak centroids can be retrieved, which corresponds to the average drift time of the ion's distribution, whose initial instant is defined by the flash of the VUV lamp.

The drift velocity of the group of ions can then be calculated by knowing the distance traveled by the

group of ions (42.73mm) and the ions' drift time. Then, using Equation 2.1, the mobility of the group of ions can be obtained.

3.1.3 Ion identification process

As the experimental system does not provide direct identification of the ions responsible for the peaks in the time-of-arrival spectra, an indirect method for this identification problem was devised, which is based on some of the system features.

First, the GEM is a very practical ion source because it is possible to define the maximum energy acquired by the electrons inside the holes at lower pressures (of few Torr), as well as the signal gain, by defining the voltage difference applied across the GEM electrodes (V_{GEM}). Thus, with the knowledge of the partial cross-sections for electron impact ionization, which are usually very accurate, the species of ions that are formed (primary ions) and their initial concentrations can be estimated.

Since these primary ions can undergo secondary reactions with the gas atoms/molecules during their drift towards grids G1 and G1, it is necessary to understand the possible ionization products, product distributions and rate constants for the collisions of these ions with the gas atoms/molecules.

When available, the knowledge of both total and partial ionization cross-sections for electron impact ionization, and the ionization products, product distributions and rate constants of the secondary reactions involved, can be used to calculate the final ion fraction arrival at the collecting grid with good accuracy for the ions' drift time measured. Comparing the relative concentration of the final ions species with the relative areas of the signal peaks, variables that in fair agreement, can help us to identify the possible ions responsible for the peaks present in time-of-arrival spectra.

Finally, we use the Langevin limit formula (equation 2.13) and Blanc's law (equation 2.15), in the case of mixtures, for identification of the ions. However, when using these formula for identification of the ions responsible present, it should be taken into account that the validity of the Langevin's formula is limited for weakly polarizable atoms/molecules and for massive molecules [20].

3.2 Experimental results on positive ion mobility

3.2.1 Pure gases

In this section, the experimental results on ion mobility in pure gases like argon (Ar), carbon tetrafluoride (CF_4), methane (CH_4), ethane (C_2H_6) and nitrogen (N_2) will be reviewed and the results in pure isobutane (iso-C_4H_{10}) will be presented and discussed. This knowledge is of uttermost importance in order to understand and interpret the time-of-arrival spectra obtained in mixtures of various gases.

Argon (Ar)

In previous works in pure argon (Ar) [32], two peaks were observed for a GEM voltage of about 20 V. The ions responsible for the peaks are the atomic ion (Ar^+), which results from direct electron impact ionization, and the dimer ion (Ar_2^+), which is a result of a three-body collision between Ar^+ and Ar atoms.

Since Ar_2^+ ions are two times heavier than Ar^+ ions, it would be expected that they would present a lower mobility. However, as a consequence of the resonant charge transfer process between Ar^+ ions and Ar atoms, the atomic argon ions are slowed down (K_{01} = 1.57 $cm^2V^{-1}s^{-1}$), appearing in the drift spectra after the dimer one (K_{02} = 1.92 $cm^2V^{-1}s^{-1}$), and so with lower mobility. A summary of possible reactions in pure Ar and respective rate constants or cross section for electron impact ionization at 25 eV, as well as the appearance energy of the primary ions, is presented in Table 3.1.

For the purpose of this work, the mobilities of the Ar^+ and Ar_2^+ ions in pure Ar were taken from [32].

Table 3.1: Summary of possible reactions in pure Ar and respective rate constants or cross sections for electron impact ionization at 25 eV (references on the last column).

Reaction	Rate Constant	Cross Section (25 eV)	A.E.(eV)	Ref.
e^- + Ar $\rightarrow$ Ar^+ + $2e^-$	-	$1.24\pm0.06\times10^{-16}$ cm^2	15.70	[50, 51]
Ar^+ + Ar $\rightarrow$ Ar + Ar^+	4.6×10^{-10} $cm^3.s^{-1}$	-	-	[20]
Ar^+ + 2Ar $\rightarrow$ Ar_2^+ + Ar	2.2×10^{-31} $cm^6.s^{-1}$	-	-	[52]

Carbon tetrafluoride (CF_4)

In pure carbon tetrafluoride (CF_4) [41] only one peak was observed for a reduced electric field of 15 Td, 8 Torr, a V_{GEM} of 25 V at room temperature (293 K). As result of the primary ionization in the GEM holes, several ions (CF_3^+, CF_2^+, CF^+, F^+ and C^+) are produced, as can be seen in Table 3.2, where the ionization products and cross sections for electron impact ionization for 25 eV in pure CF_4 [53] are summarized. Looking at the same table, it is also possible to notice that CF_3^+ will be the most abundant one (it represents about 96% of ion production for V_{GEM} of 25 V). As there were no charge transfer reactions between the ions and gas molecules found in literature at our experimental conditions and since the ion mobility computed through the Langevin theory for CF_3^+ agrees with experimental results, it was considered that the ion responsible for the peak should indeed be CF_3^+.

The mobility obtained in this work (1.12 $cm^2V^{-1}s^{-1}$), for low reduced electric field (E/N of 10 Td), is in good agreement with the one expected from the Langevin theory (1.12 $cm^2V^{-1}s^{-1}$), although it deviates from those obtained by other authors (0.96 $cm^2V^{-1}s^{-1}$) [54, 55]. This difference can be explained by formation of $CF_3^+(CF_4)$ clusters [56], which is pressure dependent and would be favored at higher pressures (close to the atmospheric one) and whose expected value is close to those observed by these authors.

Table 3.2: Ionization products, their cross sections for electron impact ionization for 25 eV in pure CF_4 [53] and respective appearance energies (A.E.) [57].

Reaction	Cross Section (10^{-16} cm^2)	A.E.(eV)
$e^- + CF_4 \rightarrow CF_3^+ + F + 2e^-$	1.011	15.69
$e^- + CF_4 \rightarrow CF_2^+ + 2F + e^-$	0.038	21.47
$e^- + CF_4 \rightarrow CF^+ + F + e^-$	0.0017	29.14
$e^- + CF_4 \rightarrow C^+ + 2F_2 + e^-$	0.0007	34.77
$e^- + CF_4 \rightarrow F^+ + CF_3 + e^-$	0.0007	35

Methane (CH_4)

In previous work for pure methane (CH_4), only one peak was observed in the time-of-arrival spectrum from zero-field up to 15 Td, and two peaks for E/N greater than 15 Td, while in other papers, in different pressure conditions, three are reported as discussed in [36].

Table 3.3: Ionization products, cross sections for electron impact ionization at 25 eV [58] and respective appearance energies (A.E.) [59] of ions in pure CH_4.

Reaction	Cross Section (10^{-16} cm^2)	A.E.(eV)
$e^- + CH_4 \rightarrow CH_4^+ + 2e^-$	1.29	12.7
$e^- + CH_4 \rightarrow CH_3^+ + H^- + e^-$	0.923	13.7
$e^- + CH_4 \rightarrow CH_3^+ + H_2 + 2e^-$		14.3
$e^- + CH_4 \rightarrow CH_2^+ + H^- + H_2 + e^-$	0.559	15.1

Table 3.4: Ionization products, product distribution and rate constants for the collisions of the primary ions of CH_4 with the CH_4 molecules [60].

Reaction	Prod. Dist.	Rate Const. (10^{-9} cm^{3}s^{-1})
$CH_4 + CH_4^+ \rightarrow CH_5^+ + CH_3$	1.00	1.15±0.05
$CH_4 + CH_3^+ \rightarrow C_2H_5^+ + H_2$	1.00	0.96±0.05
$CH_4 + CH_2^+ \rightarrow C_2H_2^+ + 2H_2$	0.12	1.20±0.05
$CH_4 + CH_2^+ \rightarrow C_2H_3^+ + 2H_2 + H$	0.22	1.20±0.05
$CH_4 + CH_2^+ \rightarrow C_2H_4^+ + H_2$	0.42	1.20±0.05
$CH_4 + CH_2^+ \rightarrow C_2H_5^+ + H$	0.38	1.20±0.05
$CH_4 + C_2H_5^+ \rightarrow C_3H_7^+ + H_2$	1.00	0.000011±0.000001
$CH_4 + C_2H_3^+ \rightarrow C_3H_5^+ + H_2$	1.00	0.22±0.01
$CH_4 + C_2H_2^+ \rightarrow C_3H_4^+ + H_2$	0.21	0.84±0.01
$CH_4 + C_2H_2^+ \rightarrow C_3H_5^+ + H$	0.79	0.84±0.01

Several primary ions are produced by electron impact ionization in CH_4 molecules depending on the energy gained by the electrons inside the GEM holes. For a V_{GEM} of 25 V, the three main primary ions being formed are CH_4^+ (produced more abundantly), CH_3^+ and CH_2^+, as can be seen in Table 3.3, where the ionization products, cross sections for electron impact ionization at 25 eV and respective appearance energies (A.E.) are summarized. These primary ions will further react with CH_4, leading to the formation of CH_5^+, in the case of the CH_4^+ primary ions, or leading to increasingly complex ions typically 2-carbon ($C_2H_n^+$) and 3-carbon ($C_3H_n^+$) ion groups, in the case of the CH_3^+ and CH_2^+ primary ions, as can be seen in Table 3.4 where the ionization products, product distribution and rate constants for the collision of the primary ions with the molecules in pure CH_4 are summarized. This helps to explain the origin of the peaks: the first, with higher mobility, comes from CH_5^+ ions and the other, with lower mobility, is due to more massive ion groups, $C_2H_n^+$ and $C_3H_n^+$.

For the purpose of this work, the mobilities of the CH_5^+ and $C_2H_n^+$/$C_3H_n^+$ ions in pure CH_4 were taken from [36].

Ethane (C_2H_6)

Table 3.5: Ionization products, cross sections for electron impact ionization at 25 eV [61] and respective appearance energies (A.E.) [59] of ions in pure C_2H_6.

Reaction	Cross Section (10^{-16} cm^2)	A.E.(eV)
$e^- + C_2H_6 \rightarrow C_2H_6^+ + 2e^-$	0.475	11.57
$e^- + C_2H_6 \rightarrow C_2H_5^+ + H^- + e^-$	0.346	12.08
$e^- + C_2H_6 \rightarrow C_2H_4^+ + H_2 + e^-$	1.43	11.81
$e^- + C_2H_6 \rightarrow C_2H_3^+ + H^- + H_2 + e^-$	0.362	14.50
$e^- + C_2H_6 \rightarrow C_2H_2^+ + 2H_2 + 2e^-$	0.225	14.41
$e^- + C_2H_6 \rightarrow CH_3^+ + CH_3 + e^-$	0.070	13.72

In pure ethane (C_2H_6) two peaks were observed and reported in a previous work [34]. For 25 eV, the primary ions being formed include a variety of ions that range from CH_3^+ to $C_2H_2^+$ all the way to $C_2H_6^+$, as can be seen in Table 3.5 where the ionization products, cross sections for electron impact ionization at 25 eV and respective appearance energies (A.E.) of ions in pure ethane are summarized. These ions will further react with ethane leading to increasingly complex ions typically with 3-carbon ($C_3H_n^+$) and 4-carbon ($C_4H_n^+$) groups. The ionization products, product distribution and rate constants for the collisions of molecules with the primary ions in C_2H_6 are summarized in Table 3.6. Finally, as expected from theory, the lighter ion group displays higher mobility while the heavier group displays lower mobility.

For the purpose of this work, the mobilities of the $C_3H_n^+$ and $C_4H_n^+$ ions in pure C_2H_6 were taken from [34].

Table 3.6: Ionization products, product distribution and rate constants for the collisions molecules and the primary ions in C_2H_6 [60].

Reaction	Prod. Dist.	Rate Const. (10^{-9} cm^{3}s^{-1})
$C_2H_6 + C_2H_6^+ \rightarrow C_3H_8^+ + CH_4$	0.42	0.019±0.001
$C_2H_6 + C_2H_6^+ \rightarrow C_3H_9^+ + CH_3$	0.58	0.019±0.001
$C_2H_6 + C_2H_5^+ \rightarrow C_4H_9^+ + H_2$	1.00	0.040±0.003
$C_2H_6 + C_2H_4^+ \rightarrow C_3H_6^+ + CH_4$	0.07	0.0053±0.0001
$C_2H_6 + C_2H_4^+ \rightarrow C_3H_7^+ + CH_3$	0.93	0.0053±0.0001
$C_2H_6 + C_2H_3^+ \rightarrow C_2H_5^+ + C_2H_4$	0.47	0.62±0.03
$C_2H_6 + C_2H_3^+ \rightarrow C_3H_5^+ + CH_4$	0.40	0.62±0.03
$C_2H_6 + C_2H_3^+ \rightarrow C_4H_7^+ + H_2$	0.13	0.62±0.03
$C_2H_6 + C_2H_2^+ \rightarrow C_2H_4^+ + C_2H_4$	0.18	1.46±0.06
$C_2H_6 + C_2H_2^+ \rightarrow C_2H_5^+ + C_2H_3$	0.09	1.46±0.06
$C_2H_6 + C_2H_2^+ \rightarrow C_3H_3^+ + CH_3 + H_2$	0.06	1.46±0.06
$C_2H_6 + C_2H_2^+ \rightarrow C_3H_5^+ + CH_3$	0.54	1.46±0.06
$C_2H_6 + C_2H_2^+ \rightarrow C_4H_5^+ + H_2 + H$	0.05	1.46±0.06
$C_2H_6 + C_2H_2^+ \rightarrow C_4H_7^+ + H$	0.09	1.46±0.06

Isobutane (iso-C_4H_{10})

The mobility of isobutane (iso-C_4H_{10}) ions in their parent gas was studied for different reduced electric fields (E/N) ranging from 10 to 45 Td, pressure ranging from 6 to 10 Torr, and for a V_{GEM} of 25 at room temperature.

In this work two peaks were observed between 10 and 40 Td, and only one for 45 Td for 8 Torr pressure at room temperature. We believe that this difference is due to the lower ions' drift time for higher E/N. Also, with increasing E/N, the peaks became sharper, which may also be due to the corresponding decrease in the ions' drift time, leading to less diffusion. In Figure 3.3, the time-of-arrival spectra (average of 128 pulses) in pure iso-C_4H_{10} recorded for a total pressure of 8 Torr, E/N of 15 Td and of 45 Td, V_{GEM} of 25 V and room temperature (293K) are presented, showing the referred peaks.

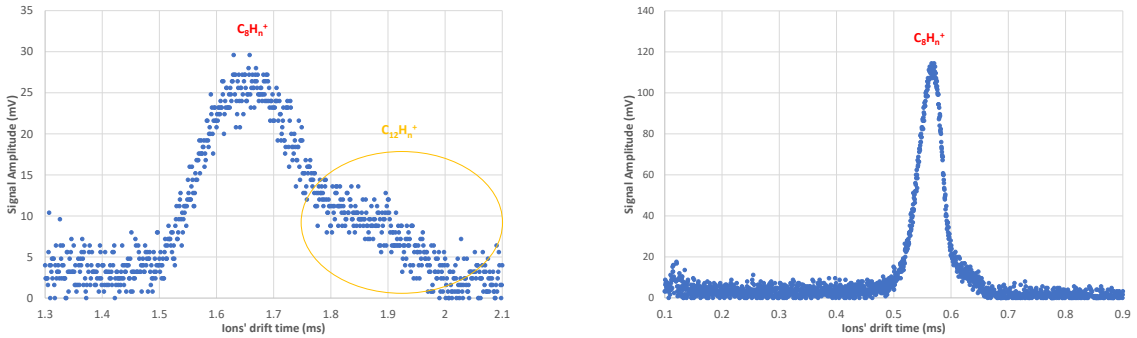

(a) (b)

Figure 3.3: Time-of-arrival spectra (average of 128 pulse) of iso-C_4H_{10} recorded for a total pressure of 8 Torr, reduced electric field of 15 Td (a) and of 45 Td (b), V_{GEM} of 25 V and room temperature (293K).

Ionization processes in isobutane are complex, not only due to the number and species of the primary ions produced which depend on the electron energy inside the GEM holes, but also because of the reaction paths available between each possible primary ion with a parent molecule. Also, relevant information on the partial cross-sections for electron impact ionization and reaction rates for reactions between primary ions and molecules in isobutane is scarce, which make this analysis more difficult.

Considering the mass spectrometer data from [62], for a electron energies up to 25 eV, most of the primary ions being formed are expected to be of $C_3H_n^+$, with n = 5, 6 or 7 and of $C_2H_3^+$. In addition, simulations on the isomer effect on butane-like molecules on the total ionization cross sections by electron impact show very small differences up to 25 eV [63]. Therefore we can expect that the distribution of the primary ions not to be very different from the one obtained for the same V_{GEM} in isobutane. Still, some differences are anticipated, as the fraction of $C_2H_4^+$ and $C_2H_5^+$ is expected to be greater in butane than in isobutane [62]. However effects of those differences in the primary ions fractions will be overcome by secondary reactions leading to molecules of about the same size. The primary ions, the cross sections for electron impact ionization at 25 eV and their respective appearance energies (A.E.) of ions in pure isobutane (cross-sections are from electron impact in butane, as explained earlier) can be found in Table 3.7.

Table 3.7: Primary ions, cross sections for electron impact ionization at 25 eV (considered similar to those of from butane) [64] and respective appearance energies (A.E.) [62] of ions in pure isobutane (cross-sections from electron impact in butane).

Ion Produced	Cross Section (10^{-16} cm^2)	A.E.(eV)
$C_2H_3^+$	0.29	-
$C_2H_4^+$	0.47	14.07
$C_2H_5^+$	0.62	13.80
$C_3H_3^+$	0.10	-
$C_3H_5^+$	0.81	14.55
$C_3H_6^+$	0.46	10.88
$C_3H_7^+$	2.40	11.16
t-$C_4H_9^+$	0.11	11.60
iso-$C_4H_{10}^+$	0.38	10.23

Those primary ions will further react with the isobutane molecules, leading to the formation of secondary ions with a ternary structure of $C_4H_9^+$ (t-$C_4H_9^+$) and iso-$C_4H_{10}^+$ [65]. Since it was concluded that reaction rates do not change significantly from butane to isobutane [66], recent experimentally obtained reaction rates (k) [64] were taken into account in order to understand the final distribution of the ions arriving at the collecting grid. The ionization products, their distribution and rate constants for isobutane (considered similar to those of butane) for these reactions between primary ions and molecules of isobutane are summarized in Table 3.8.

Table 3.8: Ionization products, product distribution and rate constants for reactions between primary ions and molecules in isobutane (considered similar to those of butane [64]).

Reaction	Prod. Dist.	Rate Const. (10^{-9} cm^{3}s^{-1})
iso-C_4H_{10} + $C_2H_3^+ \rightarrow C_3H_7^+$ + C_3H_6	0.35	1.3±0.3
iso-C_4H_{10} + $C_2H_3^+ \rightarrow C_4H_9^+$ + C_2H_4	0.65	1.3±0.3
iso-C_4H_{10} + $C_2H_4^+ \rightarrow C_3H_7^+$ + $C_3H_6$7	0.01	1.5±0.3
iso-C_4H_{10} + $C_2H_4^+ \rightarrow C_4H_8^+$ + C_2H_6	0.14	1.5±0.3
iso-C_4H_{10} + $C_2H_4^+ \rightarrow C_4H_9^+$ + C_2H_5	0.57	1.5±0.3
iso-C_4H_{10} + $C_2H_4^+ \rightarrow C_4H_{10}^+$ + C_2H_4	0.28	1.5±0.3
iso-C_4H_{10} + $C_2H_5^+ \rightarrow C_4H_9^+$ + C_2H_6	1.00	1.0±0.2
iso-C_4H_{10} + $C_3H_5^+ \rightarrow C_4H_9^+$ + C_3H_6	1.00	0.45±0.09
iso-C_4H_{10} + $C_3H_6^+ \rightarrow C_4H_8^+$ + C_3H_8	0.93	0.78±0.16
iso-C_4H_{10} + $C_3H_6^+ \rightarrow C_4H_9^+$ + C_3H_7	0.07	0.78±0.16
iso-C_4H_{10} + $C_3H_7^+ \rightarrow C_4H_9^+$ + C_3H_8	1.00	0.37±0.07

These reactions between primary ions and molecules in isobutane, leading to 4-carbon ion groups ($C_4H_n^+$) which will be called secondary ions, have a relatively high rate constant (about 10^{-9} cm^{-3}s^{-1}) thus for low total pressures and/or drift distances, these will be the ions that will be responsible for the peaks on the time-of-arrival spectra. However, for higher pressures and/or drift distances, those secondary ions will undergo reactions with a rate constant five orders of magnitude lower than the

previous ones (10^{-14} $cm^{-3}s^{-1}$), that will lead to the formation of much heavier 8-carbon group ions ($C_8H_n^+$). Finally, these molecular ions will proceed to react with isobutane molecules leading to the formation of 12-carbon group ions ($C_{12}H_n^+$), with even lower rate constants (about 10^{-15} $cm^{-3}s^{-1}$). The ionization products, product distribution and rate constants of these slower reactions are summarized in Table 3.9.

Table 3.9: Ionization products, product distribution and rate constants for reactions between the secondary ions and molecules in isobutane [65].

Reaction	Rate Const. (10^{-14} cm^3s^{-1})
iso-$C_4H_{10}^+$ + iso-C_4H_{10} $\rightarrow$ $C_8H_{18}^+$ + H_2	4.2±0.8
t-$C_4H_9^+$ + iso-C_4H_{10} $\rightarrow$ $C_8H_{17}^+$ + H_2	4.7±0.8
$C_8H_{18}^+$ + iso-C_4H_{10} $\rightarrow$ $C_{12}H_{26}^+$ + H_2	0.30±0.06
$C_8H_{17}^+$ + iso-C_4H_{10} $\rightarrow$ $C_{12}H_{25}^+$ + H_2	0.28±0.0.06

Using both the initial primary ions' distribution and the rate constants for the possible secondary ions, we can estimate the evolution of the ions drifting in the gas as a function of time. The results of these calculations at a total pressure of 8 Torr are displayed in Figure 3.4. It can be seen that two types of ions should arrive to the collecting grid, $C_8H_n^+$ and $C_{12}H_n^+$, since the drift time of the ions ranges from about 0.55 to 2.5 ms, as E/N ranges from 45 to 10 Td, respectively. We conclude that as the ions' drift time decreases, with increasing E/N, the fraction of $C_{12}H_n^+$ ions arriving also decreases, which explains why only one peak is present for E/N of 45 Td. However, no exact conclusions about the fraction of the ions arriving at the collecting grid should be drawn from these calculations because of both high uncertainties on the rate constants (of about 20%) and the differences between the cross sections for electron impact and the rate constants for butane and isobutane which help predict the fraction of primary and secondary ions, respectively. Also, the ions identified as $C_{12}H_n^+$ have traveled as $C_8H_n^+$ in part their drift, thus influencing the measured mobility may be influenced their predecessor ions. In fact, adding to the fact that higher drift times should lead to higher diffusion effects, this may explain why the peaks are broader at lower reduced electric fields.

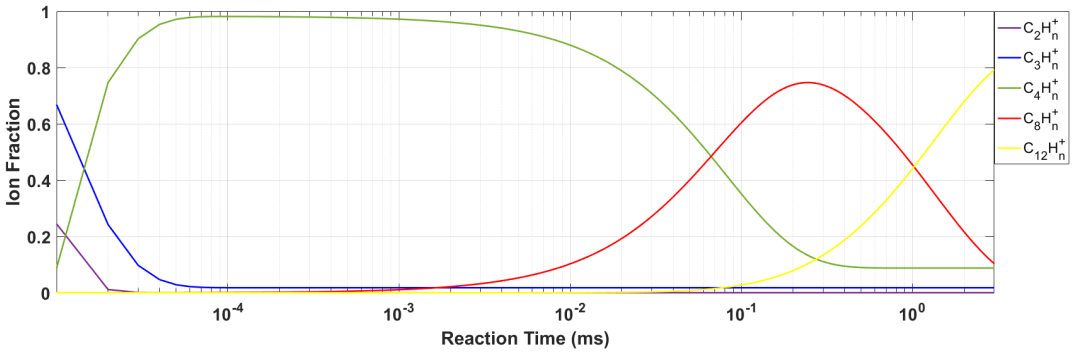

Figure 3.4: Fraction of the ions that can be formed as a function of the time in isobutane at a total pressure of 8 Torr.

In Figure 3.5, the reduced mobility of the ions produced in iso-C_4H_{10} as function of the reduced

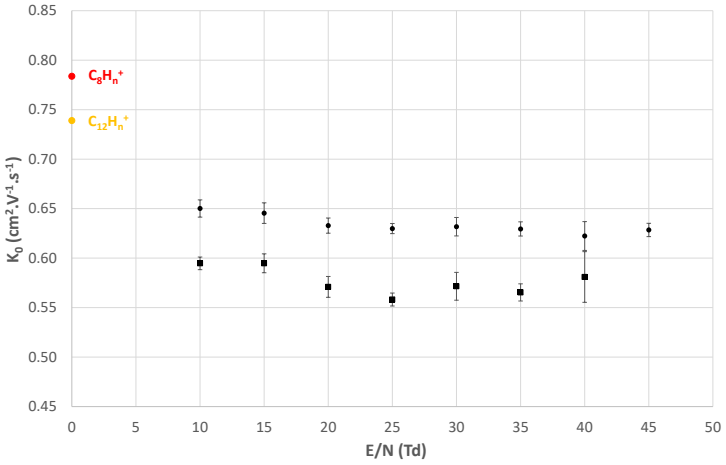

Figure 3.5: Reduced mobility of the ions produced in iso-C_4H_{10} as function of the reduced electric field for a pressure of 8 Torr at room temperature. The colored points represent the mobility values expected from the Langevin limit for $C_8H_n^+$ (red) and $C_{12}H_n^+$ (yellow) ions.

electric field for a pressure of 8 Torr at room temperature with the mobility values expected from the Langevin theory for the main candidate ions, $C_8H_n^+$ and $C_{12}H_n^+$, are presented. From figure 3.5, we find that the experimental mobilities obtained, for the lower E/N, have a deviation of about 20% from the ones expected from Langevin theory. This result is not surprising since the Langevin theory has some known limitations when used to predict the mobility of massive molecular ions [20]. From the analysis made both from the fraction of ions arriving at the collecting grid (in Figure 3.4) and from the Langevin limit comparison, we conclude that the ions responsible for the peaks should indeed be the $C_8H_n^+$ ions, for the peak presenting higher mobility, and the $C_{12}H_n^+$ ions, for the other one presenting lower mobility.

Comparing our results, for low reduced electric fields, with the ones found in literature, we find a small deviation of about less than 2% for the $C_{12}H_n^+$ ions, which are the ones that are expected to be found in higher pressure systems, albeit, in these works, the ions responsible for the peaks observed are either wrongly identified [67] or not identified at all [68].

The experimental results obtained did not change significantly in the pressure range studied, from 6 to 10 Torr and are presented in Table A.1, for a total pressure of 8 Torr, V_{GEM} of 25 V at room temperature.

.

Nitrogen (N_2)

In a previous work on pure nitrogen (N_2) [33], the mobility of N_4^+ in their parent gas (N_2) only one peak is observed at room temperature (293K), in the pressure range of 6 to 16 Torr, for reduced electric fields between 15 and 35 Td, and for a V_{GEM} of 20.5 eV. As in the previous work, using a V_{GEM} of 25 V, the same kind of ion responsible for peak is expected, since only the N_2^+ primary ion is possible to be produced. This ion will further react by colliding with N_2 molecules through a three-body reaction, which will result in the production of N_4^+ ions. A summary of the possible reactions and respective rate constants or cross section for electron impact ionization for 25 eV in pure N_2 is presented in Table 3.10.

For the purpose of this work, the mobilities of the N_4^+ ions in pure N_2 were taken from [33].

Table 3.10: Summary of possible reactions and respective rate constants or cross section for electron impact ionization at 25 eV in pure N_2 (references on the last column).

Reaction	Rate Constant	Cross Section (25 eV)	Ref.
$e^- + N_2 \rightarrow N_2^+ + 2e^-$	-	0.640×10^{-16} cm^2	[69]
$N_2^+ + 2N_2 \rightarrow N_4^+ + N_2$	$5.5 \pm 0.3 \times 10^{-29}$ cm^6.s^{-1}	-	[70]

3.2.2 Binary mixtures of argon (Ar) with various molecular gases

As already mentioned, argon (Ar) has been chosen as the main filling in many gaseous detectors. Thus, understanding its behavior in terms of ion transport properties when in mixtures of Ar with other molecular gases is critical in order to improve the performance of large gaseous detectors.

In this section results in binary mixtures of Ar–CH_4 and Ar–C_2H_6 will be briefly reviewed, while results in Ar–N_2 mixtures will be discussed and the results in mixtures of Ar–CF_4 and Ar–iso-C_4H_{10} will be presented and discussed.

Argon–Nitrogen (Ar–N_2)

In argon–nitrogen (Ar–N_2) mixtures, from pure N_2 to pure Ar, only one peak was observed in the entire range of mixtures studied for a total pressure of 8 Torr, reduced electric field of 15 Td, V_{GEM} of 25 V and room temperature (293K), as can be seen in Figure 3.6, which presents the time-of-arrival spectra (average of 128 pulses) recorded for several Ar-N_2 mixtures of 5%, 50%, 70% and 95% of Ar in the previously mentioned conditions. We also noticed that the mobility of the ions decreases slowly and the signal amplitude increases slightly with increasing Ar relative concentration.

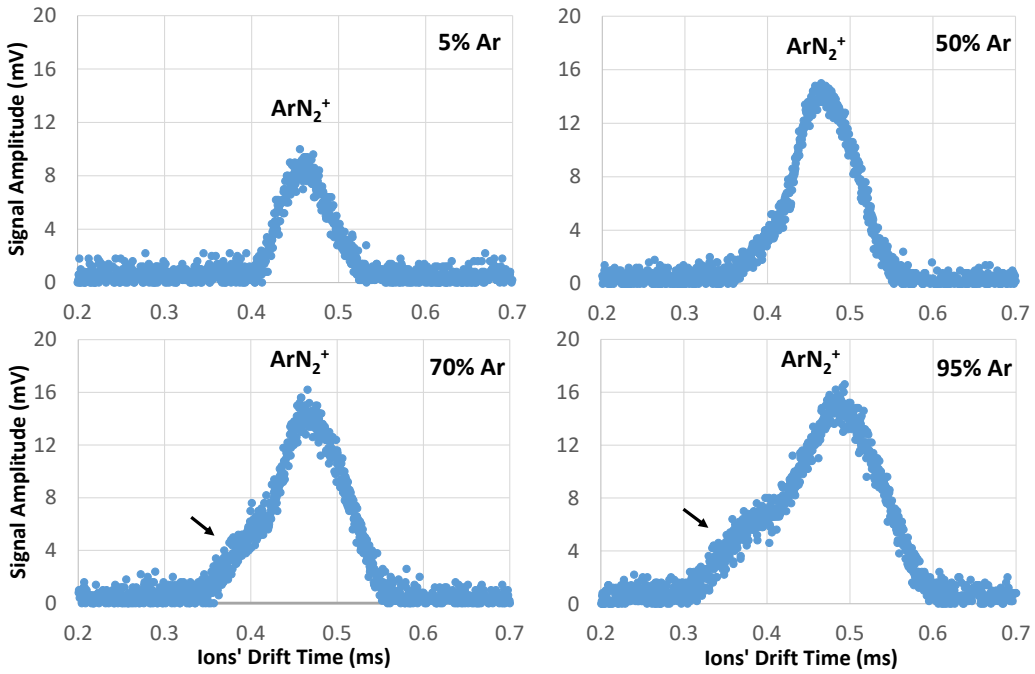

Figure 3.6: Time-of-arrival spectra (average of 128 pulse) recorded for several Ar-N_2 mixtures (5%, 50%, 70% and 95% of Ar) at total pressure of 8 Torr, reduced electric field of 15 Td, V_{GEM} of 25 V and room temperature (293K).

For the correct identification of the ion responsible for the peak, it was required to understand the relative abundance of primary ions produced which depends on V_{GEM} and on the relative abundance of

each gas. According to Monte Carlo simulations performed in our group for a V_{GEM} of 25 V, the relative abundance of primary ions produced in the GEM depends on the relative abundance of each gas. Ions of N_2^+ are predominately produced from pure N_2 up to approximately 35% of Ar, and so increasing Ar concentration above that value leads to the dominant production of Ar^+ ions.

When in their parent gases, as explained before, both ions react with the gas atoms/molecules through three-body reactions leading to formation of Ar_2^+ and N_4^+ ions. However, when in a mixture of both, the reactions taking place are much more complex, as can be seen in Table 3.11 where a summary of possible reactions between the primary ions with atoms/molecules of Ar and N_2 and their respective rate constants is presented.

Table 3.11: Summary of possible reactions and respective rate constants in Ar-N_2 mixtures (references on the last column).

Reaction	Rate Constant	Ref.
$N_4^+ + Ar \rightarrow ArN_2^+ + N_2$	1.4×10^{-12} cm^3.s^{-1}	[71]
$ArN_2^+ + N_2 \rightarrow Ar + N_4^+$	$\leq3\times10^{-13}$ cm^3.s^{-1}	[71]
$Ar_2^+ + N_2 \rightarrow ArN_2^+ + Ar$	$\gg2\times10^{-11}$ cm^3.s^{-1}	[71]
$ArN_2^+ + Ar \rightarrow Ar_2^+ + N_2$	$\gg1\times10^{-12}$ cm^3.s^{-1}	[71]
$Ar^+ + N_2 \rightarrow N_2^+ + Ar$	$1.10\pm0.22\times10^{-11}$ cm^3.s^{-1}	[60]
$N_2^+ + Ar \rightarrow Ar^+ + N_2$	$2.00\pm0.40\times10^{-13}$ cm^3.s^{-1}	[60]

Considering that the ionization energies of Ar and N_2 are very close to each other (15.76 eV [72] and 15.58 eV [73], respectively), it is understandable why the reactions involved, the charge transfer reactions and the ones leading to ArN_2^+ presented in Table 3.11, are reversible and also why their rate constants are not accurately known. Despite that, there is a clear tendency for the formation of ArN_2^+ ions and so it is expected that these will be the ions responsible for the peak observed.

Additionally, the appearance of a bump at the left side of the main peak for Ar concentrations above 70% might be due to a hetero-nuclear associative ionization of the molecule involving a highly excited state of the Ar atom and a N_2 molecule, which can be expressed by [71]:

$$Ar^* + N_2 \rightarrow ArN_2^+ + e^- \tag{3.1}$$

with a rate constant of $1.5\pm0.5\times10^{-11}$ cm^{3}s^{-1}, leading to the formation of the same ion product (ArN_2^+), but through a different channel. Since, from Monte Carlo simulations, it was concluded that about 10% of the Ar excited states produced in the GEM have enough energy to produce ArN_2^+, the ions resulting from this channel should in fact appear at the left side of the main peak, because the ones originated through the main channel (involving Ar_2^+) may have their mobility affected by their predecessor ions (Ar^+ and Ar_2^+) which present lower mobility. Thus both the bump and main peak are probably due to the same ions, ArN_2^+.

In Figure 3.7 is displayed the inverse of the reduced mobility of the ions produced in the Ar-N_2 mixture as function of Ar concentration for a pressure of 8 Torr and E/N of 15 Td at room temperature as well as the mobility values expected from the Blanc's law for the main candidate ions, N_4^+, ArN_2^+ and Ar_2^+, are

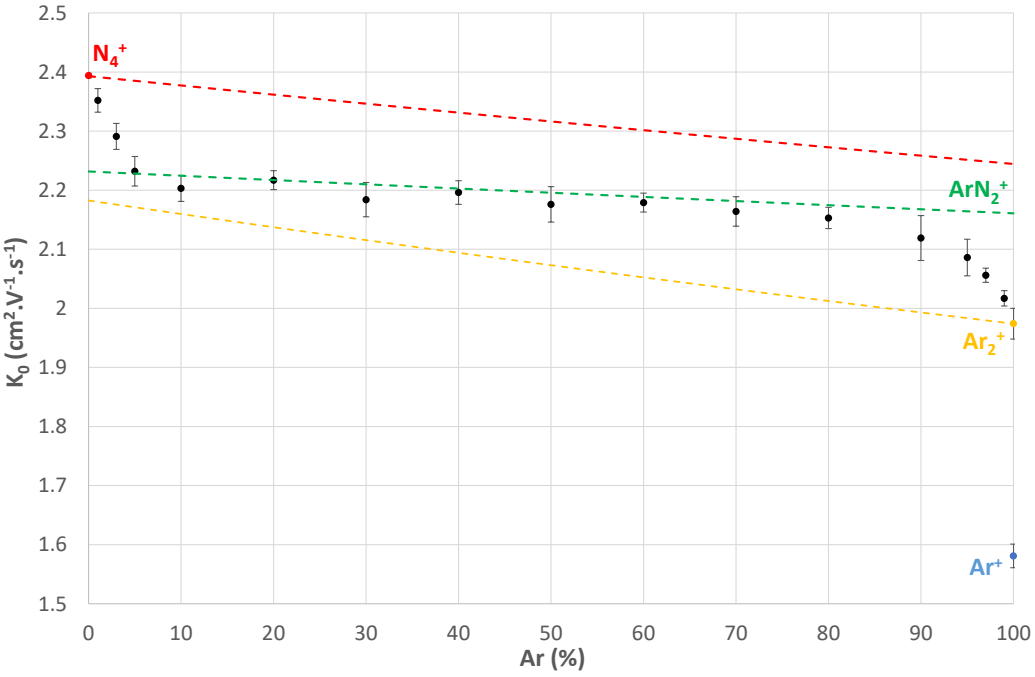

Figure 3.7: Inverse of the reduced mobility of the ions produced in the Ar-N_2 mixture as function of Ar relative concentration for a pressure of 8 Torr and E/N of 15 Td at room temperature. The dashed lines represent the mobility values expected from the Blanc's law for N_4^+ (red), ArN_2^+ (green) and Ar_2^+ (yellow).

displayed. If we now compare the experimental values obtained with the ones from Blanc's law for those ions, we find that the mobility experimentally measured follows closely, within a mean deviation of about 8%, the theoretical values obtained from Blanc's law for ArN_2^+ ions from 10% to 90% of Ar, deviating to N_4^+ and Ar_2^+ for high concentrations of N_2 and Ar, respectively.

Argon–Carbon-tetrafluoride (Ar–CF_4)

In argon–carbon-tetrafluoride (Ar–CF_4) mixtures, from pure CF_4 to pure Ar, only one peak, with a slight bump appearing at its left side, was consistently observed in the entire range of mixtures studied for a total pressure of 8 Torr, reduced electric field of 15 Td and 20 Td, V_{GEM} of 25 V at room temperature (293K). In Figure 3.8, the time-of-arrival spectra (average of 128 pulse) recorded for several Ar-CF_4 mixtures of 20%, 50%, 70% and 90% of Ar at a total pressure of 8 Torr, reduced electric field of 15 Td, V_{GEM} of 25 V and at room temperature (293K) is presented. Looking at the same peak, it is possible to see that the signal amplitude rises until about 90% of and that ions move faster with increasing Ar concentration. In addition, a slight asymmetry is possible to be observed from 20% up to 50% Ar, over which point a bump starts to appear, becoming even more noticeable up to 90%.

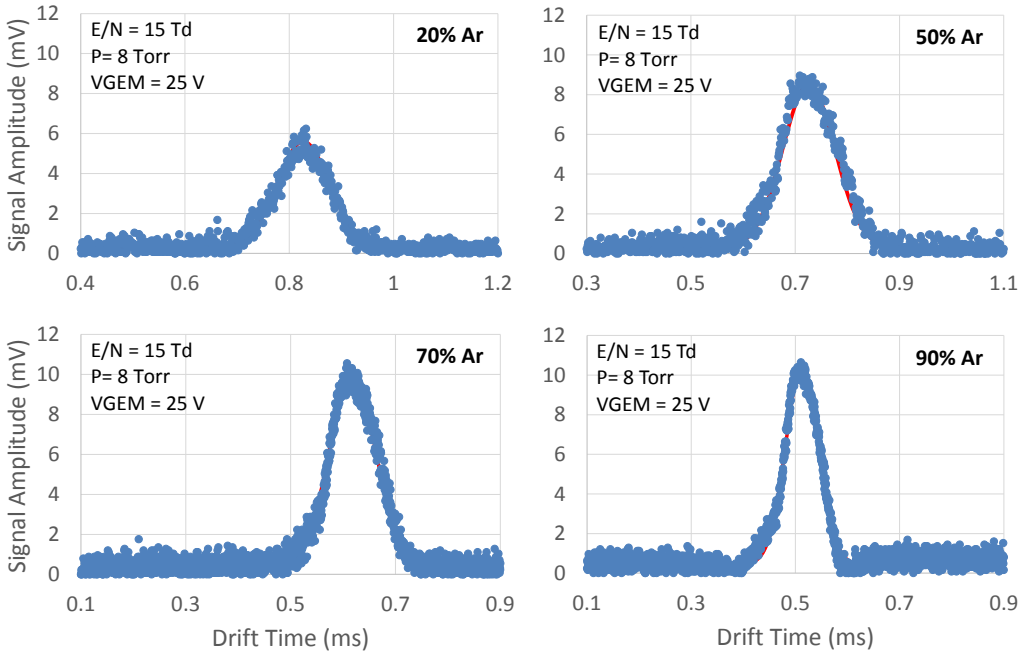

Figure 3.8: Time-of-arrival spectra (average of 128 pulse) recorded for several Ar-CF_4 mixtures (20%, 50%, 70% and 90% of Ar) at total pressure of 8 Torr, reduced electric field of 15 Td, V_{GEM} of 25 V and room temperature (293K).

For electron energies up to 25 eV, two types of primary ions will be produced, Ar^+ and CF_3^+ (following Tables 3.1 and 3.2). Due to the electron impact ionization cross-sections, Ar^+ ions will be predominantly produced from pure Ar down to 45% Ar. However, these primary ions quickly undergo a charge transfer reaction with CF_4, described by:

$$Ar^+ + CF_4 \rightarrow CF_3^+ + F + Ar. \tag{3.2}$$

with a rate constant of 0.70$\times$ 10^{-9} $cm^3.s^{-1}$ [74]. This should lead to a peak corresponding to the same ion as in pure CF_4, *i.e.*, the CF_3^+ ion. This mechanism will also be responsible for preventing the formation of Ar_2^+ ions described in Table 3.1, also explaining why the signal amplitude rises until about 90$\%$ Ar. To verify these assumptions, the ion fraction of the possible ions formed in a gas mixture containing 95$\%$ Ar for a total pressure of 8 Torr was determined. The results are presented in Figure 3.9.

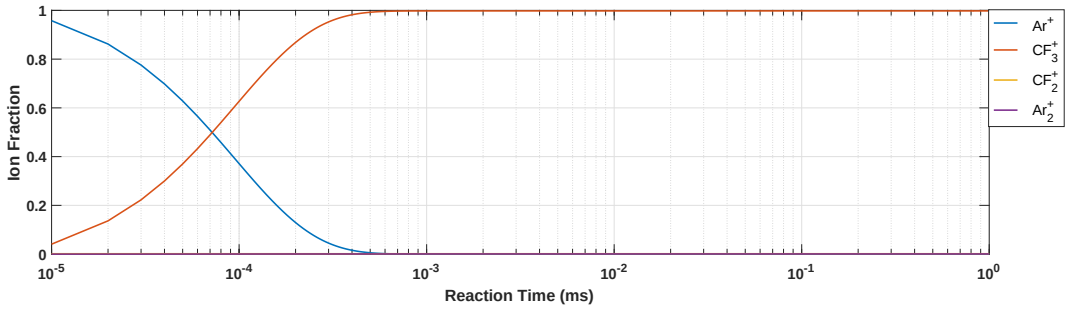

Figure 3.9: Fraction of the ions that can be formed as a function of the time in Ar-CF_4 mixtures with 95$\%$ of Ar at a total pressure of 8 Torr.

In Figure 3.10, the inverse of the reduced mobility of the ions produced in the Ar-CF_4 mixture as function of Ar relative concentration for a pressure of 8 Torr and E/N of 15 Td at room temperature, as well as the mobility values expected from the Blanc's law for CF_3^+ and Ar_2^+ are presented. By comparing the behavior of the inverse of the reduced mobility of the ions with the predicted one for the main candidate ions, we can see that the behavior of the experimental data is well described within 5$\%$ deviation from the ones predicted by Blanc's law and Langevin limit for CF_3^+ ions.

The bump was considered to be related to impurities, namely water resulting from the detector outgassing, since the fraction of other possible ions, Ar_2^+ and CF_2^+, is negligible and that the effect seems to be independent of the gas composition.

Finally, it is important to notice that, as in pure CF_4, increasing the pressure could lead to the formation of $CF_3^+(CF_4)$ clusters, with the mobility of the ions becoming about 11$\%$ lower than our observations. The experimental results obtained did not change significantly neither in the pressure range studied, from 6 to 10 Torr, or in the reduced electric field range studied, for 15 and 20 Td. The experimental results obtained can be found in Table A.2.

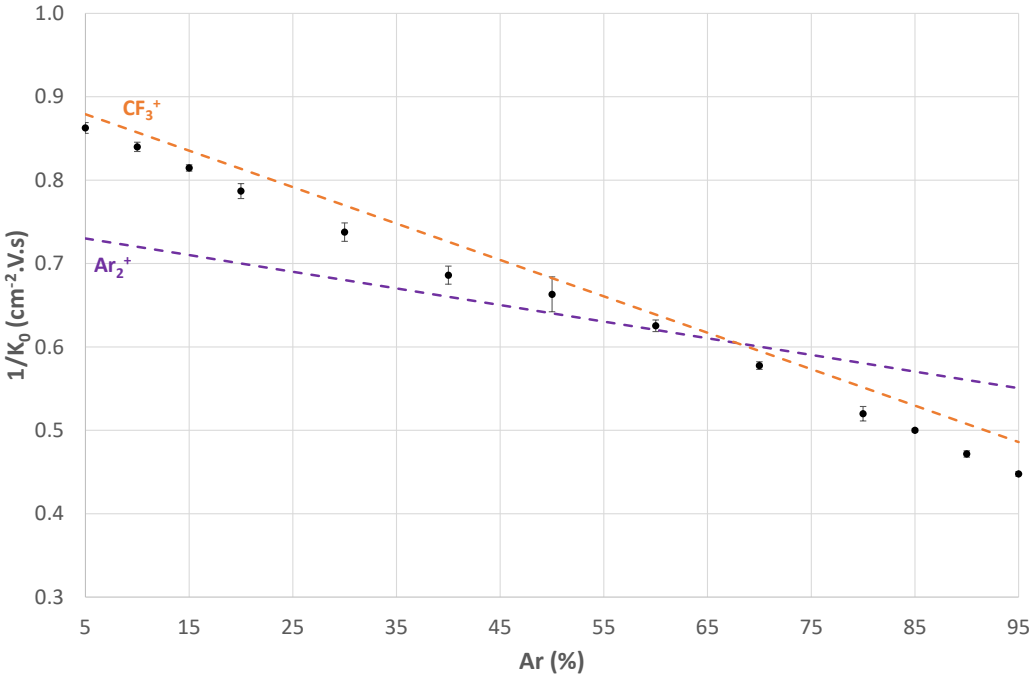

Figure 3.10: Inverse of the reduced mobility of the ions produced in the Ar-CF_4 mixture as function of Ar relative concentration for a pressure of 8 Torr and E/N of 15 Td at room temperature. The dashed lines represent the mobility values expected from the Blanc's law for CF_3^+ (orange) and Ar_2^+ (purple).

Argon–Isobutane (Ar–iso-C_4H_{10})

In argon–isobutane (Ar–iso-C_4H_{10}) mixtures, from pure iso-C_4H_{10} to pure Ar, the number and origin of the peaks observed changes throughout the range of mixtures studied for a total pressure of 8 Torr, V_{GEM} of 25V and E/N of 15 Td and 20 Td at room temperature. In Figure 3.11, the time-of-arrival spectra (average of 128 pulse) recorded for several Ar–iso-C_4H_{10} mixtures of 5%, 80%, 85% and 95% of Ar for a total pressure of 8 Torr, reduced electric field of 15 Td and V_{GEM} of 25 V at room temperature (293K) are presented. From this figure, we can see that increasing the relative concentration of argon results in greater signal amplitude, due to the cross sections involved, and in faster ions, because of the lower polarizability and mass of argon atoms.

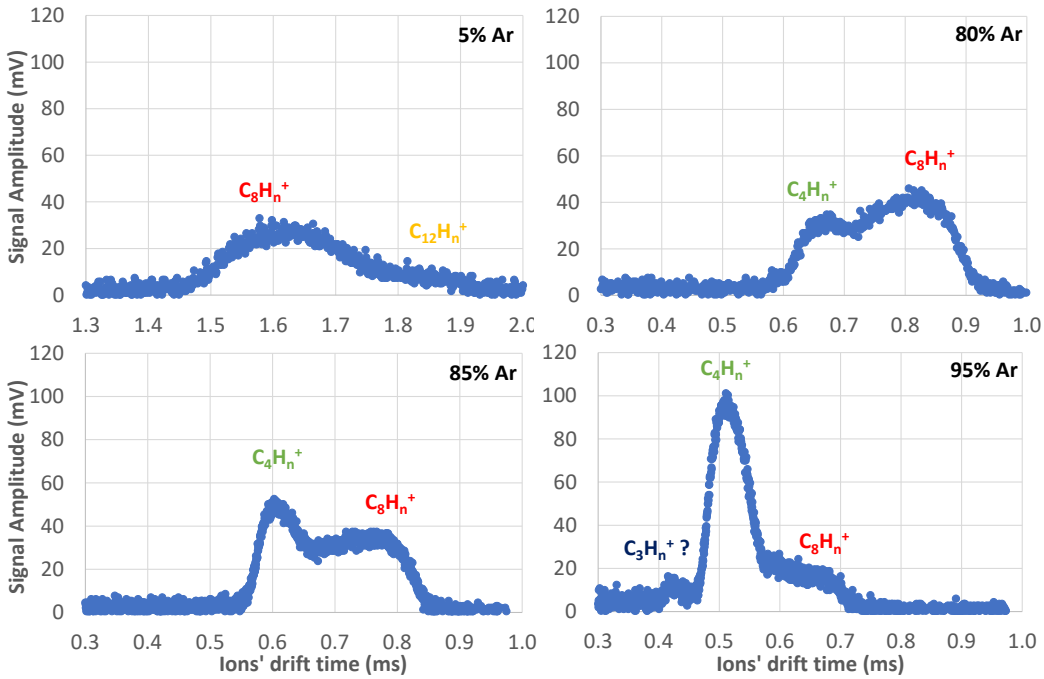

Figure 3.11: Time-of-arrival spectra (average of 128 pulse) recorded for several Ar–iso-C_4H_{10} mixtures (5%, 80%, 85% and 95% of Ar) at total pressure of 8 Torr, reduced electric field of 15 Td, V_{GEM} of 25 V and room temperature (293K).

In order to correctly identify the ions responsible for the peaks, we tried first to understand which primary ions are produced at the GEM and then which reactions between the primary and secondary ions and the atoms/molecules occur during the drift time.

For electron energies of 25 eV, four types of primary ions will be produced: Ar^+ ions, and 2-carbon ($C_2H_n^+$), 3-carbon ($C_3H_n^+$) and 4-carbon ($C_4H_n^+$) ion groups, with the carbon ion groups being predominantly produced from pure isobutane up to about 82% Ar due to the higher total electron impact ionization of the isobutane molecules, as can be seen by comparing Tables 3.1 and 3.7. Yet, Ar^+ ions should transfer their charge to the isobutane molecules, since the Ar atoms ionization energy (15.82 eV [72]) is much

higher than that of iso-C_4H_{10} molecules (10.74 eV [75]) and although the rate constant for this process could not be found in literature, it was assumed they have the same rate constant as charge transfer reactions from Ar^+ ions to butane molecules, which is 1.4 $\times$ 10^{-9} cm^3s^{-1} [64]. The ionization products and product distribution for reactions between the Ar ions and molecules of isobutane are summarized in Table 3.12. Thus, we can expect that the ions arriving to the collecting grid to be isobutane ions, although not exactly the same ones as in pure isobutane since the presence of argon should delay the formation of more complex and heavier ions.

Table 3.12: Ionization products, product distribution and rate constants for reactions between the Ar ions and molecules of butane [64].

Reaction	Prod. Dist.
$Ar^+ + C_4H_{10} \rightarrow C_2H_3^+ + (2C, 7H) + Ar$	0.27
$Ar^+ + C_4H_{10} \rightarrow C_2H_4^+ + (2C, 6H) + Ar$	0.08
$Ar^+ + C_4H_{10} \rightarrow C_2H_5^+ + (2C, 5H) + Ar$	0.32
$Ar^+ + C_4H_{10} \rightarrow C_3H_5^+ + (C, 5H) + Ar$	0.26
$Ar^+ + C_4H_{10} \rightarrow C_3H_7^+ + (C, 3H) + Ar$	0.05
$Ar^+ + C_4H_{10} \rightarrow C_4H_9^+ + H + Ar + Ar$	0.02

By using the rate constants to calculate the fraction of ions that can be originated as a function of time, we can predict the fraction of ions arriving at the collecting grid which will help in the ion identification. Figure 3.12 displays the fraction of the ions formed as a function of time in Ar–iso-C_4H_{10} mixtures with 5$\%$ and 95$\%$ Ar at a total pressure of 8 Torr. From the 5$\%$ Ar calculation, in Figure 3.12(a), we can see that for about 1.6 ms (corresponding to the drift time of the main peak in the corresponding spectra), the ions arriving on the grid should be of $C_8H_n^+$ and $C_{12}H_n^+$ groups. On the other hand, for 95$\%$ Ar, in Figure 3.12(b), for about 0.5 ms, it is possible to see that the ions arriving at the grid should be predominantly of $C_4H_n^+$, and also some of $C_8H_n^+$.

Then, by calculating the expected values for the mobility of the candidate ions through Blanc's law and the Langevin limit and comparing it with the experimental values obtained we can identify the ions responsible for the peaks retrieved. In Figure 3.13, the inverse of the reduced mobility of the ions produced in the Ar–iso-C_4H_{10} mixture as function of Ar relative concentrations for a pressure of 8 Torr and E/N of 15 Td at room temperature is represented. The dashed lines represent the mobility values expected from the Blanc's law for $C_{12}H_n^+$, $C_8H_n^+$ and $C_4H_n^+$ ions. As can be seen in the same figure, the behavior of the final ions observed is well described by Blanc's law and Langevin theory.

Finally, we can identify the ions present by mixing the information gathered from the time-of-arrival spectra (Figure 3.11), the calculation of ion fraction, the predicted values and the experimental values obtained. From pure isobutane up to 20 $\%$ Ar, two peaks are observed which should have the same origin as in pure isobutane: $C_{12}H_n^+$ for the peak with lower mobility and $C_8H_n^+$ for the peak with higher mobility, because the relative concentrations of argon are low. However, as we increase the Ar concentration over this point, up to 70$\%$ of Ar, only one peak is observed, attributed to $C_8H_n^+$ ions as the reactions leading to $C_{12}H_n^+$ ions do not have time to be completed during the ions' drift time. This effect will be

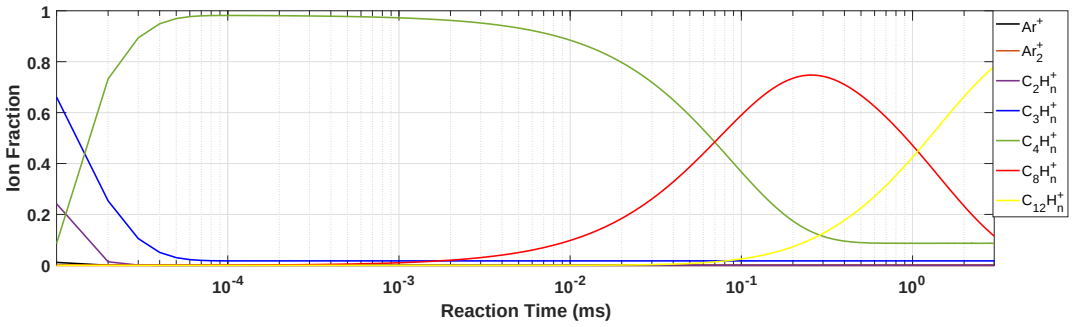

(a)

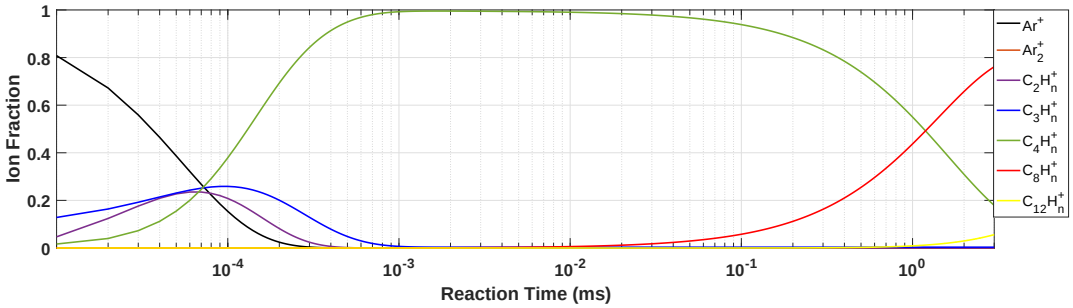

(b)

Figure 3.12: Fraction of the ions that can be formed as a function of the time in Ar–iso-C_4H_{10} mixtures for 5% (a) and 95% (b) of Ar at a total pressure of 8 Torr.

responsible for the appearance of a peak of even higher mobility (smaller drift time) that should be due to $C_4H_n^+$ ions for concentrations above 80 % of Ar. This behavior depends on the reduced electric field being more pronounced for higher values of E/N, because of the smaller drift times. Also a third peak with higher mobility starts to appear for 95%, that could be due to $C_3H_n^+$ ions. However its mobility could not be retrieved, since the peak is too small to be fitted with accuracy.

The experimental results obtained did not change significantly in the pressure range studied, from 6 to 10 Torr and can be found for in Table A.3 for E/N of 15 Td and 20 Td, V_{GEM} of 25 V and pressure of 8 Torr, at room temperature (293 K).

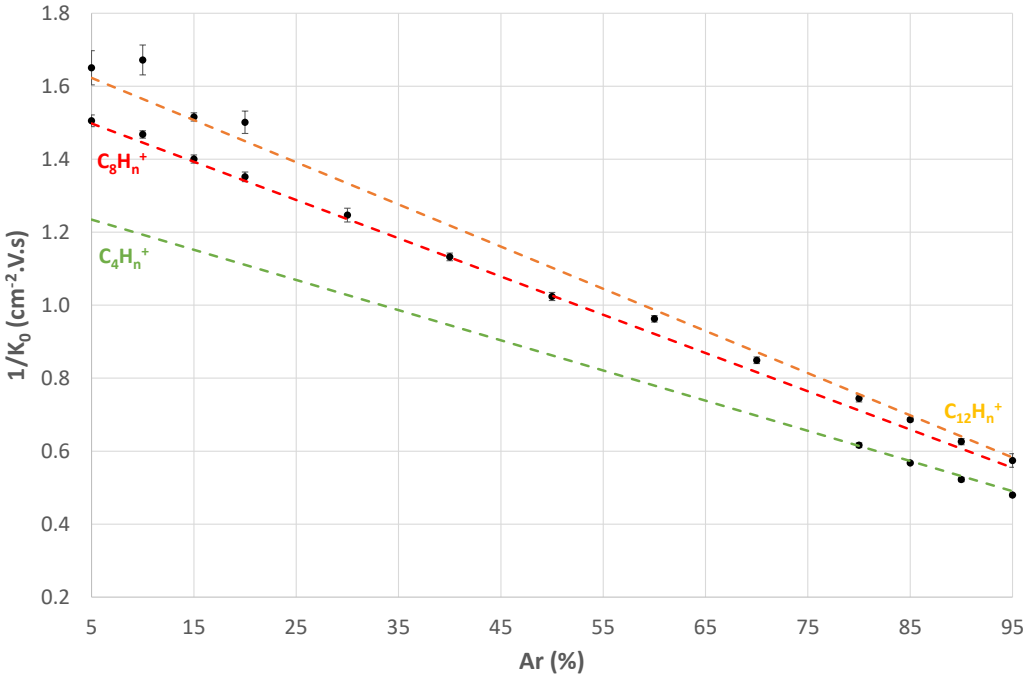

Figure 3.13: Inverse of the reduced mobility of the ions produced in the Ar-iso-C_4H_{10} mixture as function of Ar relative concentration for a pressure of 8 Torr and E/N of 15 Td at room temperature. The dashed lines represent the mobility values expected from the Blanc's law for $C_{12}H_n^+$ (yellow), $C_8H_n^+$ (red) and $C_4H_n^+$ (green).

Argon–Methane (Ar–CH_4)

In a previous work with argon–methane (Ar–CH_4) mixtures [38], three peaks were observed. Increasing the concentration from pure methane up to 90% of Ar results in slower ions drifting in the gas, whose mobility seems to stabilize after that point.

For a V_{GEM} of 25 V, the primary ions formed will be predominately produced from CH_4 molecules, from pure CH_4 up to 70% of Ar. However, as can be seen in Table 3.13, where the ionization products, product distribution and rate constants for the collisions of CH_4 molecules with the primary ions of Ar are presented, the ions arriving at the collecting grid in this case should be the same ones as in pure CH_4, although with a different distribution. In fact, the presence of Ar leads to the separation of the peaks due to $C_2H_n^+$ and $C_3H_n^+$ ions, and as a consequence three peaks can be observed, due to CH_5^+ (higher mobility), $C_2H_n^+$ (intermediate mobility) and $C_3H_n^+$ (lower mobility) ions.

Finally, the results did not display considerable differences either on the pressure range (5-8 Torr) or in the reduced electric field range (17-43 Td) studied, and were well described by Blanc's law and Langevin theory.

Table 3.13: Ionization products, product distribution and rate constants for the collisions of CH_4 molecules with the primary ions of Ar [60]. Authors of [76] believe that the CH_4^+ ions are not observed due to possible fragmentation.

Reaction	Prod. Dist.	Rate Const. (10^{-9} cm^3s^{-1})
$CH_4 + Ar^+ \rightarrow CH_4^+ + Ar$	Not observed	0.98±0.01
$CH_4 + Ar^+ \rightarrow CH_3^+ + H + Ar$	0.85	0.98±0.01
$CH_4 + Ar^+ \rightarrow CH_2^+ + H_2 + Ar$	0.15	0.98±0.01

Argon–Ethane (Ar–C_2H_6)

In a previous work with argon–ethane (Ar–C_2H_6) mixtures [35], a similar behavior to the Ar-CF_4 was observed. Increasing the concentration from pure ethane up to 90% of Ar, results in faster ions and higher signal amplitude.

As in mixtures of Ar-CH_4, the ions observed in this case are the same as in pure C_2H_6 ions, since the presence of Ar leads to the formation of the same primary ions as in pure C_2H_6, $C_3H_n^+$ and $C_4H_n^+$ ions, but with a different distribution, as can be seen in Table 3.14, where the ionization products, product distribution and rate constants for the collisions C_2H_6 molecules with the primary ions of Ar are presented.

For concentrations of Ar above 80%, a bump starts to appear at the right of the $C_4H_n^+$, that could be due to the $C_5H_{11}^+$ ions, produced by [77]:

$$C_3H_5^+ + C_2H_6 \rightarrow C_5H_{11}^+ \tag{3.3}$$

As explained in [35], $C_3H_5^+$ is one of the possible products of the reaction between $C_2H_3^+$ ions and

C_2H_6 molecules, and its concentration increases with increasing Ar concentrations, however the rate constant for this reaction could not be found in the literature.

Nevertheless, the behavior of the ion mobility is well described by Blanc's law and Langevin theory until about 80% of Ar for the final ions drifting in the gas, $C_3H_n^+$ and $C_4H_n^+$.

Table 3.14: Ionization products, product distribution and rate constants for the collisions C_2H_6 molecules with the primary ions of Ar [60]. Authors of [76] believe that the $C_2H_6^+$ ions are not observed due to possible fragmentation.

Reaction	Prod. Dist.	Rate Const. (10^{-9} cm^3s^{-1})
$C_2H_6 + Ar^+ \rightarrow C_2H_6^+ + Ar$	Not observed	1.15±0.17
$C_2H_6 + Ar^+ \rightarrow C_2H_5^+ + H + Ar$	0.08	1.15±0.17
$C_2H_6 + Ar^+ \rightarrow C_2H_4^+ + H_2 + Ar$	0.22	1.15±0.17
$C_2H_6 + Ar^+ \rightarrow C_2H_3^+ + H_2 + H + Ar$	0.42	1.15±0.17
$C_2H_6 + Ar^+ \rightarrow C_2H_2^+ + 2H_2 + Ar$	0.23	1.15±0.17
$C_2H_6 + Ar^+ \rightarrow CH_3^+ + CH_3 + Ar$	0.05	1.15±0.17

3.2.3 Binary mixtures of CF_4 with alkanes

As previously explained, carbon-tetrafluoride (CF_4) has been considered as one of the molecular additives for the LCTPC mixture [14] because of its desirable characteristics. As a third component is expected to be added methane (CH_4), ethane (C_2H_6) or isobutane (iso-C_4H_{10})), it is important to understand the behavior in mixtures of these gases in terms of ion transport properties.

In this section, results in mixtures of CF_4–CH_4, CF_4–C_2H_6, CF_4–iso-C_4H_{10} will be presented and discussed in order to understand the behavior in terms of ion mobility for the alternative mixtures to be chosen for the LCTPC.

Carbon-tetrafluoride–Methane (CF_4-CH_4)

The mobility of the ions in tetrafluoride-methane (CF_4-CH_4) mixtures was measured for E/N of 15 and 20 Td, for different total pressures (6-10 Torr) and for a constant V_{GEM} of 25 V at room temperature (293K).

Figure 3.14 displays the time-of-arrival spectra (average of 128 pulse) recorded for several CF_4-CH_4 mixtures of 5%, 40% and 95% of CF_4 at total pressure of 8 Torr, reduced electric field of 20 Td, V_{GEM} of 25 V and at room temperature. As can be seen in the same figure, the number of peaks observed depends on the relative abundance of each gas. Also, increasing CF_4 concentration leads both to slower ions because of the CF_4 higher mass and polarizability, and to smaller signal amplitude due to the lower ionization electron impact ionization cross-section of CF_4 molecules.

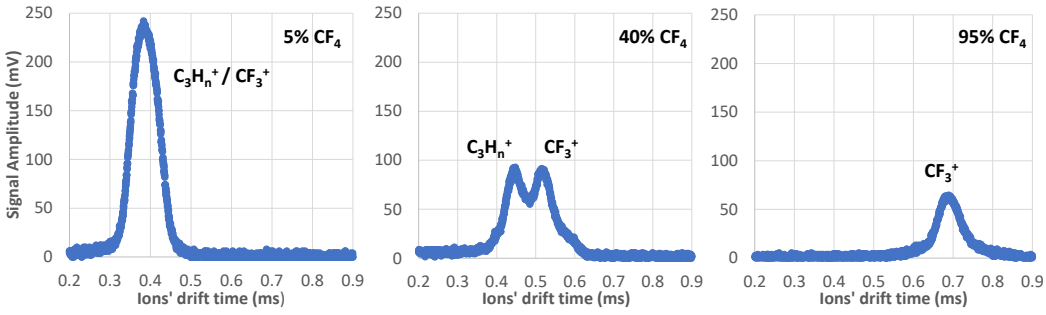

Figure 3.14: Time-of-arrival spectra (average of 128 pulse) recorded for several CF_4-CH_4 mixtures (5%, 40% and 95% of CF_4) at total pressure of 8 Torr, reduced electric field of 20 Td, V_{GEM} of 25 V and room temperature (293K).

The primary ions formed are: CF_3^+, which is predominantly produced from pure CF_4 down to about 70% of CF_4, and the CH_4^+, CH_3^+ and CH_2^+ ions, as can be seen by the cross sections for electron impact in the Tables 3.2 and 3.3.

In Table 3.15, the ionization products, product distribution and rate constants for the collisions of the primary ions of CH_4 with the CF_4 and CH_4 molecules are summarized. By analyzing this table, it is possible to conclude that the CH_5^+ ions, produced from reactions between CH_3^+ ions with CH_4

molecules, react with CF_4 molecules, producing CF_3^+ ions, while CH_2^+ ions react with CH_4 molecules, producing $C_2H_n^+$ ions (n=2,3,4,5) and later $C_3H_n^+$ ions. Finally, CH_3^+ ions can either react with CH_4 molecules, eventually producing 3-carbon ions, or with CF_4 molecules, producing CF_3^+ ions.

Table 3.15: Ionization products, product distribution and rate constants for the collisions of the primary ions of CH_4 with the CF_4 [78] and CH_4 [60] molecules.

Reaction	Prod. Dist.	Rate Const. (10^{-9} cm^3s^{-1})
$CH_4 + CH_4^+ \rightarrow CH_5^+ + CH_3$	1.00	1.15±0.05
$CH_4 + CH_3^+ \rightarrow C_2H_5^+ + H_2$	1.00	0.96±0.05
$CH_4 + CH_2^+ \rightarrow C_2H_2^+ + 2H_2$	0.12	1.20±0.05
$CH_4 + CH_2^+ \rightarrow C_2H_3^+ + 2H_2 + H$	0.22	1.20±0.05
$CH_4 + CH_2^+ \rightarrow C_2H_4^+ + H_2$	0.42	1.20±0.05
$CH_4 + CH_2^+ \rightarrow C_2H_5^+ + H$	0.038	1.20±0.05
$CH_4 + C_2H_5^+ \rightarrow C_3H_7^+ + H_2$	1.00	0.000011±0.000001
$CH_4 + C_2H_3^+ \rightarrow C_3H_5^+ + H_2$	1.00	0.22±0.01
$CH_4 + C_2H_2^+ \rightarrow C_3H_4^+ + H_2$	0.21	0.84±0.01
$CH_4 + C_2H_2^+ \rightarrow C_3H_5^+ + H$	0.79	0.84±0.01
$CF_4 + CH_3^+ \rightarrow CF_3^+ + CH_3F$	1.00	0.545±0.027
$CF_4 + CH_5^+ \rightarrow CF_3^+ + CH_4 + HF$	1.00	0.23±0.012

Using the cross sections for electron impact and the rate constants and product distributions for the collisions of ions with the gas molecules, calculations of the fraction of the ions that can be formed as a function of the time in CF_4-CH_4 mixtures for 5% and 95% of Ar at a total pressure of 8 Torr were performed. The results are presented in Figure 3.15.

In order to verify the identity of the ions, we compare the inverse of the reduced mobility of the ions produced in the CF_4-CH_4 mixture as function of CF_4 relative concentration for a pressure of 8 Torr and E/N of 20 Td at room temperature with the values the mobility values expected from the Blanc's law for the main candidate ions: CF_3^+ and $C_3H_n^+$, which is presented in Figure 3.16, and the origin of the peaks can be validated as the experimental values clearly follow the theoretical values predicted by Blanc's law with the Langevin limit for both CF_3^+ and $C_3H_n^+$ trend lines.

From pure methane up to 25% of CF_4, only one peak was observed being due to two different ions CF_3^+ and $C_3H_n^+$ (see results of simulation on ion fraction for 5% CF_4 in Figure 3.15(a), which are not possible to sort out because of their similar mobility, as can be seen in Figure 3.16 by the predicted mobilities from Blanc's law. Increasing CF_4 concentration above that point, leads to the the separation of the two ion groups which become distinguishable, until 95% CF_4, above which point only one peak was observed, which was identified as CF_3^+, assumption which is supported by the calculations on the ion fraction for 95% of CF_4 (displayed in Figure 3.15(b)).

Finally, no significant variation of the mobility was observed in the total pressure and E/N ranges studied. The results obtained are summarized in Table A.4 for E/N of 15 Td and of 20 Td, V_{GEM} of 25 V and pressure of 8 Torr at room temperature (293 K).

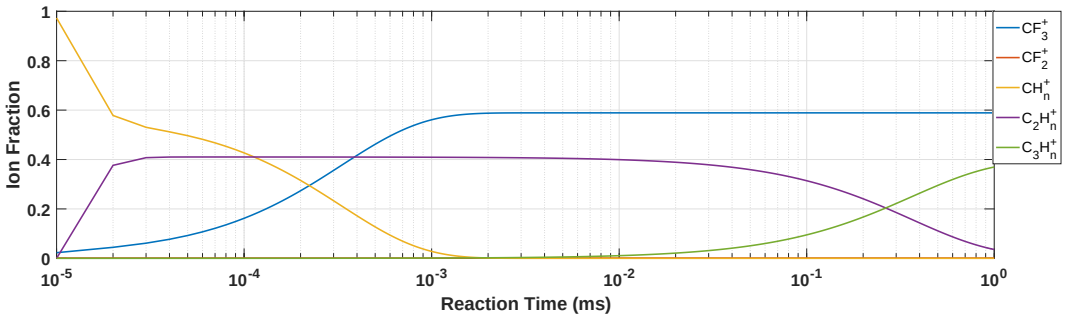

(a)

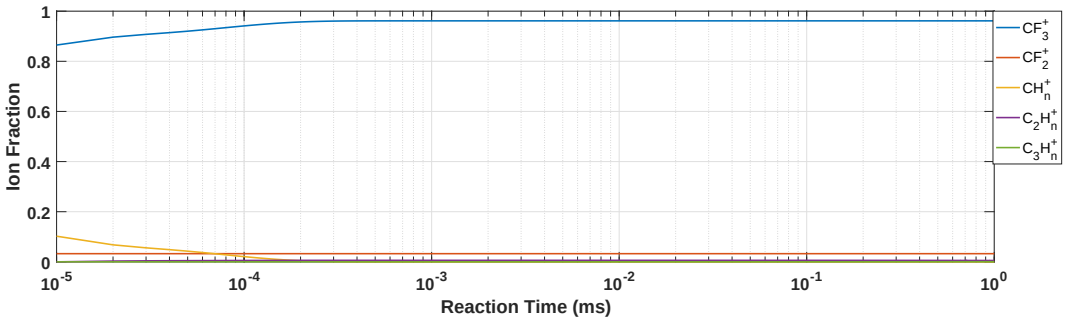

(b)

Figure 3.15: Fraction of the ions that can be formed as a function of the time in CF_4-CH_4 mixtures for 5% (a) and 95% (b) of Ar at a total pressure of 8 Torr.

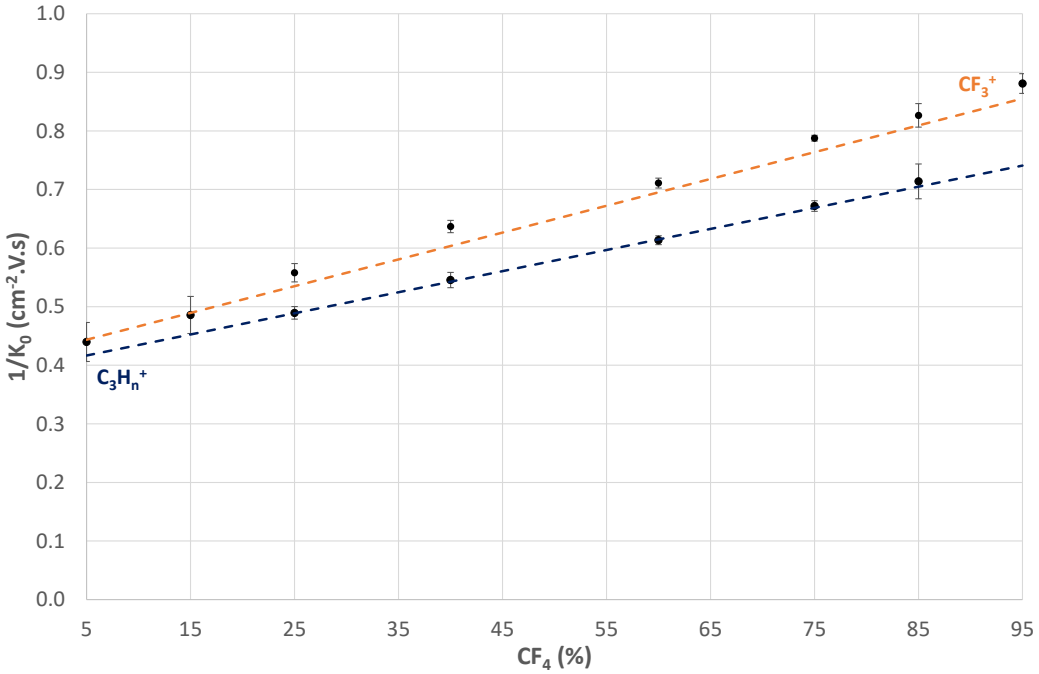

Figure 3.16: Inverse of the reduced mobility of the ions produced in the CF_4-CH_4 mixture as function of CF_4 relative concentration for a pressure of 8 Torr and E/N of 20 Td at room temperature. The dashed lines represent the mobility values expected from the Blanc's law for CF_3^+ (orange) and $C_3H_n^+$ (blue).

Carbon-tetrafluoride–Ethane (CF_4–C_2H_6)

The mobility of the ions in carbon tetrafluoride-ethane (CF_4–C_2H_6) mixtures was measured for E/N of 15 and 20 Td, for different total pressures (6-10 Torr) and for a constant V_{GEM} of 25 V at room temperature (293K).

Figure 3.17 displays the time-of-arrival spectra (average of 128 pulse) recorded for several CF_4–C_2H_6 mixtures of 5%, 60% and 95% of CF_4 at total pressure of 8 Torr, reduced electric field of 20 Td, V_{GEM} of 25 V and room temperature. As can be seen in the same figure, the number of peaks observed depends on the relative abundance of each gas. Also, increasing CF_4 concentrations, leads to ions moving slower, because of the higher mass of CF_4, and to a signal amplitude decrease due to the differences in the electron impact ionization cross-sections between CF_4 and C_2H_6.

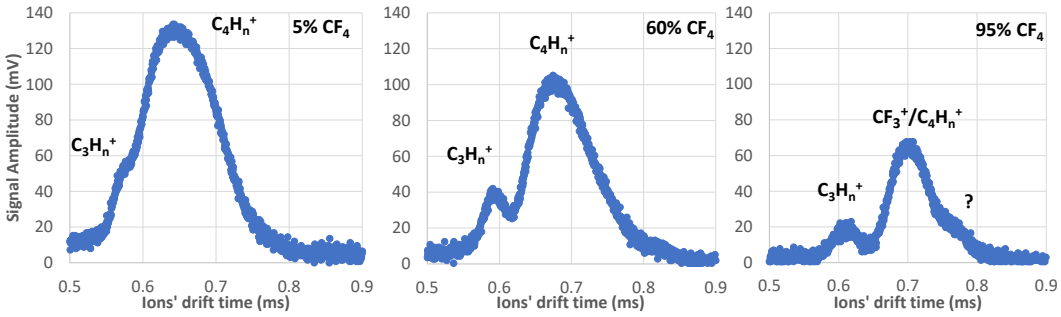

Figure 3.17: Time-of-arrival spectra (average of 128 pulse) recorded for several CF_4-C_2H_6 mixtures (5%, 60% and 95% of CF_4) at total pressure of 8 Torr, reduced electric field of 20 Td, V_{GEM} of 25 V and room temperature (293K).

For a V_{GEM} of 25 V, the primary ions originated at the GEM are CF_3^+, which are predominantly produced from pure CF_4 down to 75% of CF_4, and the $C_2H_6^+$, $C_2H_5^+$, $C_2H_4^+$, $C_2H_3^+$, $C_2H_2^+$ and CH_3^+ ions, as can be seen by the cross sections for electron impact in the Tables 3.2 and 3.5 presented in Section 3.2.1.

In Table 3.16, the ionization products, product distribution and rate constants for the collisions between C_2H_6 molecules and the primary ions of C_2H_6 [60] and of CF_4 [78] are summarized. As can be seen in the same table, CF_3^+ ions tend naturally to transfer their charge to C_2H_6 molecules, forming $C_2H_6^+$ and $C_2H_5^+$, which are already some of the primary species produced in C_2H_6. These 2-carbon ions ($C_2H_n^+$) will further react with C_2H_6 molecules producing both 3-carbon ($C_3H_n^+$) and 4-carbon ($C_4H_n^+$) ion groups, as seen in pure C_2H_6.

Using the cross sections for electron impact and the rate constants for the collision of ions with gas molecules, calculations on the fraction of the ions that can be produced as a function of time in CF_4–C_2H_6 mixtures for 5% and 95% of CF_4 at a total pressure of 8 Torr were performed. The results are presented in Figure 3.18. From them, it is clear that, with increasing CF_4 concentration, the $C_4H_n^+$ fraction gets higher and the $C_3H_n^+$ fraction gets lower.

Table 3.16: Ionization products, product distribution and rate constants for the collisions between $C_2H_6^+$ molecules and the primary ions of C_2H_6 [60] and of CF_4 [78].

Reaction	Prod. Dist.	Rate Const. (10^{-9} cm^{3}s^{-1})
$C_2H_6 + C_2H_6^+ \rightarrow C_3H_8^+ + CH_4$	0.42	0.019±0.001
$C_2H_6 + C_2H_6^+ \rightarrow C_3H_9^+ + CH_3$	0.58	0.019±0.001
$C_2H_6 + C_2H_5^+ \rightarrow C_4H_9^+ + H_2$	1.00	0.040±0.003
$C_2H_6 + C_2H_4^+ \rightarrow C_3H_6^+ + CH_4$	0.07	0.0053±0.0001
$C_2H_6 + C_2H_4^+ \rightarrow C_3H_7^+ + CH_3$	0.93	0.0053±0.0001
$C_2H_6 + C_2H_3^+ \rightarrow C_2H_5^+ + C_2H_4$	0.47	0.62±0.03
$C_2H_6 + C_2H_3^+ \rightarrow C_3H_5^+ + CH_4$	0.40	0.62±0.03
$C_2H_6 + C_2H_3^+ \rightarrow C_4H_7^+ + H_2$	0.13	0.62±0.03
$C_2H_6 + C_2H_2^+ \rightarrow C_2H_4^+ + C_2H_4$	0.18	1.46±0.06
$C_2H_6 + C_2H_2^+ \rightarrow C_2H_5^+ + C_2H_3$	0.09	1.46±0.06
$C_2H_6 + C_2H_2^+ \rightarrow C_3H_3^+ + CH_3 + H_2$	0.06	1.46±0.06
$C_2H_6 + C_2H_2^+ \rightarrow C_3H_5^+ + CH_3$	0.54	1.46±0.06
$C_2H_6 + C_2H_2^+ \rightarrow C_4H_5^+ + H_2 + H$	0.05	1.46±0.06
$C_2H_6 + C_2H_2^+ \rightarrow C_4H_7^+ + H$	0.09	1.46±0.06
$C_2H_6 + CF_3^+ \rightarrow C_2H_5^+ + CF_3H$	1.00	0.330±0.033
$C_2H_6 + CF_3^+ \rightarrow C_2H_6^+ + CF_3$	1.00	0.030±0.003

In order to confirm the identity of the ions arriving at the collecting grid, we now compare the inverse of the reduced mobility of the ions produced in the CF_4–C_2H_6 mixture as function of CF_4 relative concentration for a pressure of 8 Torr and E/N of 20 Td at room temperature with the mobility values expected from the Blanc's law for the main candidate ions: CF_3^+, $C_3H_n^+$ and $C_4H_n^+$. The results are presented in Figure 3.19. In the same figure, it is possible to see that our experimental values roughly follow the theoretical values predicted by Blanc's law with the Langevin limit for both $C_3H_n^+$ and $C_4H_n^+$ trend line up to 40% of CF_4, while for concentrations above this point, the experimental values deviate from $C_4H_n^+$ towards the trend line of CF_3^+. If we now look at the different reaction channels available, it is possible to see that CF_3^+ ions will transfer their charge to the C_2H_6 molecules, and we expect from the ion fraction calculations (in Figure 3.18) that the final ions should be $C_4H_n^+$, although having their mobility affected by the predecessor ion, CF_3^+, which is much slower.

After this analysis, it is possible to identify the peaks present. From pure C_2H_6 up to 15% of CF_4, only one peak was observed being due to a degree of overlap between the signal due to the three ($C_3H_n^+$) and four carbon ion groups ($C_4H_n^+$) which is due to both close ion mobility and to the space-charge effects at the GEM. Increasing the CF_4 concentration up to 75% gives rise to a split of the two peaks attributed to the same ion groups. Above this concentration, a third peak appears whose identification we could not infer, although we suspect it to be from collision of the drifting ions with impurities, namely, water.

Finally, no significant variation of the mobility was observed in the ranges of total pressure and of E/N studied. The results obtained are summarized in Table A.5 for E/N of 20 Td, V_{GEM} of 25 V and pressure of 8 Torr at room temperature (293 K).

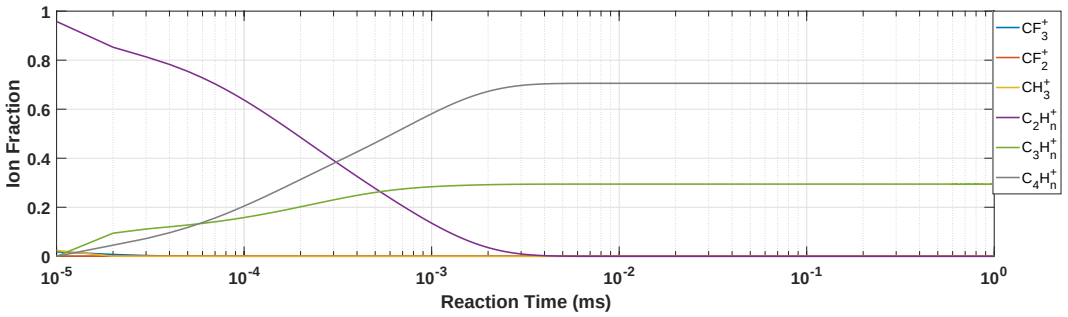

(a)

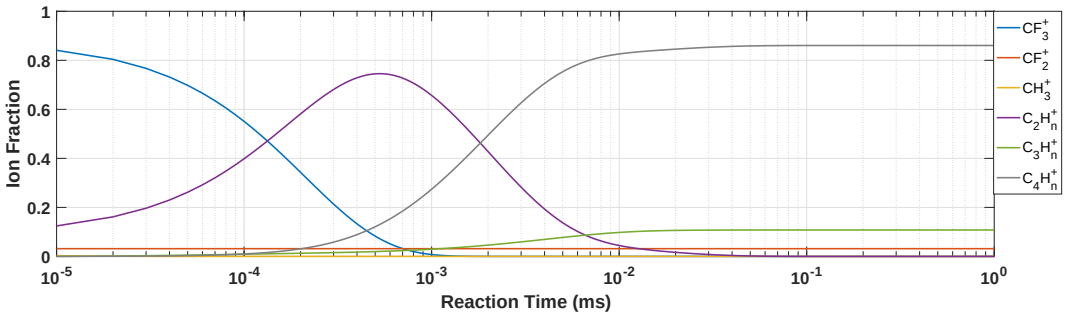

(b)

Figure 3.18: Fraction of the ions that can be formed as a function of the time in CF_4–C_2H_6 mixtures for 5% (a) and 95% (b) of Ar at a total pressure of 8 Torr.

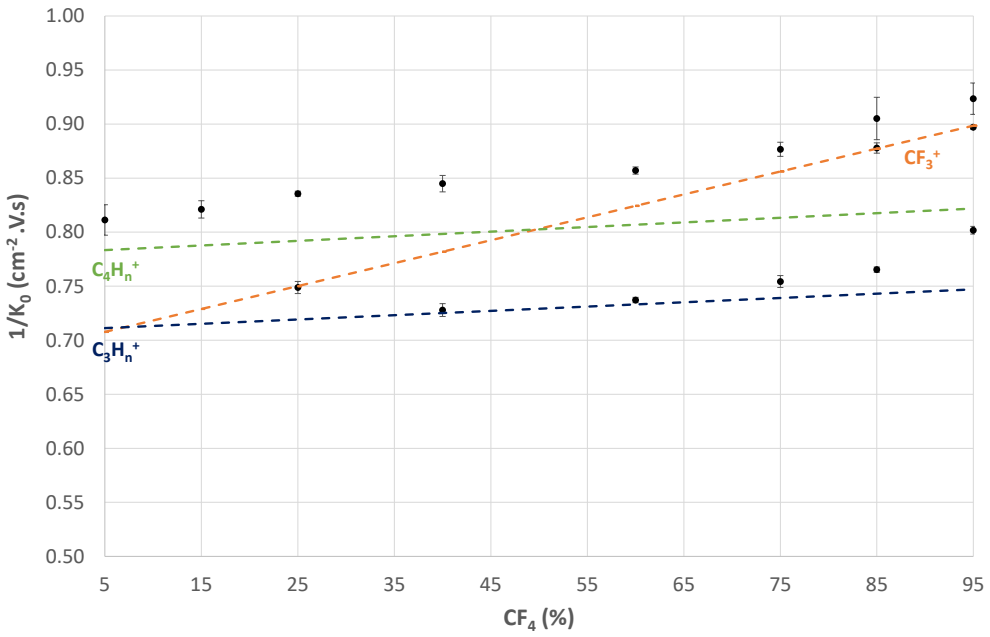

Figure 3.19: Inverse of the reduced mobility of the ions produced in the CF_4-C_2H_6 mixture as function of CF_4 relative concentration for a pressure of 8 Torr and E/N of 20 Td at room temperature. The dashed lines represent the mobility values expected from the Blanc's law for $C_4H_n^+$ (green), CF_3^+ (orange) and $C_3H_n^+$ (blue).

Carbon-tetrafluoride–Isobutane (CF_4–iso-C_4H_{10})

The mobility of the ions in carbon-tetrafluoride–isobutane (CF_4–iso-C_4H_{10}) mixtures was measured for E/N of 15 and 20 Td, for different total pressures (6-10 Torr) and for a constant V_{GEM} of 25 V at room temperature (293K).

Figure 3.20 displays the time-of-arrival spectra (average of 128 pulse) recorded for CF_4–iso-C_4H_{10} mixtures of 15%, 75%, 85% and 95% of CF_4 at total pressure of 8 Torr, reduced electric field of 15 and 20 Td, V_{GEM} of 25 V and at room temperature. As can be seen in the same figure, the number of peaks observed depends on the relative abundance of each gas. Also, increasing CF_4 concentrations, makes ions move faster, because of CF_4's lower mass and polarizability.

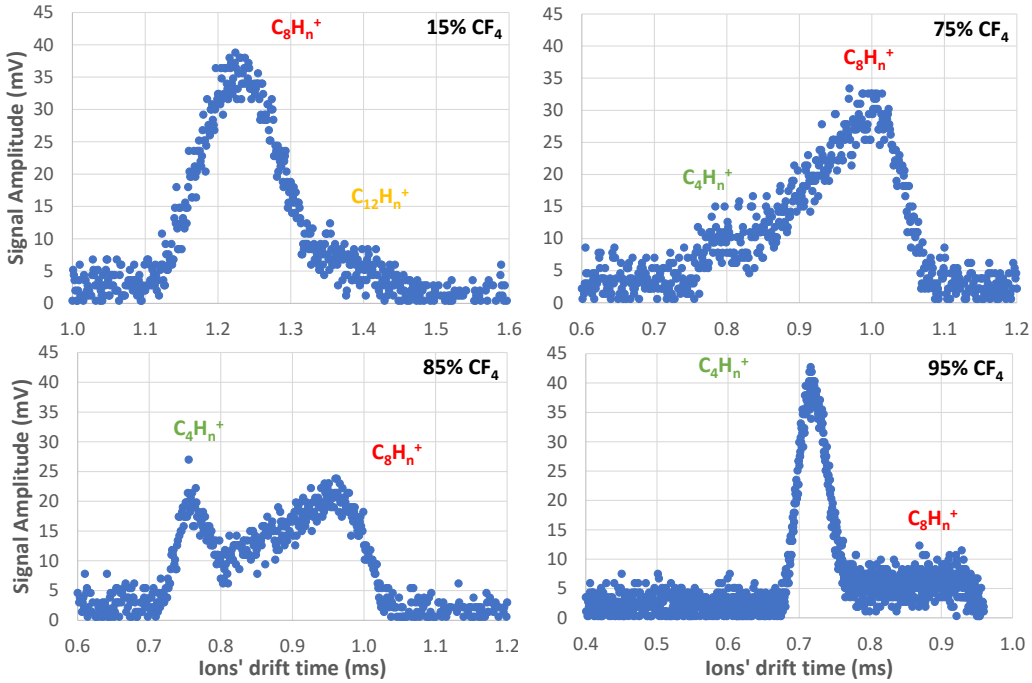

Figure 3.20: Time-of-arrival spectra (average of 128 pulse) recorded for several CF_4-iso-C_4H_{10} mixtures (15%, 75%, 85% and 95% of CF_4) at total pressure of 8 Torr, reduced electric field of 20 Td, V_{GEM} of 25 V and room temperature (293K).

For a V_{GEM} of 25 V, the primary ions produced in this mixture will be CF_3^+ ions, which will be predominantly produced from pure CF_4 down to about 84% CF_4, and 2-carbon ($C_2H_n^+$), 3-carbon ($C_3H_n^+$) and 4-carbon ($C_4H_n^+$) ion groups, as can be seen in Tables 3.2 and 3.7.

Unfortunately, the rate constants and product distributions for collisions between CF_4 ions with isobutane molecules could not be found in literature, thus calculations on the fraction of the ions that can be formed as a function of the time could not be done in this case. However the ionization energy of CF_4 (16.2 eV [79]) is considerably higher than the ionization energy of iso-C_4H_{10} (10.74 eV [75]), therefore it is expected that the CF_3^+ ions will transfer their charge to iso-C_4H_{10} molecules, ultimately leading to

the same ions as in pure isobutane, although with a different distribution since, as in the case of Ar–iso-C_4H_{10} mixtures presented earlier, the presence of CF_4 molecules should delay the formation of heavier ions.

Figure 3.21 shows the inverse of the reduced mobility of the ions produced in the CF_4-iso-C_4H_{10} mixture as function of CF_4 relative concentration for a pressure of 8 Torr and E/N of 20 Td at room temperature along with the mobility values expected from Blanc's law for the main candidate ions species: CF_3^+, $C_{12}H_n^+$, $C_8H_n^+$ and $C_4H_n^+$. As can be seen in the same figure, the behavior in terms of the mobility of the final ions observed is fairly well described by Blanc's law with Langevin limit within about 3% of mean deviation from the predicted mobility values.

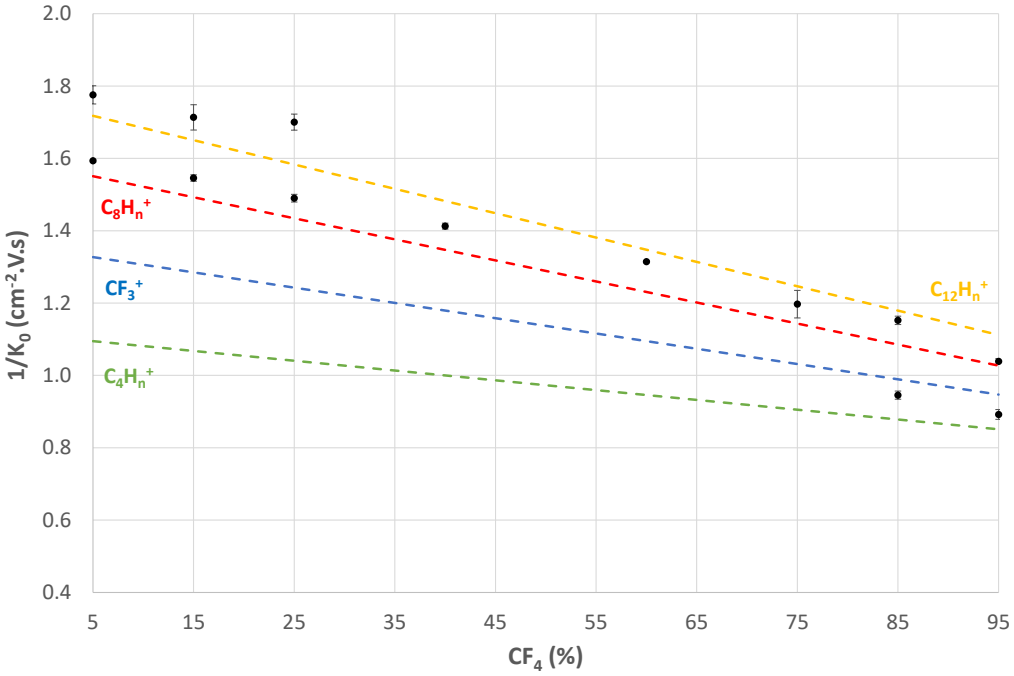

Figure 3.21: Inverse of the reduced mobility of the ions produced in the CF_4–iso-C_4H_{10} mixture as function of CF_4 relative concentration for a pressure of 8 Torr and E/N of 20 Td at room temperature. The dashed lines represent the mobility values expected from the Blanc's law for CF_3^+ (light blue), $C_{12}H_n^+$ (yellow), $C_8H_n^+$ (red) and $C_4H_n^+$ (green).

The time-of arrival spectra evolution with increasing CF_4 concentration in these mixtures (Figure 3.20) was found to be similar to the one in Ar—iso-C_4H_{10} mixtures with increasing Ar concentration (see Figure 3.11). From pure isobutane to 25% CF_4, two peaks are observed with the ions responsible for the peaks observed being the same as in pure isobutane: $C_{12}H_n^+$ for the peak with lower mobility and $C_8H_n^+$ for the peak with higher mobility. Increasing CF_4 concentration up to 75% of CF_4, only one peak was observed. The ions responsible for this peak are the $C_8H_n^+$ ions as the reactions leading to $C_{12}H_n^+$ ions do not complete during the drift time of the ions with increasing CF_4 concentration. Further increasing the CF_4 concentration, leads to the appearance of a peak with even higher mobility that should be due

to $C_4H_n^+$ ions. Nevertheless, the similar behavior under Blanc's law of the CF_3^+ ions and because we have no knowledge of the reaction rates involved between CF_3^+ ions and isobutane molecules, it is not possible to be sure of the nature of the final ions to be of $C_4H_n^+$. As we get to 95% of CF_4, the peak of lower mobility is almost unnoticeable and the peak attributed to $C_4H_n^+$ ions starts to be the predominant one.

No significant variation of the mobility of the ions was observed in the total pressure and E/N range studied. However the relative amplitude between the peaks present was seen to depend on the reduced electric field, this effect being more pronounced for higher values of E/N, because of the smaller drift times resulting in different ion fractions. The experimental results obtained are summarized in Table A.6 for E/N of 15 Td and of 20 Td, V_{GEM} of 25 V and pressure of 8 Torr at room temperature (293 K).

At last, it is important to note that in high pressure systems (near atmospheric), with the same mixtures studied here, the ions responsible for the peaks observed should be the $C_{12}H_n^+$ ions, whose mobility was not possible to measure across all the range of mixtures studied but, as proven here, can be predicted through Blanc's law with good accuracy.

3.2.4 Alternative mixtures for the LCTPC collaboration

In this section, the results for three different ternary mixtures of interest for the LCTPC collaboration will be presented and discussed, namely, in mixtures of Ar–CF_4–CH_4 (92-3-5), Ar–CF_4–C_2H_6 (94-3-3) and Ar–CF_4–iso-C_4H_{10} (95-3-2). The mixture ratios studied were proposed to us by the LCTPC collaboration.

Argon–Carbon-tetrafluoride–Methane (Ar–CF_4–CH_4)

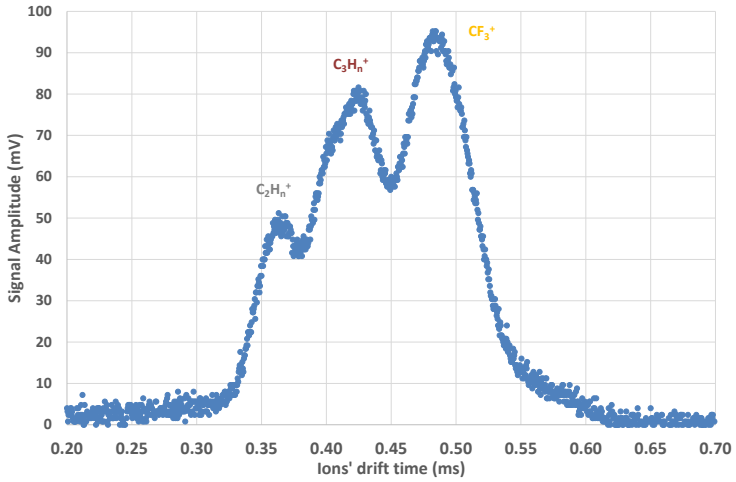

Figure 3.22: Time-of-arrival spectrum (average of 128 pulse) recorded for a 92-3-5 percent mixture of Ar-CF_4-CH_4 at total pressure of 8 Torr, reduced electric field of 15 Td, V_{GEM} of 25 V and room temperature (293K).

In the Ar–CF_4–CH_4 (92-3-5) mixture, three peaks are clearly visible for an E/N of 15 Td, for 8 Torr of total pressure and a V_{GEM} of 25 V at room temperature, as can be seen in the time-of-arrival spectrum shown in Figure 3.22.

Having in mind the discussions held in prior sections, it is expected that five different ions can be produced at the GEM in these conditions: Ar^+ (predominantly), CF_3^+, CH_4^+, CH_3^+ and CH_2^+ ions. As seen before in Ar-CF_4 mixtures (in Section 3.2.2) and in previous studies on Ar-CH_4 mixtures [38], Ar^+ tend to transfer all their charge to CF_4 and CH_4 molecules. In CF_4-CH_4 mixtures, again, the CH_5^+ ions, produced from reactions between CH_3^+ ions with CH_4 molecules, will further react with CF_4 molecules, producing CF_3^+ ions, while CH_2^+ will react with CH_4 molecules, producing $C_2H_n^+$ ions (n=2,3,4,5) and later $C_3H_n^+$ ions, while CH_3^+ ions can either react with CH_4 molecule, eventually producing $C_3H_n^+$, or with CF_4 molecules, producing CF_3^+.

Using the cross sections for electron impact, and the rate constants and product distribution of the reaction involved (already presented in Tables 3.1, 3.2, 3.3, 3.13, and 3.15), the fraction of the ions that can be formed as a function of the time In the Ar–CF_4–CH_4 (92-3-5) mixture at a total pressure of 8 Torr were calculated. The results are displayed in Figure 3.23 and show that three kinds of ions arriving at the collection grid, therefore should appear in the spectrum: CF_3^+, $C_2H_n^+$ and $C_3H_n^+$.

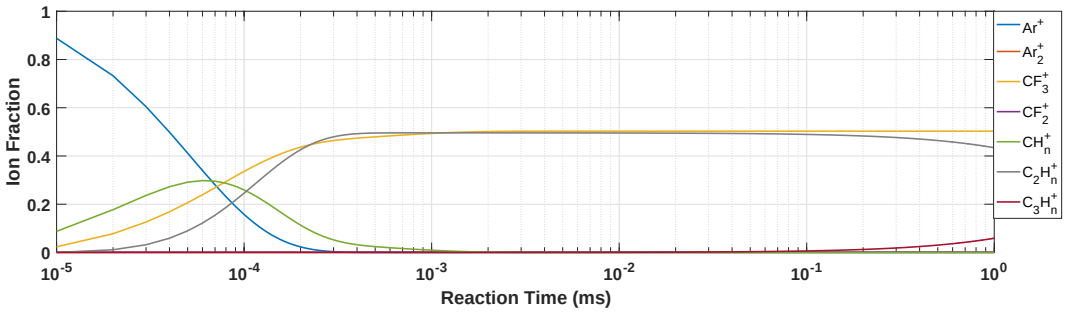

Figure 3.23: Fraction of the ions that can be formed as a function of the time in the Ar–CF_4–CH_4 (92-3-5) mixture at a total pressure of 8 Torr.

In Table 3.17, the results for the reduced mobility of the peaks present in the time-of-arrival spectra for an E/N of 15 Td, 8 Torr total pressure and a V_{GEM} of 25 V at room temperature, the predicted values expected from Blanc's law with the Langevin limit for the main candidate ions and the theoretical deviations of the experimental results obtained are summarized.

Table 3.17: Reduced mobility of the peaks (1 to 3 from left to right) present in the time-of-arrival spectra in the Ar–CF_4–CH_4 (92-3-5) mixture for an E/N of 15 Td, 8 Torr total pressure and a V_{GEM} of 25 V at room temperature, predicted values expected from Blanc's law with the Langevin limit for the main candidate ions (CF_3^+, $C_2H_n^+$ and $C_3H_n^+$) and the theoretical deviations of the experimental results.

Mobility at 15 Td	Theor. Mobility	Theor. Deviation
K_1 = 2.95±0.02 $cm^2V^{-1}s^{-1}$	$K_{C_2H_n^+}$ = 3.12 $cm^2V^{-1}s^{-1}$	5.4%
K_2 = 2.55±0.02 $cm^2V^{-1}s^{-1}$	$K_{C_3H_n^+}$ = 2.40 $cm^2V^{-1}s^{-1}$	7.4%
K_3 = 2.19±0.01 $cm^2V^{-1}s^{-1}$	$K_{CF_3^+}$ = 2.15 $cm^2V^{-1}s^{-1}$	1.9%

By comparing the experimental values obtained for each peak with the theoretical values expected from Blanc's law with the Langevin limit for the main candidate ions, it is possible to see that our results are in a fair agreement with these values within a mean deviation of about 4.5%. This means that the ions responsible for the peaks observed should be the ones mentioned.

It is important to note that the mobility for $C_3H_n^+$ is higher than expect and that should be due to the the influence of its predecessor ions, the $C_2H_n^+$ ions, which are lighter, and so have a higher mobility.

Finally, two peaks are expected to be present in high pressure systems, originated either by CF_3^+ or by $C_3H_n^+$ ions, since the $C_2H_2^+$, $C_2H_3^+$ and $C_2H_5^+$ ions eventually produce $C_3H_n^+$ upon colliding with CH_4 molecules, thus only a small fraction of $C_2H_n^+$ ions (corresponding to $C_2H_4^+$ ions) will arrive at the collecting grid (less than 5% at atmospheric pressure). Despite the fact that these ion mobility measurements have been consistently in accordance with the ones obtained at higher pressures [20], our experimental results should be carefully analyzed before using them to describe the mobility of the $C_3H_n^+$ ions at higher pressure, as the mobility obtained seem to be influenced by their predecessor ions. Moving to higher pressure may also lead to a residual fraction of Ar_2^+ ions arriving at the collecting grid, thus contributing to the signal formation.

Argon–Carbon-tetrafluoride–Ethane (Ar–CF_4–C_2H_6)

In the Ar–CF_4–C_2H_6 (94-3-3) mixture, two peaks are clearly visible as well as a long tail at the right of the peaks for an E/N of 15 Td, 8 Torr total pressure and a V_{GEM} of 25 V at room temperature, as can be seen in the time-of-arrival spectrum shown in Figure 3.24.

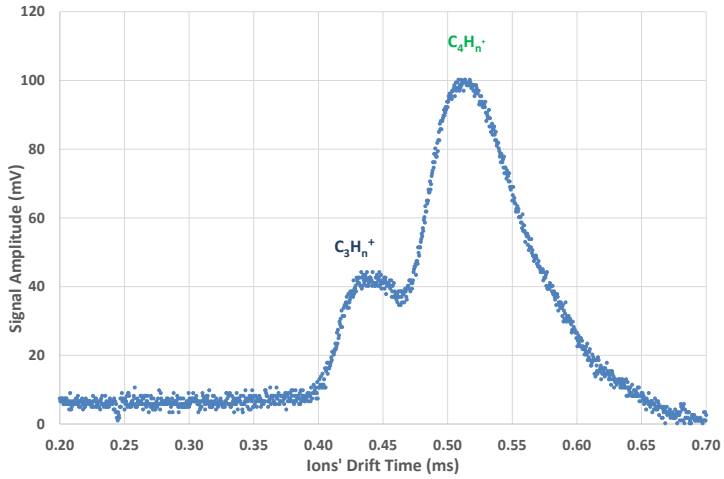

Figure 3.24: Time-of-arrival spectrum (average of 128 pulse) recorded for a 94-3-3 percent mixture of Ar-CF_4-C_2H_6 at total pressure of 8 Torr, reduced electric field of 15 Td, V_{GEM} of 25 V and room temperature (293K).

As discussed before, in the binary mixtures involving Ar–C_2H_6 and CF_4–C_2H_6 (Sections 3.2.2 and 3.2.3), both Ar^+ (predominantly) and CF_3^+ primary ions will transfer their charge to C_2H_6 molecules, ultimately leading to the formation of 3-carbon ($C_3H_n^+$) and 4-carbon ($C_4H_n^+$) ion groups, as in the case of pure C_2H_6. The fraction of the ions that can be formed as a function of the time in the Ar–CF_4–CH_4 (92-3-5) mixture at a total pressure of 8 Torr was calculated using both the cross sections for electron impact of the gases present along with the rate constants and product distribution for the collisions of the ions and molecules involved. The results obtained are displayed in Figure 3.25 and show that two kinds of final ions should be represented in the spectrum: $C_3H_n^+$ and $C_4H_n^+$ for the experimentally observed drift time.

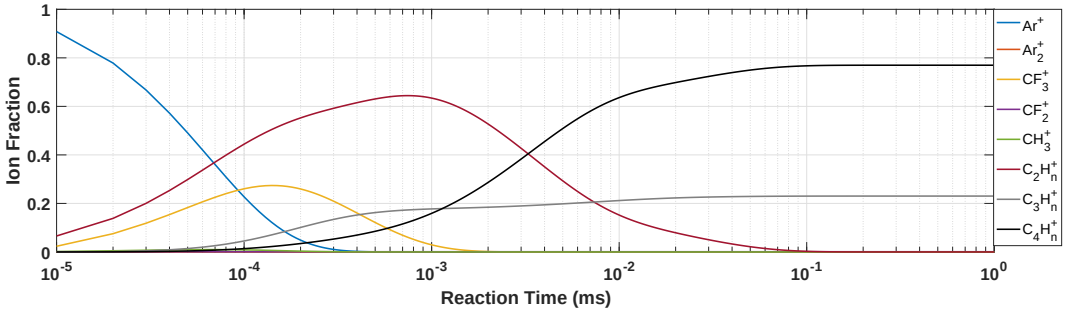

Figure 3.25: Fraction of the ions that can be formed as a function of the time in the Ar–CF_4–C_2H_6 (94-3-3) mixture at a total pressure of 8 Torr.

In Table 3.18, the results for the reduced mobility of the peaks present in the time-of-arrival spectra for an E/N of 15 Td, 8 Torr total pressure and a V_{GEM} of 25 V at room temperature are summarized along with the predicted values expected from Blanc's law with the Langevin limit for the main candidate ions and the theoretical deviations of the experimental results obtained.

Table 3.18: Reduced mobility of the peaks (1 to 2 from left to right) present in the time-of-arrival spectra in the Ar–CF_4–C_2H_6 (94-3-3) mixture for an E/N of 15 Td, 8 Torr total pressure and a V_{GEM} of 25 V at room temperature, predicted values expected from Blanc's law with the Langevin limit for the main candidate ions ($C_3H_n^+$ and $C_4H_n^+$) and the theoretical deviations of the experimental results.

Mobility at 15 Td	Theor. Mobility	Theor. Deviation
K_1 = 2.50±0.03 cm^{2}V^{-1}s^{-1}	$K_{C_3H_n^+}$ = 2.31 cm^{2}V^{-1}s^{-1}	8.4%
K_2 = 2.07±0.02 cm^{2}V^{-1}s^{-1}	$K_{C_4H_n^+}$ = 2.15 cm^{2}V^{-1}s^{-1}	3.4%

By comparing the experimental values obtained for each peak with the theoretical values expected from Blanc's law with the Langevin limit for the main candidate ions, it is possible to see that our results are in fair agreement within a theoretical deviation of about 8.4% and 3.4%, respectively, thus corroborating the identification suggested earlier.

Additionally, it is important to stress out that the long tail visible may be due to the $C_5H_{11}^+$ ions, as explained for the Ar–C_2H_6 mixtures. Also the mobility measured for $C_3H_n^+$ was higher than the one predicted theoretically using Blanc's law with the Langevin limit and that may be due to the fact that its predecessor ion ($C_2H_n^+$) displays higher mobility, which may end up increasing the their overall measured mobility.

Finally, increasing the working pressure, we expect the same two peaks with a long tailed are expected will be present, therefore contributing to the signal. Again, as in Ar–CF_4–CH_4 mixture, our experimental results for high pressure (near atmospheric) systems should be carefully analyzed when using them to predict the mobility of the $C_3H_n^+$ ions, as in our case, the experimental mobilities obtained for these ions seem to be influenced by their predecessor ions. Also, as in the previous case, a small fraction of Ar_2^+ ions is expected to reach the collecting grid, thus contributing to the generated signal.

Argon–Carbon-tetrafluoride–Isobutane (Ar–CF_4–iso-C_4H_{10})

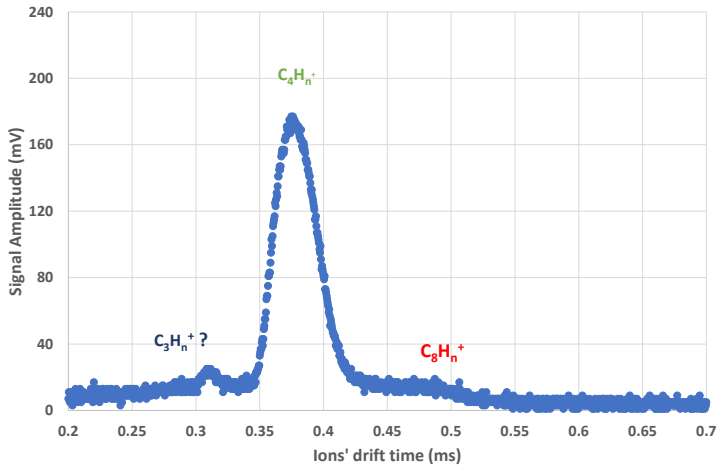

Figure 3.26: Time-of-arrival spectrum (average of 128 pulse) recorded for a 95-3-2 percent mixture of Ar-CF_4-iso-C_4H_{10} at total pressure of 8 Torr, reduced electric field of 20 Td, V_{GEM} of 25 V and room temperature (293K).

In the Ar–CF_4–iso-C_4H_{10} (95-3-2) mixture, three peaks are visible for a E/N of 20 Td, 8 Torr total pressure and a V_{GEM} of 25 V at room temperature, as can be seen in time-of-arrival presented in Figure 3.26. In the same figure, it is possible to see, from left to right, a first peak with small amplitude (displaying higher mobility), a second with a higher amplitude (with an intermediary) mobility and a third which is broader also with low amplitude (displaying lower mobility).

As discussed in the binary mixtures involving Ar–iso-C_4H_{10} and CF_4–iso-C_4H_{10} (Sections 3.2.2 and 3.2.3), both Ar^+ (predominantly), and CF_3^+ primary ions should transfer their charge to iso-C_4H_{10} molecules, ultimately leading to the formation of $C_{12}H_{25}^+$ and $C_{12}H_{26}^+$ ions, as in the case of pure isobutane. Although no reactions were found in literature between CF_3^+ ions and iso-C_4H_{10} molecules, the similarities between the time-of-arrival spectra of the Ar–CF_4–iso-C_4H_{10} (95-3-2) mixture, in Figure 3.26, and that of the Ar–iso-C_4H_{10} (98-2) mixture presented in Figure 3.27 for the same conditions as the previous one, support this assumption. Therefore, the central large peak should be due to $C_4H_n^+$ ions, while the small peak at its left is expected to be originated by $C_3H_n^+$ ions and the broad peak at its right by $C_8H_n^+$ ions.

In Table 3.19, the results for the reduced mobility of the peaks present in the time-of-arrival spectra for an E/N of 15 Td, 8 Torr total pressure and a V_{GEM} of 25 V at room temperature are summarized along with the predicted values expected from Blanc's law with the Langevin limit for the main candidate ions and the theoretical deviations of the experimental results obtained.

Comparing the experimental results for the main peak with the mobility obtained from Blanc's law and Langevin theory for the $C_4H_n^+$ ions, reveals a remarkable agreement with the experimental result, with only about 0.5% deviation from the theoretical ones. For the broader peak, at the right side of the main

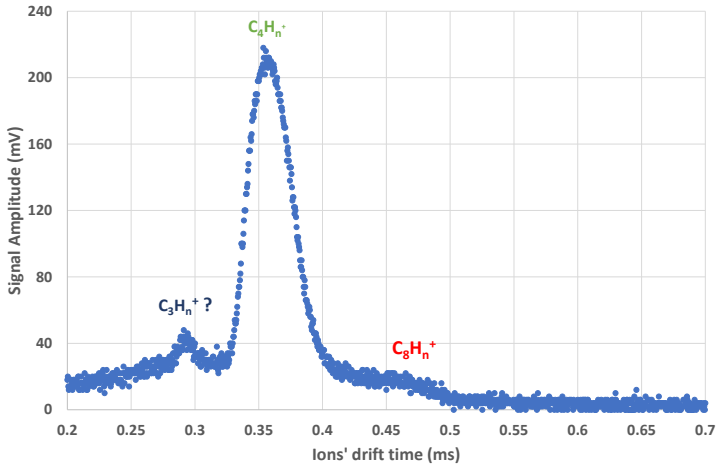

Figure 3.27: Time-of-arrival spectrum (average of 128 pulse) recorded for a 98-2 percent mixture of Ar-iso-C_4H_{10} at total pressure of 8 Torr, reduced electric field of 20 Td, V_{GEM} of 25 V and room temperature (293K).

Table 3.19: Reduced mobility of the peaks (1 to 3 from left to right) present in the time-of-arrival spectra in the Ar–CF_4–iso-C_4H_{10} (95-3-2) mixture for an E/N of 15 Td, 8 Torr total pressure and a V_{GEM} of 25 V at room temperature, predicted values expected from Blanc's law with the Langevin limit for the main candidate ions ($C_3H_n^+$, $C_4H_n^+$, $C_8H_n^+$ and $C_{12}H_n^+$) and the theoretical deviations of the experimental results.

Mobility at 15 Td	Theor. Mobility	Theor. Deviation
K_1 = 2.67±0.04 $cm^2V^{-1}s^{-1}$	$K_{C_3H_n^+}$ = 3.12 $cm^2V^{-1}s^{-1}$	18.6 %
K_2 = 2.16±0.02 $cm^2V^{-1}s^{-1}$	$K_{C_4H_n^+}$ = 2.15 $cm^2V^{-1}s^{-1}$	0.5 %
K_3 = 1.72±0.07 $cm^2V^{-1}s^{-1}$	$K_{C_8H_n^+}$ = 1.86 $cm^2V^{-1}s^{-1}$	7.5%
-	$K_{C_{12}H_n^+}$ = 1.77 $cm^2V^{-1}s^{-1}$	-

one, the experimental mobility agrees within 7.5% with the predicted one, thus confirming the identity of the ion responsible ($C_4H_n^+$), however less precisely due to fitting difficulties. For the smaller peak, at the left of the main peak, the deviation is high (18%) and not much can be said about its identity, as it was not possible to confirm that the group of ions responsible was $C_3H_n^+$.

Additionally, it is very important to stress out that the final ions observed will be strongly dependent on the gas pressure. Increasing the pressure and/or the drift distance will lead to the formation of heavier ions, ultimately resulting in a one peak signal due to the $C_{12}H_n^+$ ions. Moving to higher pressure may also lead to a residual fraction of Ar_2^+ ions arriving at the collecting grid, thus contributing to the signal formation.

Please note that, even at the atmospheric pressure (760 Torr), reactions leading to $C_{12}H_n^+$ and $C_8H_n^+$ ions take a few ms and few hundreds of μs to complete, thus the ions formed in the multiplication areas of large gaseous detector, as the LCTPC, should quickly drift as smaller ions from that area before the formation of heavier ions, thus producing low space charge effects.

Chapter 4

Development of a Dual-Polarity Ion Drift Chamber

The last studies conducted in our group on the ion transport properties in gases, make use of the techniques conceived and of the experimental system developed by P. N. B. Neves [31] to perform measurements on the mobility of positive ions at pressures below the atmospheric one, for a fixed drift distance and for reduced electric fields below 45 Td .

As a lower pressure system, one of the major limitations of the existing chamber in measuring the mobility of the ions in mixtures of interest for large gaseous detectors is that the ions responsible the time-of-arrival spectra obtained may not be the same ones drifting in high pressure detectors, as its origin depends on the rate constants and product distributions for the collisions between the ions and the gas atoms/molecules, and so on the gas total pressure. However, if possible, varying the drift distances, would allow to study the mobility of ions produced by both slower and faster reactions between the ions and the gas atoms/molecules. Since all chemical reactions occur during the drift of the ions, if the drift time is smaller than the mean time needed for the reaction to be complete, both primary and secondary ions will be caught at the collecting grid. However, if the drift distance is increased, the same reactions can be completed during the drift time and the final ions caught at the collecting grid will be different. Thus, this technique would allow to draw conclusions for the ions drifting in gases at different pressures or drift lengths conditions.

Additionally, due to its intrinsic characteristics, the present system does not allow to measure the mobility of negative ions. Nevertheless, relevant data on the transport properties of these ions in gases and mixtures of interest is scarce and of uttermost importance for the development of NITPCs.

Thus, in order to expand the knowledge on the transport properties of ions in gases, a new experimental system, the Dual-Polarity Ion Drift Chamber (DP-IDC), was developed in the scope of this work for measuring the mobility of both positive and negative ions for different drift distances and, as in the previous system, for pressures below atmospheric one and for reduced electric fields below 45 Td, with the main objective of performing experimental measurements on ion mobility, and eventually diffusion, for both negative and positive ions, in mixtures of interest for NITPCs and other large gaseous detectors.

The system was then designed using SolidWorks® software, then constructed at LIP-Coimbra workshop, and finally assembled and tested in the laboratory. In this chapter, the working principle and several aspects of the development of the DP-IDC, as well as studies on its limitations and critical aspects, together with the first experimental results, will be presented.

4.1 Working principle

The working principle of this chamber is quite similar to the one presented in Section 3.1.2 with the main difference being that it is symmetrical with reference to the GEM. Each measurement starts with the flash of the Xe UV lamp, that emits photons with a 10 Hz frequency and a pulse duration shorter than 0.5 μs, which releases photoelectrons from the 300nm thick CsI photocathode deposited on the top electrode of the GEM.

While drifting through the GEM holes, these photoelectrons will gain energy from the electric field and collide with the gas atoms/molecules, resulting in the production of either positive ions, by electron impact ionization, whenever the energy of the electrons is higher than the gas ionization threshold, or negative ions, by electron attachment to the electronegative atoms/molecules of the gas.

As each ion group leaves the GEM holes, it starts drifting under a uniform electric field towards a Frisch grid, one in each end of the drift chamber.

When a group of ions crosses one of the Frisch grids, a signal is induced on the collecting grids, that is converted from current to voltage by a pre-amplifier, coupled to each end, recorded in a digital oscilloscope (as an average of 128 pulses) and finally fed to a PC for processing and storage.

A schematic diagram of the working principle of this system, is presented in Figure 4.1.

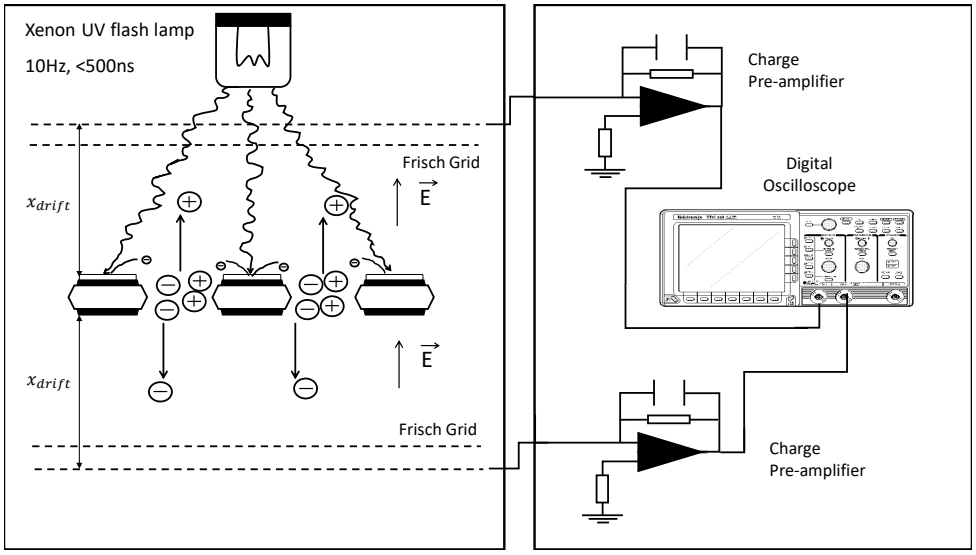

Figure 4.1: Schematic diagram of the system working principle of the DP-IDC.

4.2 Design proposal and system components

The experimental system consists on a stainless steal, vacuum sealed, gas vessel. Ions are produced in its center and then will be guided upwards or downwards, depending on their polarity, by one of the drift chambers to a double grid structure, where the signal will be formed and collected.

In Figure 4.2, the inside and outside drafts of the experimental system are showed.

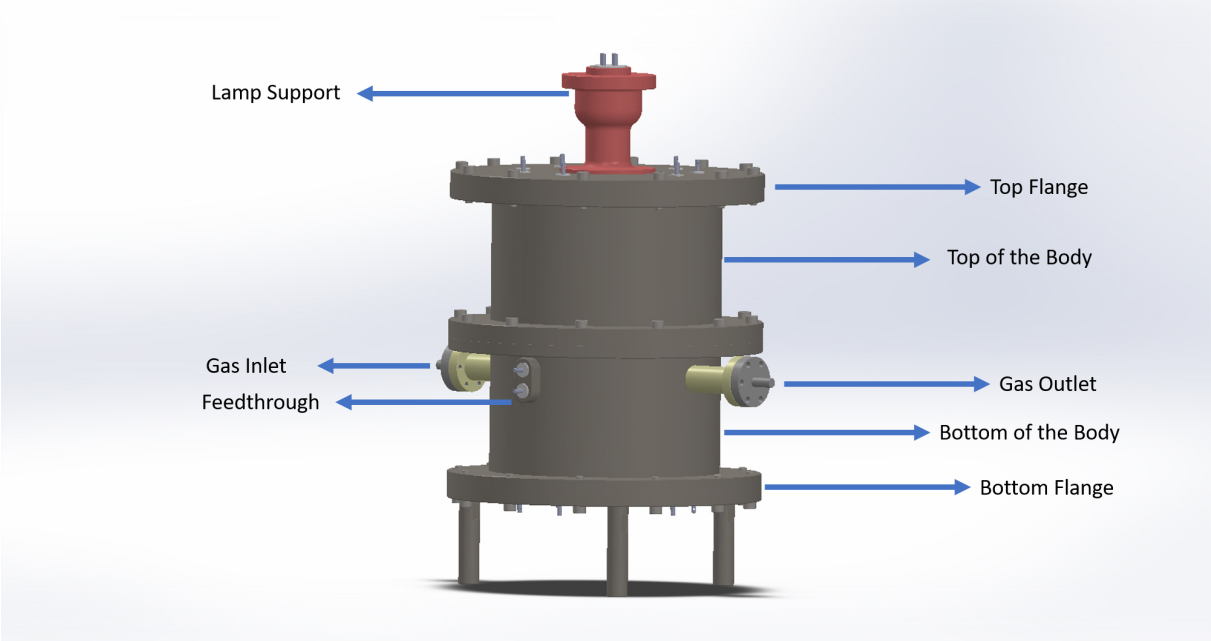

(a)

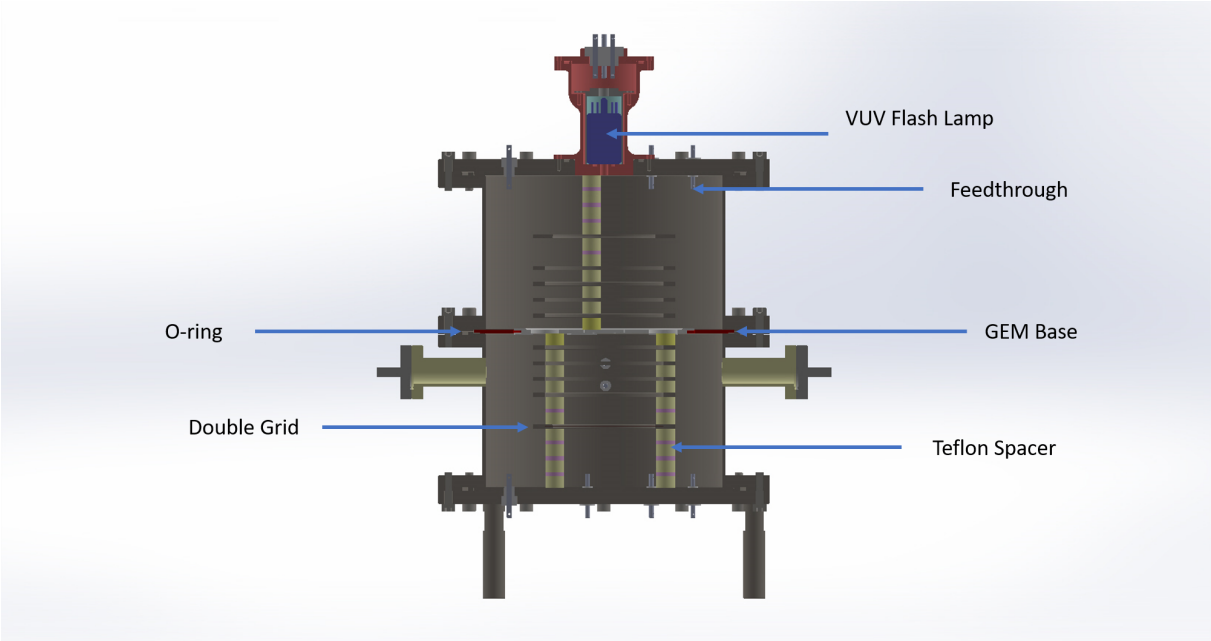

(b)

Figure 4.2: Experimental system outside (a) and inside (b) drawings.

In order to be functional, several requirements have been met upon the system design. First, the system was designed to be modular and symmetrical with respect to the GEM base in order to both

Figure 4.3: Photograph of the feedthroughs after the gluing process.

minimize the time required for its installation and the access to its inside. A quick installation is required, within a maximum of 10 min, in order to reduce exposure of the CsI photocathode to the air humidity. With easy access to its inside, it will be possible to replace components or add/remove field rings in order to change the ions' drift distance.

The outside of the chamber (see Figure 4.2(a)) is composed by the lamp support, top and bottom flanges (each one with eight electric feedthroughs) and top and bottom parts of the body. Additionally, in the bottom part of the body, a gas inlet/outlet and two electric feedthroughs are located.

Figure 4.3, shows a photograph of the electrical feedthroughs that consist on a bar of stainless steel that was glued to a Teflon casing to electrically isolate them from the chamber body. These electrical feedthroughs allow to feed the high voltage to the different components inside the chamber and in order to assure vacuum sealing, were also glued to detector with a proper vacuum glue.

In order to support the lamp, making it easier to be replaced, keeping it stable during operations and vacuum sealing the detector, while optimizing the light that is able to reach the photochatode deposited in the top electrode of the GEM, a support for the UV L2439 Hamamatsu lamp was designed inside the detector. Photographs of the lamp and its support can be found in Figure 4.4, where it is possible to see that the lamp is tightly placed inside this structure. The structure is then fixed to the top flange of the detector and vacuum sealed with a Viton O-ring and by a flange screwed at the top of this structure.

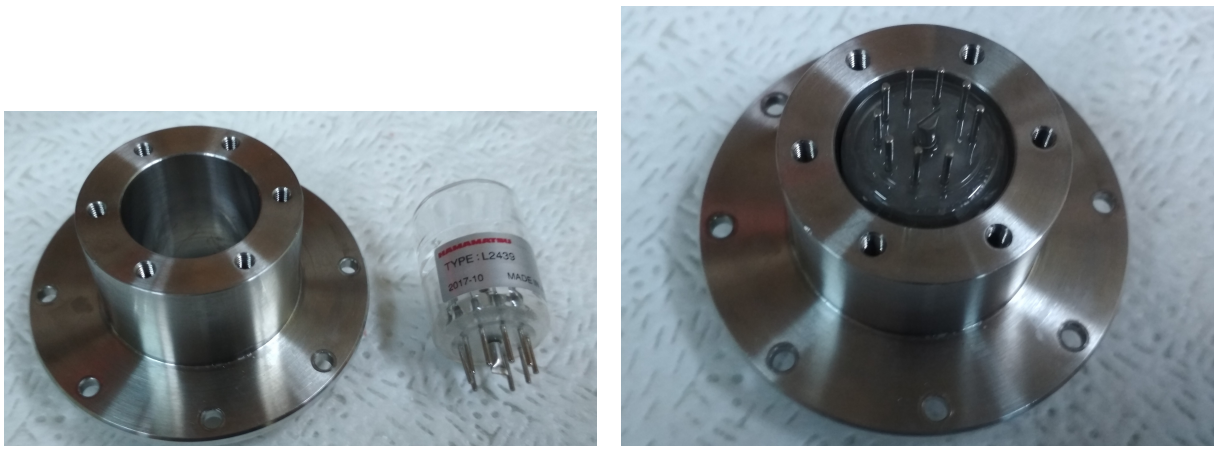

(a) (b)

Figure 4.4: Photos of the L2439 Hamamatsu lamp and of its support structure on the detector.

Also, both the top and bottom flanges have been designed to fit in eight feedthroughs that will allow to bias the internal structures of the field cage and the grids. Also, coupled to the bottom part of the detector, are the gas inlet/outlet, one for gas admission and other which was adapted to place a pressure sensor, as well as two feedthroughs that will be used to bias the GEM electrodes. All the different modules are vacuum sealed with Viton O-rings.

The walls and flanges thicknesses, of about 5mm, were calculated to support the differential of pressure between the outside and the inside of the detector and will be screwed to each other through twelve M4 screws.

Inside, the experimental system is composed by two (top and bottom) drift chambers, symmetrically placed in respect to the GEM support, as can be seen in Figure 4.2(b).

In Figure 4.5 a picture of the interior of the bottom part of the detector is presented.

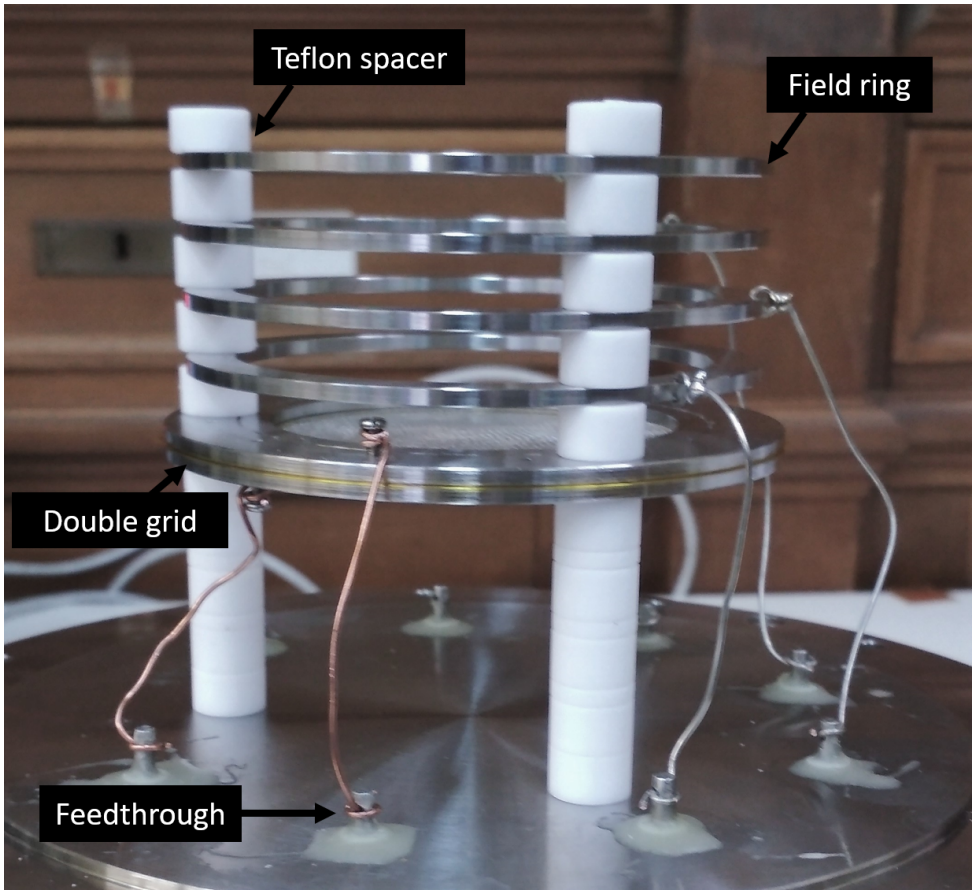

Figure 4.5: Photograph of the assembly of the field cage with the second double grid prototype.

To ensure a uniform electric field in the drift region, a field cage was designed for this chamber. This field cage is composed of 75 mm internal diameter stainless steal rings, separated by 7.5 mm long Teflon spacers that are placed above and below the GEM base. The rings are biased at regularly spaced voltage steps using a voltage divider that connects the feedthroughs through electric resistances on the outside of both the top and bottom flanges. Each field cage is composed of up to six field rings, one double grid, several Teflon spacers and three bars to hold the spacers. Since the drift distance must be well known for measuring the mobility of ions with great accuracy, in order to support and maintain the

field cage in the same position, these bars are screwed to the top and bottom flanges. The two cages are symmetrical and the one at the top will be used for measuring the mobility of positive ions, while the other, at the bottom, for measuring the mobility of negative ions. The walls are far enough from the field rings to avoid electrical discharges between the field cage and the wall.

To maintain the GEM at the center of the detector, a support structure was designed. In Figure 4.6, a photograph of the GEM base mounted in the bottom part of the detector is shown, where its is possible to see that the GEM is fixed at the center of a Teflon structure which is mounted on a metallic structure fixed at the detector body. Also, in the same figure, it is possible to see how the GEM is biased through two holes drilled in the Teflon structure. Finally, several holes were done in the Teflon and metal discs in order to allow free flowing of the gases inside the chamber.

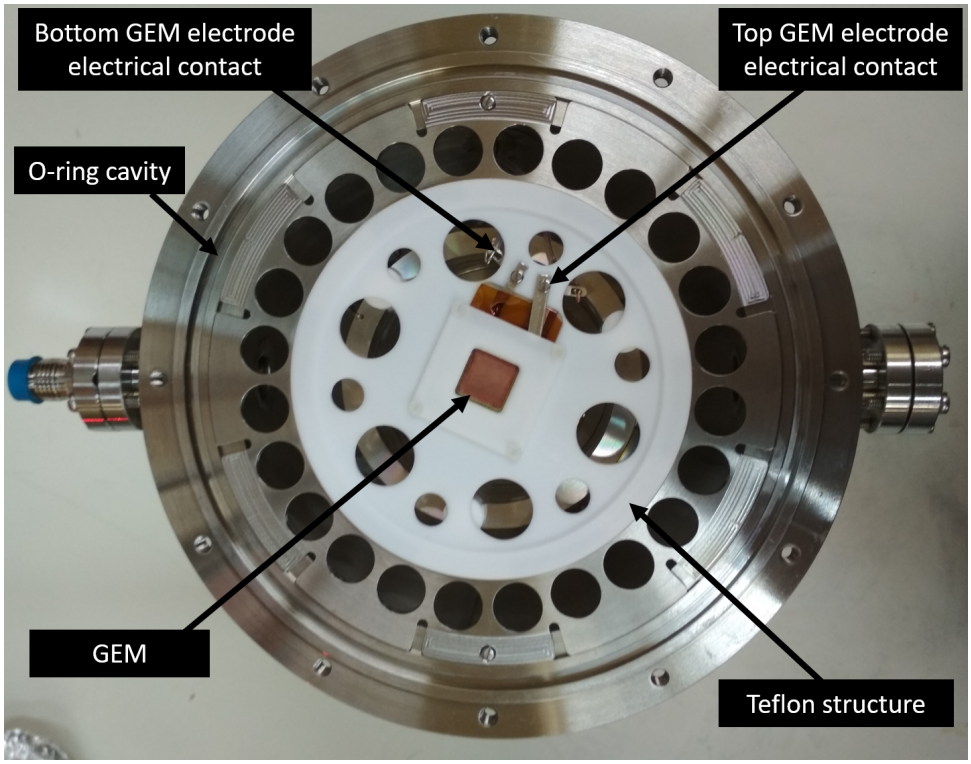

Figure 4.6: Photograph of the GEM base assembled.

The double grid is a critical component of this experimental system since its function is to shape and collect the charge signal induced by the ions transversing it. In order to correctly function, the two grids should be separated by a very small fixed distance (few tenths of mm) and be as uniformly stressed as possible, insuring a uniform electric field without electric wire contact between them. In Figure 4.7, photographs of the two double grid prototypes developed are presented.

The first prototype (in Figure 4.7(a)) was constructed by pressuring one stainless steel ring to tight cavities (one in each side) in the Teflon base, while stretching the grid between them. In the initial tests, the grids remained uniformly stretched and no electrical contact between them was identified, but after a few days, probably due to the high thermal expansion coefficient of Teflon, the grids started to get loose and an electric contact was identified, rendering this prototype useless.

In the second prototype (in Figure 4.7(b)) instead of a bulk Teflon center with two cavities, two stain-

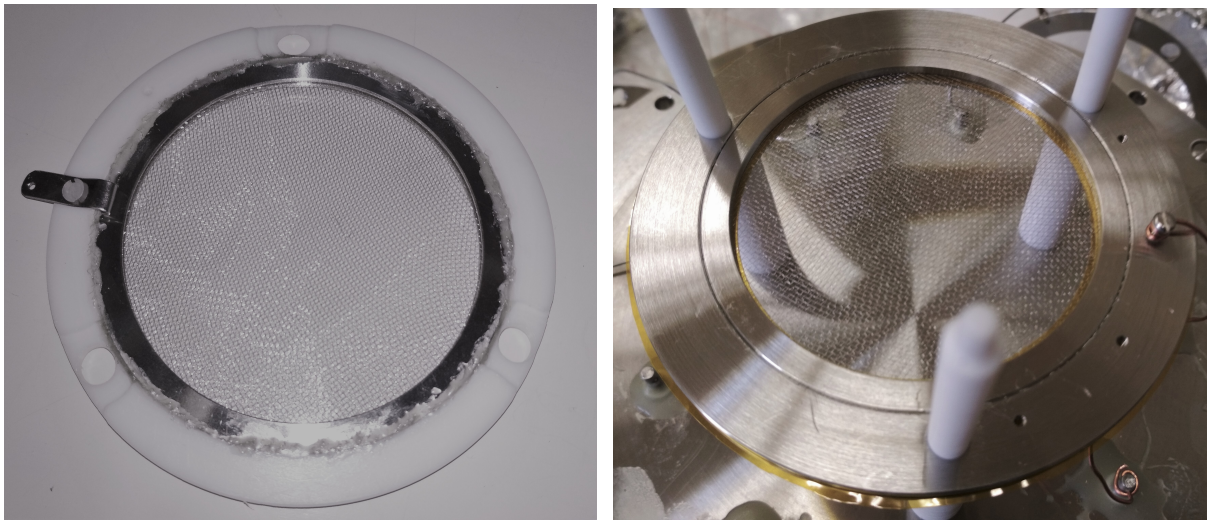

(a) (b)

Figure 4.7: Photographs of the first (a) and second (b) double grid prototypes.

less steel pieces were designed with one cavity each, in order to stretch the grids with the help of a stainless steal ring. A 24.7 μm thick Kapton ring foil was then introduced between these two metallic rings in order to achieve electrical insulation between them. The distance between the grids was augmented from 0.5 mm to about 0.62 mm in order to decrease the probability of electrical contact of the grids with time.

4.3 Preliminary tests

After the construction of the system at the LIP workshop, several tests on the electrical properties and vacuum quality were conducted in order to ensure a safe and reliable operation of the experimental system.

Before fully assembling the chamber, all contacts inside the detector were tested using a multimeter ensuring that the GEM and all field rings worked properly. Since no leak currents were found and all contacts were functioning correctly, tests on the installation between the Frisch and collecting grids followed, which failed in a first prototype, as explained in the previous section, leading to the construction of a second prototype which yielded acceptable results upon testing.

Then, several vacuum quality tests were performed in order to ensure that the chamber tightness was adequate and therefore reducing the risk of contamination from outside gases and impurities resulting from leaks. For that purpose, the system was vacuum pumped and the vacuum quality monitored using the pressure gauge of the pumping station. Whenever doubts about possible leaks existed, the detection of those leaks was performed by evaluating the change of pressure when acetone or alcohol was applied in junctions and connectors of the detector. When a vacuum of 10^{-6} Torr at the pump head was obtained, no considerable leaks were detected and the chamber was considered ready to operate.

Finally, tests on the outside electric contacts were made, revealing that the conditions needed to operate the detector were met.

4.4 Assembly

After the preliminary tests were successfully executed, the experimental system was finally assembled.

First, the chamber was installed by connecting the gas inlet in the existing vacuum line. Then, a 300 nm thick CsI film was vacuum evaporated in an appropriate evaporation plant. The GEM was then quickly installed on its support in about three minutes, allowing us to finally close the chamber.

While the system was vacuum pumped down to about 10^{-6} Torr at the head of the pump, the necessary electric apparatus for taking measurements on the mobility of positive ions, with only the top part of the detector biased, was installed. The detector body and upper collecting grid were grounded and a voltage divider was placed by connecting 22 MΩ resistances from the Frisch grid all the way through the field rings to the top GEM electrode.

When the vacuum quality goal was achieved, both the GEM and double grid were biased by two different DC power supplies in series with the resistance chain, which was biased by a HV power supply. After the power supplies were installed, the experimental system was finally ready for the first tests.

In Figure 4.8, a photograph of the final assembly of the experimental system in the vacuum line is shown.

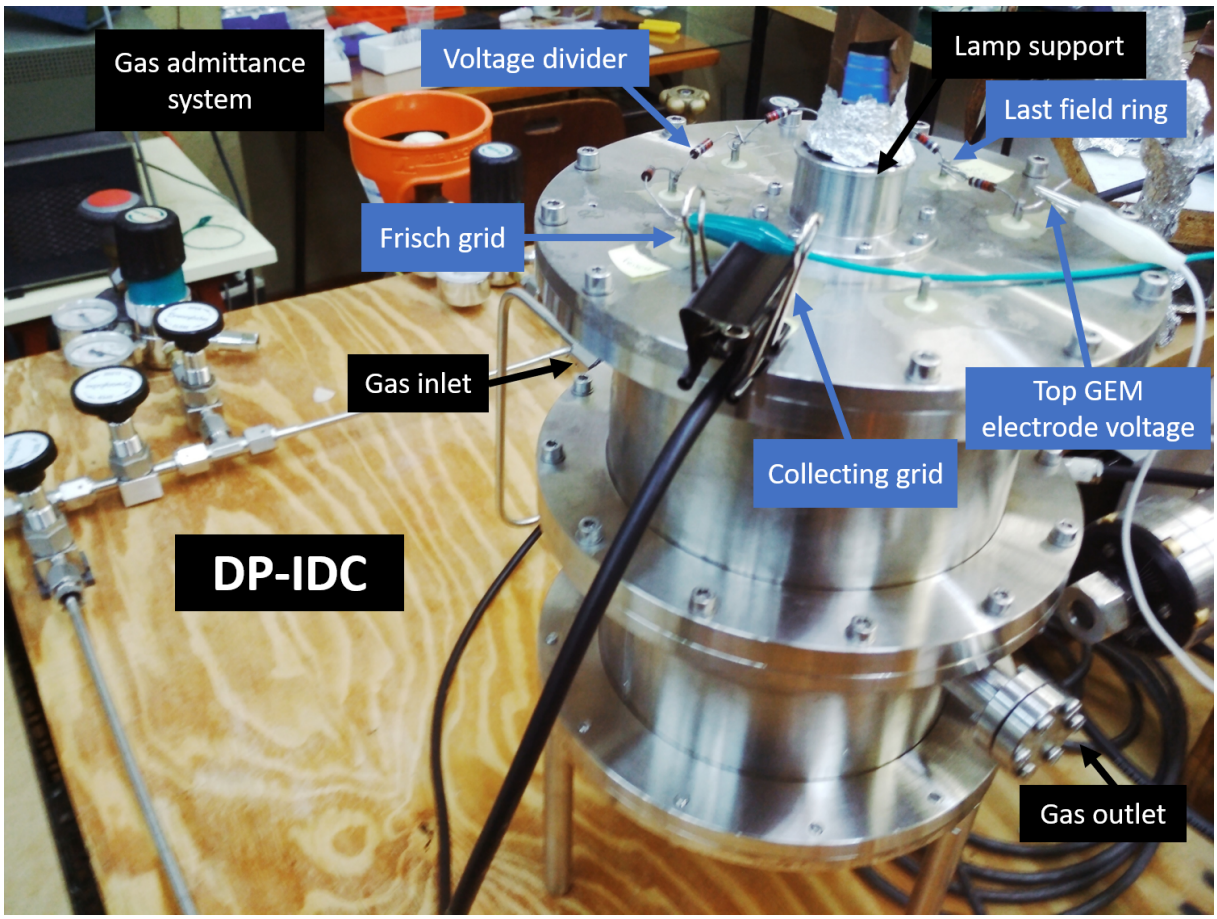

Figure 4.8: Photograph of the prototype final assembly of the DP-IDC in the vacuum line.

4.5 Limitations and critical aspects of the experimental system

As in every vacuum system, limitations arise from the effects of the impurities due to system outgassing and due to impurities on the gas used. Specially if they are polar or highly polarizable. In that case, those impurities will produce clusters or if they have a low ionization potential they can be ionized at the expense of primary ions through charge transfer processes. An extensive study about the effects of impurities in the signal for rare gases was performed by P.N.B Neves [31]. In the present system, assembled in the same vacuum line as the previous system, the low conductance (estimated to be inferior to 0.012 l/s) limits the residual vacuum in the chamber volume not to be less than 4.89×10^{-3} Torr. The solution for this residual gas problem would be to increase the diameter of the tubes and to reduce the distance between the DP-IDC and the vacuum pump.

Another limitation is the indirect identification of the ions moving in the gas, which, being indirect, only allows its identification for ions and gases for which cross sections for electron impact, and rate constants and product distributions for collisions between ions and tha gas atoms/molecules are known.

4.5.1 Lamp induced limitations

The range of ion mobility that are possible to be object of measurement can be restricted by the pulse duration (0.5 μs) and by the period between each lamp pulse (0.1 s).

Theoretically, considering a 5 cm drift distance at 15 Td uniform reduced electric field, the minimum reduced mobility possible to be measured is about 0.012 $cm^2V^{-1}s^{-1}$, a limit imposed by the frequency of the flash lamp. However, the ion mobility usually expected for these experimental conditions used is at least one order larger than the one imposed by this lamp limit. On the other hand, the lamp pulse duration limits the maximum mobility to about 2481 $cm^2V^{-1}s^{-1}$. No ion mobility measured in this system is expected to be that high, however electron mobility is about 1000 times higher than ion mobility [7], and they would be expected to be found near the trigger of the mobility spectrum.

As will be shown later in Section 4.6, it was found that the trigger peak width, in this new assembly, was about 200 times greater than it was supposed to, which limits the maximum mobility possible to be measured to be about 12.4 $cm^2V^{-1}s^{-1}$.

4.5.2 Electric potential simulation

With the purpose of understanding the characteristics of the electric field inside the DP-IDC, a simulation was performed in MATLAB® at conditions similar to those in which it is expected to work: a E/N of 20 Td, a total pressure of about 8 Torr at room temperature (which gives an ideal uniform electric field of about 57 V/cm inside the drift chamber). A V_{GEM} of 25 V, a voltage difference of 30 V applied between the grids of the double grid and a grounded detector body were considered. In order to simplify the problem, a cylindrical symmetry was considered. Although, the GEM base is a square geometry (15×15 mm), it was assumed to be circular with the same area as that of the real one, i.e. with $r_{GEM} \approx$ 8.5mm. The simulation ran until a maximum difference between iterations of 10^{-6} V was achieved.

There may be some differences between the results of these simulations and what in fact happens inside the chamber since there are number of aspects that in fact may differ: the GEM geometry and so its impact on the field, the electrical contacts positions, the distances between the rings of the field cage may not be as well defined and electrical resistances present some deviation from their nominal values, inducing effects on the uniformity of the field.

The results of these simulations for when only the top part is biased and with the detector fully biased are presented in Figures 4.9 and 4.10, respectively.

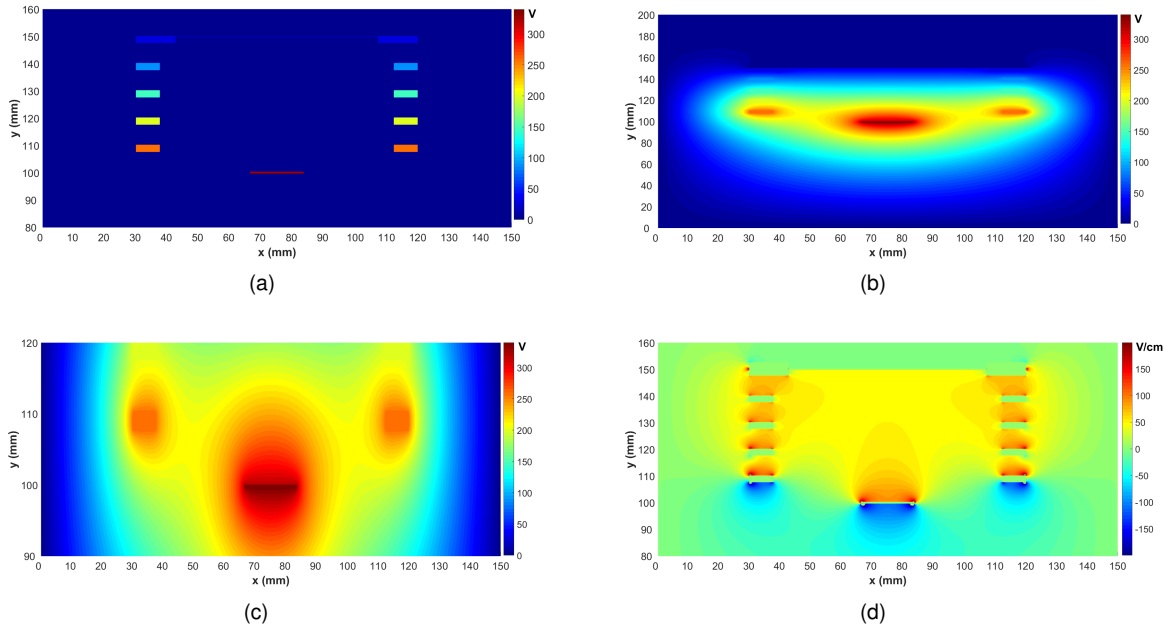

Figure 4.9: Results of the calculations on the electric field inside the detector when only the top part of the chamber is biased: (a) initial electrical potential, (b) and (c) equipotential lines inside the chamber and near the GEM, respectively, and (d) electric fields in the vertical direction.

In order to perform high accuracy ion mobility measurements, a uniform electric field is required. However, as can be seen in Figure 4.9, when only the top part of the detector is functioning, corresponding to a positive ion mobility experiment, the electric field inside the detector is far from uniform. Near the GEM, where the primary ions are produced and begin their journey through the drift chamber, up to the first field cage ring, the vertical electric field (E_y) is higher than 75 V/cm and it changes quickly in both vertical (y) and radial (x) directions. A similar effect happens near the field rings and the electric field stabilizes after the third ring for the circular region delimited by half of the radius of the drift cage. Nonetheless the electric field obtained is about 13$\%$ lower than the ideal one (57 V/cm). However, if the system is biased in both sides, as can be seen in Figure 4.10, this problem is substantially reduced.

A simulation on the drift of ions with an arbitrary mobility inside the drift region of the detector was then performed considering no diffusion effects or a simplified model which only considers effects of longitudinal thermal diffusion for a typical ion drifting in a gas (in this case Ar^+ ions in pure Ar) at 8 Torr pressure. The purpose of this simulation is just to give a clue of the ion track patterns inside the drift chamber with and without diffusion in both biasing modes. The ion tracks inside the drift chamber when only the top part of the detector is biased without and with the diffusion model applied, and when the

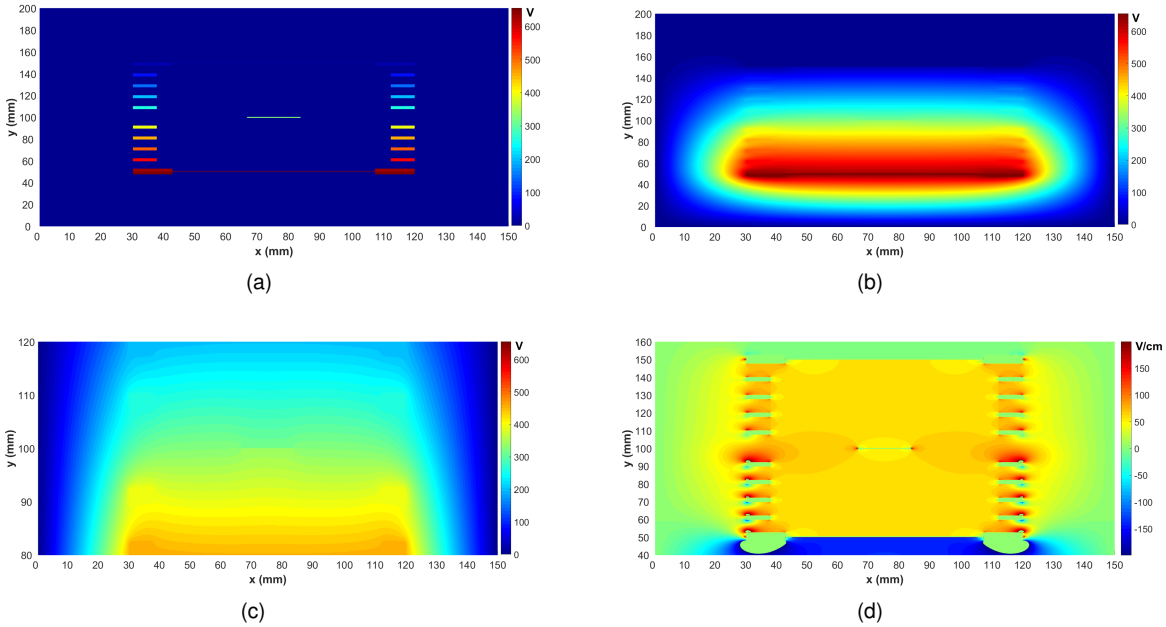

Figure 4.10: Results of the calculations on the electric field inside the detector when both top and bottom parts of the chamber are biased: (a) initial electrical potential, (b) and (c) equipotential lines inside the chamber and near the GEM, respectively, and (d) electric fields in the vertical direction.

system is operating fully (with the diffusion applied) are presented in Figure 4.11.

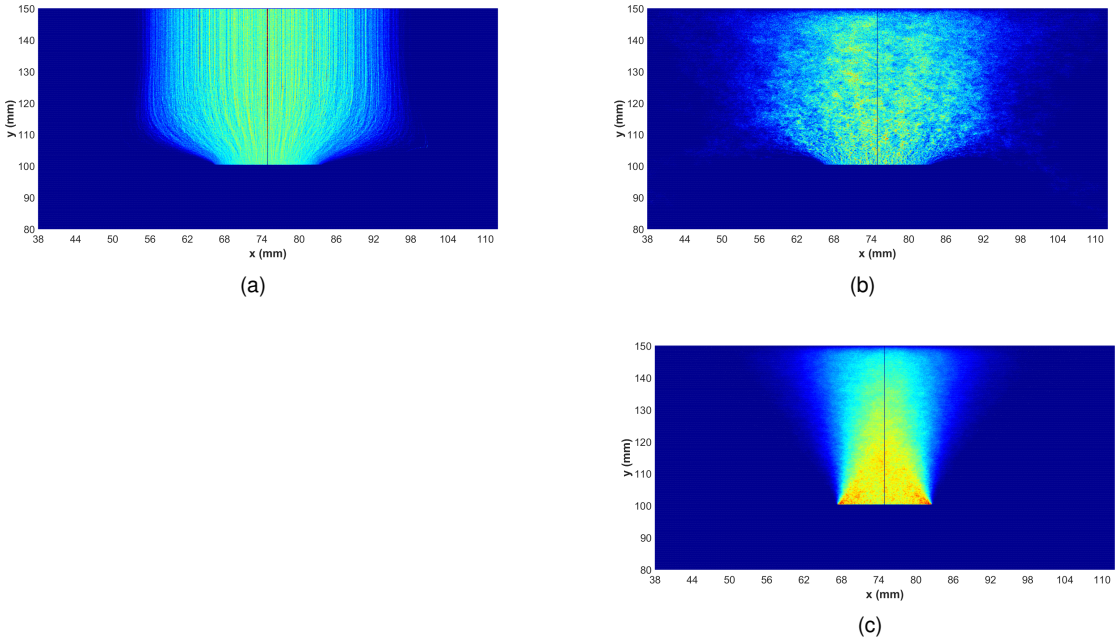

Figure 4.11: Ion tracks inside the drift chamber when on only the top part is biased without (a) and with (b) a simplified model for diffusion effects, and with both the chambers biased and a simplified diffusion model applied (c).

Also, by computing the relative time required for ions to drift from the GEM surface up to the double grid structure, it was found that ions should take about 23% longer to finish their drift in the calculated field case than in an ideal 57 V/cm uniform electric field when only the top part of the experiment is biased, and about 2% longer when the system is operating in a fully biased model. It is important to

note that the diffusion with be about 95 times higher than in a system at atmospheric pressure, since the diffusion coefficient is inversely proportional to pressure.

When only one of the parts is biased, these high thermal longitudinal diffusion effects combined with the high radial electric fields variations far from the GEM center causes some ions to drift through the lower part or the sides of the drift chamber, which should result in less ions reaching the double grid and thus a lower amplitude of the signal obtained. On the other hand, when the system is fully biased, no considerable signal loss due to these effects is expected.

At last, no significant variation in the drift time was found between the models with diffusion and no diffusion at all in either of the biasing models.

4.5.3 Teflon spacers induced limitations

Teflon is a very good electrical insulator and that why it was chosen to be the material of which the spacers were made. However mean thermal expansion of Teflon [80], at 293$\pm$10 K, is at least ten times greater than for various types of steel [81] and thermal expansion coefficients at a given temperature vary a lot in that range of temperatures, between about 110$\times 10^{-6}$ and 520$\times 10^{-6}$ K^{-1} which can lead to variations on the ion drift distance of the order of 0.1 mm.

4.6 First results on the mobility of positive ions

In order to test the detector, some measurements of positive ion mobility (biasing the top part of the detector) were taken for pure CF_4 and N_2 for different reduced electric field ranging from 10 to 30 Td, a V_{GEM} of 25 and 35 V, 8 Torr of total pressure at room temperature (293 K). The time-of-arrival spectra in pure CF_4 and pure N_2 for a V_{GEM} of 35V, a E/N of 30 Td and 8 Torr of total pressure at room temperature, as well as the electric background recorded after each measurement, are presented in Figure 4.12. These gases were chosen for the tests because of both their availability and by their known lower ion mobility than the upper limit of the mobility possible to be measured with this detector, due to the limitation already referred in Section 4.5.1.

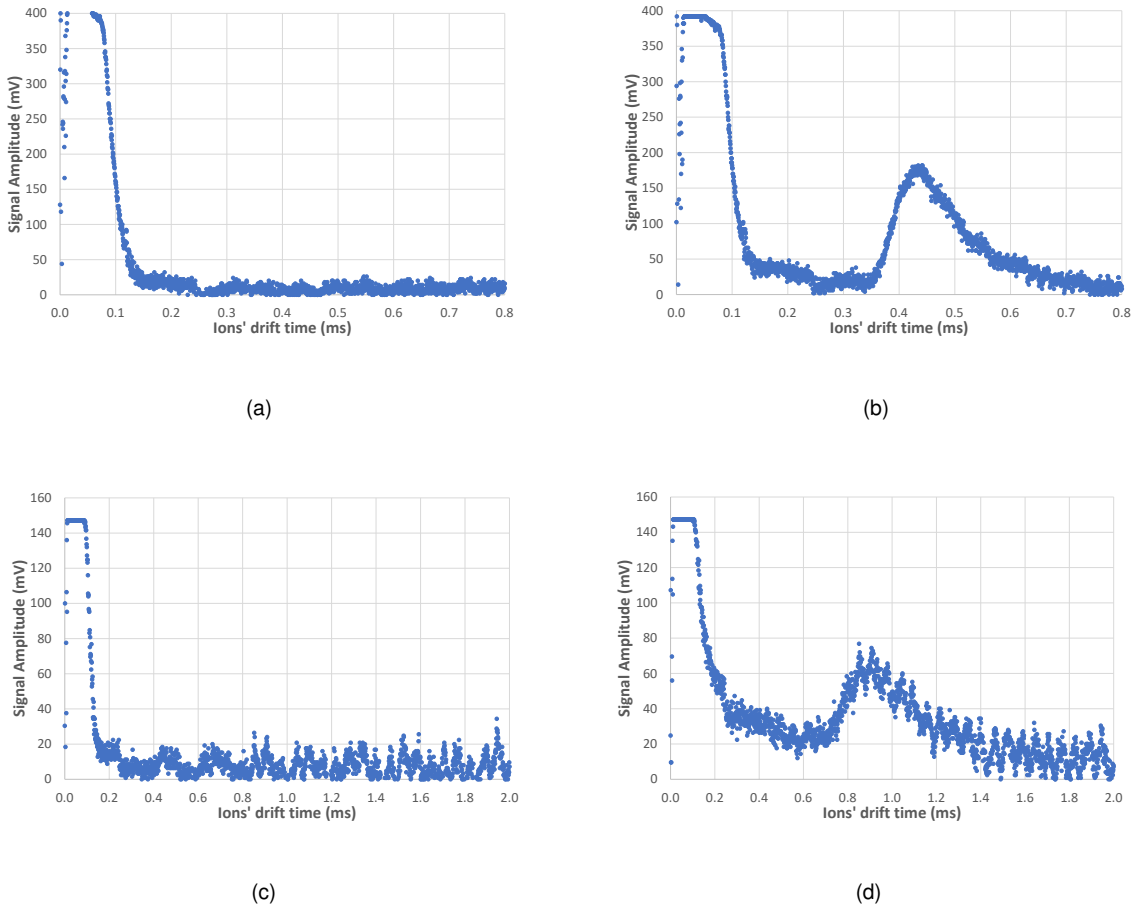

Figure 4.12: Time-of-arrival spectra (average of 128 pulse) recorded with the DP-IDC for a total pressure of 8 Torr, reduced electric field of 30 Td, V_{GEM} of 35 V at room temperature (293K) in pure N_2 (b) and in pure CF_4 (d). The corresponding electric backgrounds recorded after each measurement are also presented in (a) and (c).

Considering the background measurements, for example the ones presented in Figures 4.12(a) and 4.12(b), it was found that the system presented a much higher electrical noise than expected, with about 6 to 10 mV deviation from the baseline voltage of the background, and also that the trigger peak, which is due to the Xe lamp pulse duration, has a width at half maximum of about 0.1 ms, which is 200 times greater than expected. Also, as time went on, we noticed that the noise frequency and amplitude were

not stable, and that the trigger signal from the lamp would vary abruptly and randomly. It is expected that these noise problems can be reduced by reducing the length of the cables between the pre-amplifier and the collection feedthrough and by insuring a stable and single ground across the detector. These electronic noise and variations on the amplitude of the lamp output represent a big problem for the stability of operations with this prototype.

When taking the first measurements, it was found no noticeable signal for a V_{GEM} of 25 V and for E/N lower than 30 Td, or for V_{GEM} of 35 V and E/N lower than 20 Td in both pure CF_4 and pure N_2.

As expected from the results presented in Section 3.2.1, only one peak is clearly visible for a V_{GEM} of 35 V and E/N of 30 Td in both pure CF_4 and pure N_2 that should be due to CF_3^+ and N_4^+ ions, respectively, as can be seen in Figures 4.12(b) and 4.12(d). However,in both spectra, two peaks are clearly visible at the left of the central one with lower amplitude (one with about 20 mV and another with about 10 mV). Also, at the right, a long tail is visible in both spectra. The experimental ion mobilities obtained for some measurements in pure CF_4 and pure N_2 for 8 Torr of total pressure at room temperature and at different conditions of V_{GEM} and of E/N are presented in Table 4.1, as well as some results obtained with the previous system for these pure gases, performed at our group.

Table 4.1: First results on experimental measurements of the mobility of positive ions in pure CF_4 and N_2, using the top drift chamber of the detector, for a total pressure of about 8 Torr at room temperature. Experimental results from previous work in the some gases ([33] in pure N_2 and [46, 47] in pure CF_4) are also presented in the last column.

Gas	V_{GEM} (V)	E/N (Td)	Experimental Mobility	Previous work
CF_4	35	30	0.654±0.001	1.072±0.006
N_2	35	20	1.36±0.06	2.37±0.01
N_2	25	25	1.32±0.06	2.36±0.01
N_2	35	30	1.43±0.06	2.36±0.01

As can be seen in Table 4.1 and in Figure 4.12, the system should be capable of good precision since the statistical errors are low, but of low accuracy, since the mobilities obtained are about 40% lower than the ones found previously [33, 46, 47]. We believe that this happens both because the high width of the lamp pulse and because of the non-uniformity of the electric field inside the drift chamber when only the top part is biased, where the effect of the residual vacuum on the mobility measured can not be discarded. We expect that operating the detector on both sides will greatly improve its accuracy.

Still, the results presented here are insufficient to characterize the detector, since few measurements were made with the top part of the detector and none with detector fully biased (top and bottom) due to time constraints and technical problems with the amplifier circuit.

Chapter 5

Conclusions

Ion mobility measurements are of great importance in several areas ranging from physics to chemistry. The knowledge of the transport properties in gases is essential in the development and improvement of technologies based on IMS, and gaseous radiation detectors as TPCs, NITPCs and MWPCs.

The transport properties of ions in mixtures of various gases are influenced by phenomena such as diffusion, charge transfer and electron attachment reactions, cluster formation and recombination. The knowledge of both the cross sections for electron impact ionization and of the rate constants and product distributions of the reactions between ions and the gas atoms/molecules is essential not only in the identification of the ions responsible for the time-of-arrival spectra obtained, but also in the interpretation of the results obtained. Additionally, predictions of the ion mobility on mixtures can be made for low E/N, low pressure and room temperature by using the Langevin formula and Blanc's law.

Thus, in the first part of this work, the techniques and system described in [31] were used to study ion mobility in pure isobutane, in mixtures of Ar with molecular gases (N_2, CF_4 and iso-C_4H_{10}) and of CF_4 with alkanes (CH_4, C_2H_6 and iso-C_4H_{10}), and finally in ternary mixtures for the ILC experiment.

Regarding pure isobutane, two peaks were observed across the range of reduced electric fields from 10 to 40 Td. The ions responsible for the peaks were found to be the $C_8H_n^+$ ions, for the peak with higher mobility, and the $C_{12}H_n^+$ ions, for the peak with lower mobility, and their reduced mobilities to be 0.65$\pm$0.01 and 0.60$\pm$0.01 $cm^2 \cdot V^{-1} \cdot s^{-1}$, respectively, when $E/N \rightarrow 0$. However, it is important to note that the experimental values present a deviation within about 20$\%$ the ones obtained from Langevin theory, due to the limitations of this theory to predict the mobility of large molecular ions, as discussed in [20].

In the binary mixtures of Ar with other molecular gases studied, increasing Ar concentration leads to greater signal amplitude and faster ions in mixtures with CF_4 and iso-C_4H_{10}, and slower ions in mixtures with N_2. This effect is related to the fact that the mobility of a certain ions is inversely proportional to the square root of the product between the reduced mass (μ) of the complex ion-atom/molecule and the polarizability (α) of the gas atoms/molecules.

In mixtures involving Ar–CF_4 and Ar–iso-C_4H_{10}, we have learned that all charge is eventually transfered to the molecular gases, thus the ions responsible could be the same ones identified in the studies

on the pure molecular gases. While this is true for the Ar–CF_4 mixtures studied, where CF_3^+ is the ion responsible for the single peak, in the Ar–iso-C_4H_{10} mixtures, the reactions between ions and gas molecules are completed during the ions' drift time, and so both the fraction and species of the ions arriving at the collecting grid will be different.

Additionally, in the Ar–N_2 mixtures, the ion responsible for the only peak obtained is thought to be the ArN_2^+ ion, which displays a relatively stable mobility for most of the mixtures studied. This behavior is related to the fact that the product between the reduced mass (μ), of the ArN_2^+ with both Ar and N_2, and the neutral polarizability (α) is similar, resulting in an approximately constant mobility in the range from 10% to 90% Ar.

In the binary mixtures of CF_4 with CH_4, C_2H_6 and iso-C_4H_{10}, as we increase the carbon content of the alkane in the mixture, ions will move slower, with the number and origin of the peaks changes due to the reactions and mass of the addictive involved. Also, increasing CF_4 concentration leads to lower signal amplitudes and slower ions in the mixtures with CH_4 and C_2H_6 or faster ions in the CF_4–iso-C_4H_{10} mixtures, again for the same reasons presented earlier.

Finally, in the three alternative mixtures for the ILC collaboration: three peaks were observed for the mixtures containing CH_4 and iso-C_4H_{10}, and two with a long tail for the mixture containing C_2H_6. In these cases, the experimental results presented a theoretical deviation below 6%, except for the peaks identified as $C_3H_n^+$ ions, which mobility seems to be influenced by the predecessor ions.

In gaseous radiation detectors working at high pressure (near atmospheric), the distribution of the final ions may slightly differ from the results obtained at our working pressure/ drift distance. However these accurate ion mobility measurements have been consistently in accordance with the ones obtained at higher pressures [20]. For high pressure systems, two peaks are expected for the mixtures containing CH_4 and C_2H_6, while only one for the mixture containing iso-C_4H_{10}. In the Ar–CF_4–CH_4 (92-3-5) mixture, the ions responsible for the peaks should be CF_3^+, for the peak with lower mobility, and $C_3H_n^+$, for the peak with higher mobility, as the reactions involved should be completed. In the Ar–CF_4–C_2H_6 (94-3-3) mixture, the ions responsible for the peaks should be of $C_4H_n^+$, for the peak with lower mobility, and $C_3H_n^+$, for the peak with higher mobility, with the same long tail, as previously mentioned. As discussed earlier, the mobilities obtained in this work should be close to the ones in higher pressure systems, except for the $C_3H_n^+$ ions where the validity of our results is limited by the fact that in our work, the mobility obtained for these ions seems affected by their drift as predecessor ions. In the Ar–CF_4–iso-C_4H_{10} (95-3-2) mixture, the ions responsible for the peak should be $C_{12}H_n^+$. Unfortunately, the mobility of these ions could not be measured because the drift time required for their formation in our working pressures (6 to 10 Torr) is much longer than the drift time allowed at the current configuration of this system. As for the choice of the relative concentration in the ternary mixtures, although somehow limited, these results are presented as a direct request from the scientific community, in particular the LCTPC collaboration.

In what concerns the new system, the DP-IDC has been designed, constructed, assembled and preliminarily tested successfully. Despite the poor accuracy of the results when only the top part of the system is biased, the system is precise enough to distinguish between ions with different mobilities.

Although no tests were made with the detector operating with both top and bottom parts biased simultaneously, it is expected, from the results of a simulation performed, that the detector will be much more accurate when operating in the dual polarity mode (biasing both parts of the detector), as the uniformity of the electric inside the drift chambers should be dramatically improved. The proof of concept was made, but in order to adequately operate the chamber, several problems should be addressed.

5.1 Improvements on the DP-IDC

Since one of the major limitations of this system is the non-uniformity of the electric field inside the drift chamber, a GEM of greater area or a new GEM support should be installed on the GEM base, in order to ensure electric field uniformity when the detector is working with only one of the drift chambers biased. This can be done either by evaporation of a metallic film on the surface of the Teflon base, or by carving two cavities in the GEM support, in order to add one field at the top of the base and another in the bottom, which will be biased at the same voltage as the top and the bottom electrodes of the GEM. Another way to minimize this problem is to completely remove the present GEM support prototype and substitute it by a new prototype composed of two metallic cylindric parts, separated from each other by a Kapton foil, in a similar way as the second double grid prototype, presented in Chapter 4.

In Figure 5.1, a proposal for a new GEM support design is presented. In this proposal, the GEM is placed in-between two stainless steel discs, that insure both electric wire contact with the GEM electrodes and uniformity of the electric field in the chamber. In order to electrically isolate the GEM electrodes a Kapton foil disk should be introduced between the disks. The disks are supported by a Teflon structure fixed to the detector body. Also, as in the previous prototype, several holes in the Teflon should be drilled in order to allow free flowing of the gases inside the chamber.

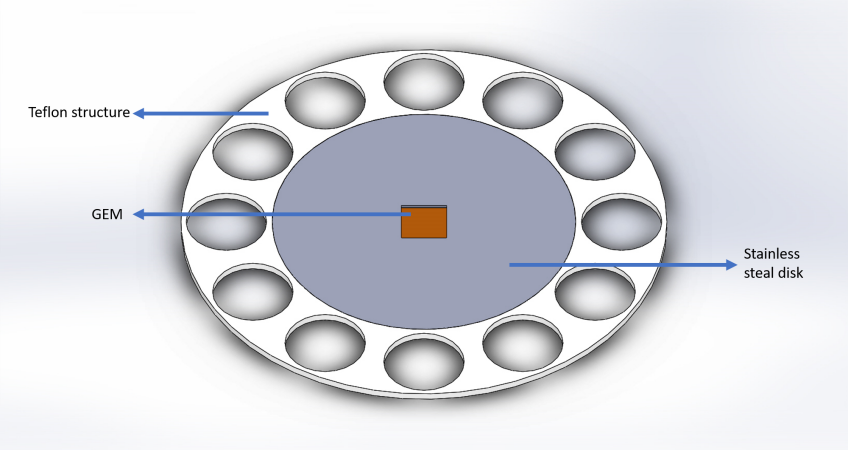

Figure 5.1: Redesign proposal for the new GEM base. The GEM is placed in-between two stainless steel discs, electrically isolated through Kapton foil, which are supported in a Teflon structure.

Secondly, the Teflon spacers should be removed and traded by another good electrical insulator also with low outgassing but with lower thermal expansion, e.g. Macor, to reduce the uncertainty on the drift distances on both sides of the chamber.

At the present time, the DP-IDC can be operated separately and the ion mobility of positive and negative ions can be measured at the top and bottom drift chambers, respectively, by grounding the collecting grids for each corresponding drift chamber. But in order to measure ion mobility of both kinds of ions simultaneously, it is not possible to ground both collecting grids and thus an electronic circuit for the pre-amplifier allows to work at a the high voltage baseline has to be designed or a commercial option has to be considered and acquired.

5.2 Future work

As gas-filled detectors continue to be extensively used in radiation detections and measurements, understanding the ion transport properties in mixtures of gases will supply important information to improve their performance, as we did in this work for the LCTPC. With the positive ion mobility experiment, we suggest to pursue the investigation on the mobility of ions in different gas mixtures of interest such as:

- **Ne - CF_4**
- **Ne - iC_4H_{10}**
- **Xe - iC_4H_{10}**

Additionally, with the DP-IDC, the transport properties of negative ions in pure and in mixtures with electronegative gases will be performed since NITPCs are serious contenders for rare events physics such as dark matter and neutrinoless beta decay ($0\nu\beta\beta$) searches. With this in mind, as a suggestion, the mobility of ions may be studied in several gases and mixtures of gases of possible interest, as:

- **SF_6**
- **CS_2**
- **O_2**
- **N_2O**
- **CH_3NO_2**
- **SF_6 - CH_4**
- **SF_6 - C_2H_6**
- **CS_2 - CH_4**
- **CS_2 - C_2H_6**
- **Xe - SF_6**
- **Xe - CS_2**
- **CO_2 - CH_3NO_2**

- **Ne - CO_2 - CH_3NO_2**

Finally, when all the constraints are raised or a new prototype designed, it will be possible to study rate constant influence on ion mobility and to study the mobility of lighter ions with minor modification. In addition to the study of the mobility on negative ions, this system will allow to study the effect of impurities, like O_2, in the amplitude of the signal. Also, it may be possible to perform relative measurements of ion diffusion by studying the width of the time-of-arrival spectra obtained for different drift distances.

Bibliography

[1] E. A. Mason and E. W. Mcdaniel. *Transport Properties of Ions in Gases*. 1988. John Wiley and Sons, Inc. New York.

[2] S. Armenta and M. B. Manel Alcala. A review of recent, unconventional applications of ion mobility spectrometry (IMS). *Analytica Chimica Acta*, 703(2):114 – 123, 2011. URL http://www.sciencedirect.com/science/article/pii/S0003267011009627.

[3] (a) D. Nygren, PEP-198 (1975); (b) 1976 Proposal for a PEP Facility based on the TPC, PEP4, December 30. .

[4] H. J. Hilke. Time projection chambers. *Rep. Prog. Phys.*, 73(11):116201, 2010. URL http://stacks.iop.org/0034-4885/73/i=11/a=116201.

[5] L. Arazi. On the possibility of positive-ion detection in gaseous TPCs and its potential use for neutrinoless double beta decay searches in ^{136} Xe. *J. Phys. Conf. Series*, 1029(1):012004, 2018. URL http://stacks.iop.org/1742-6596/1029/i=1/a=012004.

[6] LCTPC Collaboration, . URL https://www.lctpc.org/e8/e57671. Last visited: 13/09/2017.

[7] G. E. Knoll. *Radiation Detection and Measurement*. Third edition, 2000. John Wiley and Sons, Inc. New York.

[8] F. Böhmer, M. Ball, S. Dørheim, C. Höppner, B. Ketzer, I. Konorov, S. Neubert, S. Paul, J. Rauch, and M. Vandenbroucke. Simulation of space-charge effects in an ungated GEM-based TPC. *Nucl. Inst. and Meth. Phys. A.*, 719:101 – 108, 2013. ISSN 0168-9002. URL http://www.sciencedirect.com/science/article/pii/S0168900213004166.

[9] J. Alme et al. The ALICE TPC, a large 3-dimensional tracking device with fast readout for ultra-high multiplicity events. *Nucl. Inst. and Meth. Phys. A.*, 622(1):316 – 367, 2010. ISSN 0168-9002. doi: https://doi.org/10.1016/j.nima.2010.04.042. URL http://www.sciencedirect.com/science/article/pii/S0168900210008910.

[10] M. Ball, K. Eckstein, and T. Gunji. Ion backflow studies for the ALICE TPC upgrade with GEMs. *J. Inst.*, 9(04):C04025, 2014. URL http://stacks.iop.org/1748-0221/9/i=04/a=C04025.

[11] D. Attié. TPC review. *Nucl. Inst. Meth. Phys. A.*, 598(1):89 – 93, 2009. URL http://www.sciencedirect.com/science/article/pii/S0168900208011996.

[12] TPC R&D for an ILC detector. 2007. Status Report from the LCTPC Collaboration.

[13] F. Sauli. *Gaseous Radiation Detectors: Fundamentals and Applications*. 2014. Cambridge Monographs on Particle Physics, Nuclear Physics and Cosmology, Cambridge University Press.

[14] D. Attié et al. A time projection chamber with GEM-based readout. *Nucl. Inst. and Meth. Phys. A.*, 856:109 – 118, 2017. URL http://www.sciencedirect.com/science/article/pii/S0168900216311226.

[15] C. Martoff, D. Snowden-Ifft, T. Ohnuki, N. Spooner, and M. Lehner. Suppressing drift chamber diffusion without magnetic field. *Nucl. Inst. and Meth. Phys. A.*, 440(2):355 – 359, 2000. URL http://www.sciencedirect.com/science/article/pii/S0168900299009559.

[16] D. P. Snowden-Ifft, C. J. Martoff, and J. M. Burwell. Low pressure negative ion time projection chamber for dark matter search. *Phys. Rev. D*, 61(10), 2000. URL https://doi.org/10.1103%2Fphysrevd.61.101301.

[17] J. B. R. Battat et al. First background-free limit from a directional dark matter experiment: Results from a fully fiducialised DRIFT detector. *Phys. of the Dark Universe*, 9-10:1 – 7, 2015. ISSN 2212-6864. URL http://www.sciencedirect.com/science/article/pii/S2212686415000084.

[18] D. R. Nygren. A negative-ion TPC with ultra-high energy resolution for 0-ν double beta decay search in ^{136}Xe. *J. Phys. Conf. Series*, 65(1):012003, 2007. URL http://stacks.iop.org/1742-6596/65/i=1/a=012003.

[19] Z. R. Prieskorn, J. E. Hill, P. E. Kaaret, and J. K. Black. Photoelectron Track Length Distributions Measured in a Negative Ion Time Projection Chamber. *IEEE Trans. Nucl. Sci.*, 61(2):894–900, 2014.

[20] Y. Kalkan, M. Arslandok, A. Cortez, Y. Kaya, T. Nayak, and R. Veenhof. Cluster ions in gas-based detectors. *J. Inst.*, 10(07):P07004, 2015. URL http://stacks.iop.org/1748-0221/10/i=07/a=P07004.

[21] C. Dass. *Fundamentals contemporary mass spectrometry*. First edition, 2007. John Wiley and Sons, Inc. New York.

[22] P. N. B. Neves, A. N. C. Garcia, A. M. F. Trindade, J. A. S. Barata, L. M. N. Tavora, and C. A. N. Conde. Experimental measurement of the Ne^+ and Ne_2^+ ion mobility in Ne and the the reaction rate coefficient for $Ne^+ + 2Ne \rightarrow Ne_2^+ + Ne$. *IEEE Trans. Nucl. Sci.*, 58(4):2060–2063, Aug 2011.

[23] L. A. Posey and M. A. Johnson. Pulsed photoelectron spectroscopy of negative cluster ions: Isolation of three distinguishable forms of $N_2O_2^-$. *J. Chem. Phys.*, 88(9):5383–5395, 1988. URL https://doi.org/10.1063/1.454576.

[24] P. Langevin. Une formule fondamentale de theorie cinetique. *Annal. Chim. Phys.*, 5:245, 1905.

[25] R. R. Teachout and R. T. Pack. The static dipole polarizabilities of all the neutral atoms in their ground states. *Atomic Data and Nucl. Data Tables*, 3:195 – 214, 1971. URL http://www.sciencedirect.com/science/article/pii/S0092640X71800074.

[26] A. B. Tipton, A. P. Deam, and J. E. Boggs. Atomic Polarization of Sulfur Hexafluoride and of Carbon Tetrafluoride. *J. Chem. Phys.*, 40(4):1144–1147, 1964.

[27] J. Hirschfelder, C. Curtis, and R. Bird. *Molecular Theory of Gases and Liquids*. 1954. Fundamental information on molecular polarizabilities, John Wiley and Son, Inc. New York.

[28] K. M. Gough, M. M. Yacowar, R. H. Cleve, and J. R. Dwyer. Analysis of molecular polarizabilities and polarizability derivatives in H_2, N_2, F_2, CO, and HF, with the theory of atoms in molecules. *Canadian J. Chem.*, 74(6):1139–1144, 1996. URL https://doi.org/10.1139/v96-128.

[29] A. Blanc. Recherches sur le mobilities des ions danz le gaz. *J. Appl. Psys.*, 7:825, 1908.

[30] R. Chang. *Chemistry*. 10^{th} edition, 2010. McGraw-Hill.

[31] P. Neves. *Studies on the mobility of monoatomic and dimer noble gas ions in their parent gases*. 2009. PhD thesis, Universidade de Coimbra.

[32] P. N. B. Neves, C. A. N. Conde, and L. M. N. Távora. Experimental measurement of the mobilities of atomic and dimer Ar, Kr, and Xe ions in their parent gases. *J. Chem. Phys.*, 133(12):124316, 2010. URL https://doi.org/10.1063/1.3497651.

[33] A. N. C. Garcia, P. N. B. Neves, A. M. F. Trindade, F. P. Santos, and C. A. N. Conde. A new contribution to the experimental measurement of the N_4^+ ion mobility in N_2 at 298K. *J. Inst.*, 7(02): P02012, 2012. URL http://stacks.iop.org/1748-0221/7/i=02/a=P02012.

[34] A. F. V. Cortez, A. N. C. Garcia, P. N. B. Neves, F. P. Santos, F. I. G. M. Borges, J. A. S. Barata, and C. A. N. Conde. Experimental measurement of the mobility of ions originated in ethane in their parent gas. *J. Inst.*, 8(07):P07013, 2013. URL http://stacks.iop.org/1748-0221/8/i=07/a=P07013.

[35] A. F. V. Cortez, A. N. C. Garcia, P. N. B. Neves, F. P. Santos, F. I. G. M. Borges, J. A. S. Barata, and C. A. N. Conde. Experimental ion mobility measurements in Ar-C_2H_6 mixtures. *J. Inst.*, 8(12): P12012, 2013. URL http://stacks.iop.org/1748-0221/8/i=12/a=P12012.

[36] A. M. F. Trindade, J. Escada, P. N. B. Neves, T. H. V. T. Dias, J. A. S. Barata, F. P. Santos, and C. A. N. Conde. Experimental measurements of the mobility of methane ions in methane. *J. Inst.*, 7(06):P06010, 2012. URL http://stacks.iop.org/1748-0221/7/i=06/a=P06010.

[37] A. N. C. Garcia, P. N. B. Neves, A. M. F. Trindade, A. F. V. Cortez, F. P. Santos, and C. A. N. Conde. Experimental ion mobility measurements in Xe-N_2 mixtures. *J. Inst.*, 9(07):P07008, 2014. URL http://stacks.iop.org/1748-0221/9/i=07/a=P07008.

[38] A. M. F. Trindade, A. F. V. Cortez, P. N. B. Neves, A. N. C. Garcia, J. Escada, F. P. Santos, F. I. G. M. Borges, J. A. S. Barata, and C. A. N. Conde. Experimental study on ion mobility in Ar-CH_4 mixtures. *J. Inst.*, 9(06):P06003, 2014. URL http://stacks.iop.org/1748-0221/9/i=06/a=P06003.

[39] P. M. C. C. Encarnação, A. F. V. Cortez, M. G. A. Pinto, P. N. B. Neves, A. M. F. Trindade, J. Escada, F. P. Santos, F. I. G. M. Borges, J. A. S. Barata, and C. A. N. Conde. Experimental ion mobility measurements in Ar-CO_2 mixtures. *J. Inst.*, 10(01):P01010, 2015. URL http://stacks.iop.org/1748-0221/10/i=01/a=P01010.

[40] P. Encarnação, A. Cortez, R. Veenhof, P. Neves, F. Santos, A. Trindade, F. Borges, and C. Conde. Experimental Ion Mobility measurements in Ne-CO_2 and CO_2-N_2 mixtures. *J. Inst.*, 11(05):P05005, 2016. URL http://stacks.iop.org/1748-0221/11/i=05/a=P05005.

[41] A. Cortez, P. Encarnação, R. Veenhof, P. Neves, F. Santos, F. Borges, and C. Conde. Experimental ion mobility measurements in Ne-N_2. *J. Inst.*, 11(11):P11019, 2016. URL http://stacks.iop.org/1748-0221/11/i=11/a=P11019.

[42] A. Cortez, M. Santos, R. Veenhof, R. Patra, P. Neves, F. Santos, F. Borges, and C. Conde. Experimental ion mobility measurements in Xe-CO_2. *J. Inst.*, 12(06):P06012, 2017. URL http://stacks.iop.org/1748-0221/12/i=06/a=P06012.

[43] A. Trindade, P. Encarnação, J. Escada, A. Cortez, P. Neves, C. Conde, F. Borges, and F. Santos. Experimental studies on ion mobility in xenon-trimethylamine mixtures. *J. Inst.*, 12(07):P07007, 2017. URL http://stacks.iop.org/1748-0221/12/i=07/a=P07007.

[44] J. Perdigoto, A. Cortez, R. Veenhof, P. Neves, F. Santos, F. Borges, and C. Conde. Experimental ion mobility measurements in Xe-CH_4. *J. Inst.*, 12(09):P09003, 2017. URL http://stacks.iop.org/1748-0221/12/i=09/a=P09003.

[45] J. Perdigoto, A. Cortez, R. Veenhof, P. Neves, F. Santos, F. Borges, and C. Conde. Experimental ion mobility measurements in Xe-C_2H_6. *J. Inst.*, 12(10):P10011, 2017. URL http://stacks.iop.org/1748-0221/12/i=10/a=P10011.

[46] A. Cortez, M. Kaja, J. Escada, M. Santos, R. Veenhof, P. Neves, F. Santos, F. Borges, and C. Conde. Experimental ion mobility measurements in Xe-CF_4 mixtures. *J. Inst.*, 13(04):P04006, 2018. URL http://stacks.iop.org/1748-0221/13/i=04/a=P04006.

[47] M. Santos, M. Kaja, A. Cortez, R. Veenhof, P. Neves, F. Santos, F. Borges, and C. Conde. Experimental ion mobility measurements for the LCTPC collaboration—Ar-CF_4 mixtures. *J. Inst.*, 13(04):P04012, 2018. URL http://stacks.iop.org/1748-0221/13/i=04/a=P04012.

[48] LCTPC Collaboration. URL https://www.lctpc.org/e8/e46/e47/. Last visited: 13/09/2018.

[49] F. Sauli. GEM: A new concept for electron amplification in gas detectors. *Nucl. Inst. and Meth. Phys. A.*, 386(2):531 – 534, 1997. URL http://www.sciencedirect.com/science/article/pii/S0168900296011722.

[50] R. Rejoub, B. G. Lindsay, and R. F. Stebbings. Determination of the absolute partial and total cross sections for electron-impact ionization of the rare gases. *Phys. Rev. A*, 65(4):042713, 2002.

[51] B. Gstir et al. Electron impact multiple ionization of neon, argon and xenon atoms close to threshold: appearance energies and Wannier exponents. *J. Phys. B.*, 35(13):2993, 2002. URL http://stacks.iop.org/0953-4075/35/i=13/a=312.

[52] K. Hiraoka and T. Mori. Formation and stabilities of cluster ions Ar_n^+. *J. Chem. Phys.*, 90(12): 7143–7149, Jun 1989. URL https://doi.org/10.1063%2F1.456245.

[53] I. Torres, R. Martínez, and F. Castaño. Electron-impact dissociative ionization of fluoromethanes CHF_3 and CF_4. *J. Phys. B.*, 35(11):2423, 2002. URL http://stacks.iop.org/0953-4075/35/i=11/a=302.

[54] V. Stojanović, Z. Raspopović, J. V. Jovanović, J. de Urquijo, and Z. L. Petrović. Mobility of positive ions in CF_4. *J. Phys. Conf. Series*, 514(1):012059, 2014. URL http://stacks.iop.org/1742-6596/514/i=1/a=012059.

[55] J. de Urquijo, E. Basurto, and J. Hernández-Ávila. *Electron Mobility and Effective Ionization Coefficients in SF_6-CO_2 Mixtures.* 2001. Springer, Boston, MA.

[56] *National Institute of Standards and Technology, Gaithersburg, Maryland, 20899-8320*. URL http://webbook.nist.gov/cgi/cbook.cgi?ID=C75730&Mask=1EFF. Last visited 12/07/2018.

[57] T. Fiegele, G. Hanel, I. Torres, M. Lezius, and T. D. Märk. Threshold electron impact ionization of carbon tetrafluoride, trifluoromethane, methane and propane. *J. Phys. B.*, 33(20):4263, 2000. URL http://stacks.iop.org/0953-4075/33/i=20/a=306.

[58] H. C. Straub, D. Lin, B. G. Lindsay, K. A. Smith, and R. F. Stebbings. Absolute partial cross sections for electron-impact ionization of CH_4 from threshold to 1000 eV. *J. Chem. Phys.*, 106(11):4430–4435, 1997. URL https://doi.org/10.1063/1.473468.

[59] P. Mach, J. Urban, T. Märk, et al. Electron impact ionization of C_2H_6: ionization energies and temperature effects. *Inter. J. Mass Spectrosc.*, 235(2):155 – 162, 2004. ISSN 1387-3806. URL http://www.sciencedirect.com/science/article/pii/S1387380604001915.

[60] J. Huntress, W. T. Laboratory studies of bimolecular reactions of positive ions in interstellar clouds, in comets, and in planetary atmospheres of reducing composition. *Astro. J. Sup. Series*, 33:495–514, 1977.

[61] C. Tian and C. R. Vidal. Electron impact dissociative ionization of ethane: Cross sections, appearance potentials, and dissociation pathways. *J. Chem. Phys.*, 109(5):1704–1712, 1998. URL https://doi.org/10.1063/1.476743.

[62] I. Omura. Mass Spectra at Low Ionizing Voltage and Bond Dissociation Energies of Molecular Ions from Hydrocarbons. *Bulletin of the Chem. Society of Japan*, 34(9):1227–1233, 1961. URL https://doi.org/10.1246/bcsj.34.1227.

[63] M. H. F. Bettega, M. A. P. Lima, and L. G. Ferreira. Scattering of low-energy electrons by isomers of C_4H_4. *J. Phys. B.*, 40(15):3015, 2007. URL http://stacks.iop.org/0953-4075/40/i=15/a=003.

[64] C. Q. Jiao, C. A. D. Jr, and A. Garscadden. Electron impact ionization and ion reactions in n-butane. *J. Phys. D: Appl. Phys.*, 40(2):409, 2007. URL http://stacks.iop.org/0022-3727/40/i=2/a=018.

[65] R. Neagu-Plesu, A. H. Jan, and A. G. Harrison. Ion/molecule reactions in isobutane near the ionization threshold. *Rapid Communications in Mass Spectrosc.*, 1(4):63–64. URL https://onlinelibrary.wiley.com/doi/abs/10.1002/rcm.1290010406.

[66] M. S. B. Munson. Effects of structure on the reactions of hydrocarbon ions. *J. Phys. Chem.*, 71(12):3966–3970, 1967. URL https://doi.org/10.1021/j100871a036.

[67] T. Yamashita, H. Kurashige, M. Morii, T. Nakamura, T. Nomura, N. Sasao, K. Shibata, Y. Fukushima, Y. Ikegami, H. Kobayashi, and T. Taniguchi. Measurements of electron drift velocities and positive ion mobilities for gases containing CF_4 II. *Nucl. Inst. and Meth. Phys. A.*, 317(1):213 – 220, 1992. URL http://www.sciencedirect.com/science/article/pii/0168900292906117.

[68] G. Schultz, G. Charpak, and F. Sauli. Mobilities of positive ions in some gas mixtures used in proportional and drift chambers. *Revue de Physique Appliquee*, 1(12):67–70, 1977.

[69] Y. Itikawa. Cross Sections for Electron Collisions with Nitrogen Molecules. *J. Phys. and Chem. Ref. Data*, 35(1):31–53, 2006. URL https://doi.org/10.1063/1.1937426.

[70] P. A. M. van Koppen, M. F. Jarrold, M. T. Bowers, L. M. Bass, and K. R. Jennings. Ion–molecule association reactions: A study of the temperature dependence of the reaction N_2^+ + N2 + M $\rightarrow$ N_4^+ + M for M=N_2, Ne, and He: Experiment and theory. *J. Chem. Phys.*, 81(1):288–297, 1984. URL https://doi.org/10.1063/1.447383.

[71] W. Hack et al. *Gmelin Handbook of Inorganic and Organametallic Chemistry*. 8th edition, 1993. Nitrogen: Supplement Volume B1.

[72] R. Wetzel, F. Baiocchi, T. Hayes, and R. Freund. Absolute cross sections for electron-impact ionization of the rare-gas atoms by the fast-neutral-beam method. *Phys. Rev. A*, 35:559, 1987.

[73] P. B. Armentrout, S. M. Tarr, A. Dori, and R. S. Freund. Electron impact ionization cross section of metastable N_2. *J. Chem. Phys.*, 75(6):2786–2794, 1981. URL https://doi.org/10.1063/1.442350.

[74] E. R. Fisher, M. E. Weber, and P. B. Armentrout. Dissociative charge transfer reactions of Ar^+, Ne^+, and He^+ with CF_4 from thermal to 50 eV. *J. Chem. Phys.*, 92(4):2296–2302, 1990. URL https://doi.org/10.1063/1.457969.

[75] H. Flesch, G.D.; Svec. Fragmentation reactions in the mass spectrometer for C2-C5 alkanes. *J. Chem. Soc. Faraday Trans. 2*, (69):1187, 1973.

[76] M. Tsuji, H. Kouno, K. Matsumura, T. Funatsu, Y. Nishimura, H. Obase, H. Kugishima, and K. Yoshida. Dissociative charge-transfer reactions of Ar^+ with simple aliphatic hydrocarbons at thermal energy. *J. Chem. Phys.*, 98(3):2011–2022, 1993. URL https://doi.org/10.1063/1.464234.

[77] V. G. Anicich. Evaluated Bimolecular Ion-Molecule Gas Phase Kinetics of Positive Ions for Use in Modeling Planetary Atmospheres, Cometary Comae, and Interstellar Clouds. *J. Phys. and Chem. Ref. Data*, 22(6):1469–1569, 1993. URL https://doi.org/10.1063/1.555940.

[78] E. Heckel and R. J. Hanrahan. Ion–molecule reactions in the systems CF_4–CH_4 and CF_4–C_2H_6. *J. Chem. Phys.*, 62(3):1027–1039, 1975. URL https://doi.org/10.1063/1.430570.

[79] W. Harshbarger, M. Robin, and E. Lassettre. The electron impact spectra of the fluoromethanes. *J. Electron Spectrosc. Relat. Phenom.*, 1:319, 1973.

[80] R. K. Kirby. Thermal Expansion of Polytetrafluoroethylene (Teflon) from -190 to +300 C. *J. Research of the National Bureau of Standards*, 57(2):91–94, 1956.

[81] W. Souder and P. Hidnert. Thermal expansion of a few steels. *J. Research of the National Bureau of Standards*, 17:611–626.

Appendix A

Ion mobility data

Table A.1: Mobility of the ions observed in pure iso-C_4H_{10} obtained for E/N between 10 and 45 Td, at room temperature (293 K).

iso-C_4H_{10} E/N (Td)	Mobility ($cm^2 \cdot V^{-1} \cdot s^{-1}$)	Ion
10	0.650 $\pm$ 0.009	$C_8H_n^+$
	0.595 $\pm$ 0.006	$C_{12}H_n^+$
15	0.645 $\pm$ 0.010	$C_8H_n^+$
	0.595 $\pm$ 0.010	$C_{12}H_n^+$
20	0.633 $\pm$ 0.008	$C_8H_n^+$
	0.571 $\pm$ 0.011	$C_{12}H_n^+$
25	0.630 $\pm$ 0.005	$C_8H_n^+$
	0.558 $\pm$ 0.007	$C_{12}H_n^+$
30	0.632 $\pm$ 0.009	$C_8H_n^+$
	0.572 $\pm$ 0.014	$C_{12}H_n^+$
35	0.629 $\pm$ 0.007	$C_8H_n^+$
	0.565 $\pm$ 0.009	$C_{12}H_n^+$
40	0.622 $\pm$ 0.015	$C_8H_n^+$
	0.581 $\pm$ 0.026	$C_{12}H_n^+$
45	0.628 $\pm$ 0.007	$C_8H_n^+$

Table A.2: Reduced mobility of the peaks for the Ar-CF_4 mixture ratios studied, obtained for E/N of 15 Td and of 20 Td, for a pressure of 8 Torr at room temperature (293 K).

Ar-CF_4 Ar $\%$	Mobility at 15 Td ($cm^2 \cdot V^{-1} \cdot s^{-1}$)	Mobility at 20 Td ($cm^2 \cdot V^{-1} \cdot s^{-1}$)	Ion
5	1.159 $\pm$ 0.009	1.139 $\pm$ 0.012	CF_3^+
10	1.191 $\pm$ 0.009	1.179 $\pm$ 0.012	CF_3^+
15	1.228 $\pm$ 0.006	1.220 $\pm$ 0.025	CF_3^+
20	1.271 $\pm$ 0.014	1.251 $\pm$ 0.018	CF_3^+
30	1.356 $\pm$ 0.020	1.330 $\pm$ 0.011	CF_3^+
40	1.458 $\pm$ 0.023	1.434 $\pm$ 0.020	CF_3^+
50	1.509 $\pm$ 0.049	1.482 $\pm$ 0.041	CF_3^+
60	1.599 $\pm$ 0.018	1.579 $\pm$ 0.017	CF_3^+
70	1.731 $\pm$ 0.014	1.714 $\pm$ 0.014	CF_3^+
80	1.924 $\pm$ 0.032	1.908 $\pm$ 0.046	CF_3^+
85	2.000 $\pm$ 0.008	1.977 $\pm$ 0.015	CF_3^+
90	2.120 $\pm$ 0.017	2.085 $\pm$ 0.018	CF_3^+
95	2.234 $\pm$ 0.014	2.188 $\pm$ 0.043	CF_3^+

Table A.3: Reduced mobility of the peaks for the Ar-iC_4H_{10} mixture ratios studied, obtained for E/N of 15 Td and of 20 Td, for a pressure of 8 Torr at room temperature (293 K).

Ar-iC_4H_{10} Ar $\%$	Mobility at 15Td ($cm^2 \cdot V^{-1} \cdot s^{-1}$)	Mobility at 20 Td ($cm^2 \cdot V^{-1} \cdot s^{-1}$)	Ion
5	0.664 $\pm$ 0.007	0.655 $\pm$ 0.003	$C_8H_n^+$
	0.606 $\pm$ 0.017	0.599 $\pm$ 0.013	$C_{12}H_n^+$
10	0.681 $\pm$ 0.005	0.678 $\pm$ 0.001	$C_8H_n^+$
	0.598 $\pm$ 0.015	0.608 $\pm$ 0.005	$C_{12}H_n^+$
15	0.714 $\pm$ 0.006	0.704 $\pm$ 0.003	$C_8H_n^+$
	0.660 $\pm$ 0.0085	0.630 $\pm$ 0.025	$C_{12}H_n^+$
20	0.740 $\pm$ 0.007	0.733 $\pm$ 0.004	$C_8H_n^+$
	0.666 $\pm$ 0.014	0.644 $\pm$ 0.006	$C_{12}H_n^+$
30	0.802 $\pm$ 0.012	0.799 $\pm$ 0.006	$C_8H_n^+$
40	0.883 $\pm$ 0.008	0.872 $\pm$ 0.002	$C_8H_n^+$
50	0.977 $\pm$ 0.011	0.967 $\pm$ 0.005	$C_8H_n^+$
60	1.039 $\pm$ 0.010	1.034 $\pm$ 0.004	$C_8H_n^+$
70	-	1.298 $\pm$ 0.014	$C_4H_n^+$
	1.178 $\pm$ 0.013	1.141 $\pm$ 0.007	$C_8H_n^+$
80	1.623 $\pm$ 0.017	1.621 $\pm$ 0.009	$C_4H_n^+$
	1.343 $\pm$ 0.017	1.344 $\pm$ 0.009	$C_8H_n^+$
85	1.762 $\pm$ 0.008	1.752 $\pm$ 0.008	$C_4H_n^+$
	1.458 $\pm$ 0.011	1.457 $\pm$ 0.013	$C_8H_n^+$
90	1.915 $\pm$ 0.021	1.820 $\pm$ 0.213	$C_4H_n^+$
	1.597 $\pm$ 0.022	1.520 $\pm$ 0.177	$C_8H_n^+$
95	2.084 $\pm$ 0.023	2.077 $\pm$ 0.014	$C_4H_n^+$
	1.742 $\pm$ 0.056	1.808 $\pm$ 0.048	$C_8H_n^+$

Table A.4: Reduced mobility of the peaks for the CF_4-CH_4 mixture ratios studied, obtained for E/N of 15 Td and of 20 Td, for a pressure of 8 Torr at room temperature (293 K).

CF_4-CH_4 CF_4 %	Mobility at 15 Td ($cm^2 \cdot V^{-1} \cdot s^{-1}$)	Mobility at 20 Td ($cm^2 \cdot V^{-1} \cdot s^{-1}$)	Ion
5	2.277 ± 0.129	2.284 ± 0.159	$C_3H_n^+/CF_3^+$
15	2.064 ± 0.107	2.065 ± 0.130	$C_3H_n^+/CF_3^+$
25	2.091 ± 0.049	2.044 ± 0.046	$C_3H_n^+$
	1.796 ± 0.060	1.793 ± 0.051	CF_3^+
40	1.838 ± 0.011	1.834 ± 0.045	$C_3H_n^+$
	1.569 ± 0.015	1.571 ± 0.026	CF_3^+
60	1.704 ± 0.092	1.630 ± 0.020	$C_3H_n^+$
	1.415 ± 0.023	1.407 ± 0.017	CF_3^+
75	-	1.489 ± 0.020	$C_3H_n^+$
	1.249 ± 0.017	1.270 ± 0.008	CF_3^+
85	-	1.403 ± 0.059	$C_3H_n^+$
	1.191 ± 0.059	1.210 ± 0.030	CF_3^+
95	1.149 ± 0.013	1.136 ± 0.022	CF_3^+

Table A.5: Reduced mobility of the peaks for the CF_4-C_2H_6 mixture ratios studied, obtained for E/N of 20 Td, for a pressure of 8 Torr at room temperature (293 K).

CF_4-C_2H_6 CF_4 %	Mobility at 20 Td ($cm^2 \cdot V^{-1} \cdot s^{-1}$)	Ion
5	1.234 ± 0.037	$C_4H_n^+$
15	1.216 ± 0.007	$C_4H_n^+$
25	1.234 ± 0.011	$C_3H_n^+$
	1.194 ± 0.003	$C_4H_n^+$
40	1.369 ± 0.011	$C_3H_n^+$
	1.182 ± 0.011	$C_4H_n^+$
60	1.349 ± 0.005	$C_3H_n^+$
	1.162 ± 0.005	$C_4H_n^+$
75	1.319 ± 0.010	$C_3H_n^+$
	1.139 ± 0.008	$C_4H_n^+/CF_3^+$
85	1.302 ± 0.004	$C_3H_n^+$
	1.139 ± 0.006	$C_4H_n^+/CF_3^+$
	1.061 ± 0.022	?
95	1.288 ± 0.006	$C_3H_n^+$
	1.124 ± 0.002	$C_4H_n^+/CF_3^+$
	1.041 ± 0.016	?

Table A.6: Reduced mobility of the peaks for the CF_4-iC_4H_{10} mixture ratios studied, obtained for E/N of 15 Td and of 20 Td, for a pressure of 8 Torr at room temperature (293 K).

CF_4-iC_4H_{10} CF_4 %	Mobility at 15 Td ($cm^2 \cdot V^{-1} \cdot s^{-1}$)	Mobility at 20 Td ($cm^2 \cdot V^{-1} \cdot s^{-1}$)	Ion
5	0.625 ± 0.005	0.628 ± 0.002	$C_8H_n^+$
	0.572 ± 0.006	0.563 ± 0.008	$C_{12}H_n^+$
15	0.649 ± 0.003	0.647 ± 0.004	$C_8H_n^+$
	0.597 ± 0.012	0.584 ± 0.012	$C_{12}H_n^+$
25	0.673 ± 0.004	0.671 ± 0.005	$C_8H_n^+$
	0.615 ± 0.041	0.588 ± 0.008	$C_{12}H_n^+$
40	0.711 ± 0.001	0.708 ± 0.004	$C_8H_n^+$
60	0.761 ± 0.005	0.761 ± 0.002	$C_8H_n^+$
75	0.823 ± 0.020	0.836 ± 0.027	$C_8H_n^+$
85	0.974 ± 0.081	1.058 ± 0.013	$C_4H_n^+$
	0.855 ± 0.012	0.868 ± 0.009	$C_8H_n^+$
95	1.115 ± 0.004	1.121 ± 0.017	$C_4H_n^+$
	0.926 ± 0.011	0.963 ± 0.007	$C_8H_n^+$